Separation of the Heat Transfer Components from Diffusion Flames Impinging onto Ceilings

Rachel Wasson

Thesis submitted to the faculty of the Virginia Polytechnic Institute and State University in partial fulfillment of the requirements for the degree of

Master of Science

In

Mechanical Engineering

Thomas E. Diller, Chair

Brian Y. Lattimer

Scott T. Huxtable

August 27, 2014

Blacksburg, VA

Keywords: Fire Impingement, Fire plume, Hybrid heat flux gauge, Gas temperature, Coefficient of convective heat transfer, Irradiation

Separation of the Heat Transfer Components from Diffusion Flames Impinging onto Ceilings

Rachel Wasson

ABSTRACT

Two series of experiments were performed to determine the flow characteristics and to quantify the heat transfer components from a propane diffusion flame impinging onto a ceiling. A 0.3 m square sand burner with propane as the fuel type provided a steady-state fire. In the first series of experiments, measurements of gas temperature and velocity were made at 76 mm vertical intervals above the burner up to the ceiling. Fire heat release rates (*HRRs)* of 50 kW and 90 kW with free flame length to ceiling height ratios, L_f/H, of 2, 1.5, 1, 0.8, 0.85 were used to determine their effects on the measured parameters. Gas temperatures within the continuous flaming region were relatively constant, and measured to be independent of ceiling height and *HRR*, while velocities increased with elevation and were independent of ceiling height yet weakly dependent on *HRR*. Within the intermittent region, gas temperature was weakly affected by the presence of the ceiling at various heights, while the effect on velocity was more pronounced. *HRR* had an effect on both temperature and velocity within the intermittent region of the fire plume. Comparisons with existing fire plume correlations showed that the unbounded correlations can be used to provide a good approximation of the gas temperature for the ceiling bounded case; while the correlations for the velocity can only be used for elevations up to approximately 60% of the ceiling height. Elevations above this cutoff were significantly affected by the presence of the ceiling.

The second series of experiments investigated HRRs of 50 kW and 90 kW with free flame length to ceiling height ratios, L_f/H, of 2, 1.5, and 1. Heat flux and gas temperature at the stagnation point of the ceiling were measured using hybrid heat flux gauges and an aspirated Type K thermocouple. Four methods of calculating the convective heat transfer coefficient, h, were developed and adapted; two reference methods and two slope methods. The components of heat transfer at the impingement point were separated using these calculated h values. The reference method 2, and both slope methods only required the use of the non-cooled hybrid gauge measurements and were in overall good agreement with one another. The reference method 1 differed significantly, being up to 15.8 times lower than the others. The trends in the two groups were contradictory, with the h calculated using the reference method 1 increasing with ceiling height while the others showed no strong trend with ceiling height. The disagreements between the methods greatly affected the components of heat transfer, particularly at the lowest ceiling heights. Convection calculated using the h from reference method 1 contributed only 2-5% of the total exposure heat flux at the lowest ceiling heights, whereas with the other methods convection contributed 20-50% of the total exposure heat flux. The limitations of each method are discussed. Further investigation is required for all methods to determine their applicability within the flaming region of a fire.

DEDICATION

This work is dedicated to my parents and my family who have provided me with unwavering support, encouragement, and prayers which have made it possible for me to accomplish my goals. To my sister, Elisa Wasson, and to Philip Jones; you both have been a huge inspiration to me and having you along the journey made it all the more enjoyable.

ACKNOWLEDGEMENTS

Dr. Diller and Dr. Lattimer- Words cannot express how grateful I am to have been able to work with you. I was warned by several people before graduate school about the importance of picking the right advisers and the horrors that could ensue if the wrong decision was made. Turns out I made a great decision. You are excellent advisers. Dr. Diller, your open door policy and expertise in the field of heat transfer was invaluable to my growth as a graduate student and engineer. Dr. Lattimer, your knowledge and expertise in the area of fire science was an integral part to this research. I really knew nothing about fire research and your insight and suggestions help me to progress in my work. I learned a lot from both of you. Anytime I was unclear about something, or felt stuck in some way, your suggestions and experience always provided a path forward. I am honored to have worked with two experts in their fields.

Dr. Huxtable- Although I was never able to take your radiation course, I always found it easy to set up time to talk with you about my studies. You were willing to help in any way possible, which I am thankful for.

Extreme Lab Members- Joshua McNeil, Christian Rippe, Joseph Starr thank you for all of your guidance and help in the fire lab and with the propane system. Also for taking time out of your day to spend several hours at a time out at the fire lab while I ran experiments. Christian, thank you for letting me borrow your test setup for a few months before I built my monstrous one. Nahid, thank you for your collaboration on the velocity and gas temperature paper. It was a pleasure working with you. And to all the SFPE officers: Joseph Starr, Christian Rippe, Joshua McNeil, Jong Hwan Kim, for your help in setting up events and booths to promote our society.

Heat Transfer Lab members-Abdusalam Al-Khwaji, thank you for your insight into the problems I encountered and for the references you provided. Akashdeep Sing Virk thanks for your assistance in setting up experiments and for running a some extra ones while I was away; I know it took up a lot of your time.

Sandia National Laboratories, NM- I want to thank my manager, John Lorio, and team, for the opportunity to attend graduate school while remaining a SNL employee. Working with you has been an enjoyable experience and I could not imagine a better team to be a part of. Also to John, for understanding the challenges that come with research. To SNL's Master's Fellowship Program in partnership with the GEM Fellowship: my graduate school attendance was made possible through the financial support provided by you, thank you.

TABLE OF CONTENTS

1. Introduction and Thesis Organization 1
1.1. Introduction 1
1.2. Organization 2
References 2
2. Influence of a Ceiling on Fire Plume Velocity and Temperature 5
2.1. ABSTRACT 5
2.2. Introduction 7
2.3. Experimental Methods 10
2.3.1. Burner and Experimental Apparatus 11
2.3.2. Gas Temperature 12
2.3.3. Velocity 12
2.3.4. Test Matrix 13
2.3.5. Experimental Procedure 14
2.4. Fire Dynamics Simulations 14
2.5. Analysis and Discussion 16
2.5.1. Gas Temperature Results 16
2.5.1.1. Effect of Ceiling Height on Gas Temperature 16
2.5.1.2. Effect of HRR on Gas Temperature 17
2.5.1.3. Comparison to FDS Simulation 18
2.5.2. Velocity Results 19
2.5.2.1. Effect of Ceiling Height on Velocity 19
2.5.2.2. Effect of HRR on Velocity 21
2.5.2.3. Comparison to FDS Simulation 23
2.6. Discussion 24
2.6.1. Comparison to Correlations Found in the Literature 24
2.7. Conclusions 28
2.8. Acknowledgements 28
References 28
3. Partitioning Measurements of Convection and Irradiation Heat Transfer Components from Diffusion Flames Impinging onto Ceilings 31
3.1. ABSTRACT 31

3.2. Introduction 33
3.3. Experimental Methods 39
3.3.1. Burner and Experimental Apparatus 40
3.3.2. Heat Flux 41
3.3.3. Gas Temperature 43
3.3.4. Velocity 44
3.3.5. Test Matrix 45
3.3.6. Experimental Procedure 45
3.4. Results 46
3.4.1. Heat Fluxes and Temperatures 46
3.4.2. Convective Heat Transfer Coefficient 50
3.4.2.1. Reference Method 1, Two Gauges 51
3.4.2.2. Reference Method 2, One Gauge 53
3.4.2.3. Slope Method 1, One Gauge 55
3.4.2.4. Slope Method 2, One Gauge 58
3.4.2.5. Summary of h Values and Effects of HRR and Ceiling Height 60
3.4.3. Velocity, Reynolds and Rayleigh Number 65
3.4.4. Separated Heat Transfer Components 67
3.5. Discussion 71
3.5.1. Separated Components of Heat Transfer 71
3.5.2. Methods of Calculating h 72
3.5.3. Calculated Standard State Heat Flux 75
3.5.4. Comparison to Previous Studies 76
3.6. Conclusions 80
3.7. Acknowledgements 81
References 81
4. Conclusions and Recommendations 85
4.1. Conclusions 85
4.2. Recommendations for Future Work 86
APPENDIX A- UNCERTAINTY CALCULATIONS IN REFERENCE METHOD 1 AND SLOPE METHOD 1 88
APPENDIX B- CALIBRATION PROCEDURES AND CALCULATED GAUGE SENSITIVITIES 97

APPENDIX C- SOOT CALIBRATIONS 112
APPENDIX D -VELOCITY AND GAS TEMPERATURE PROCEDURE 114
APPENDIX E -HEAT FLUX MEASUREMENTS PROCEDURE 119
APPENDIX F – COMPARISON OF METHODS FOR CALCULATING H USING PREVIOUS EXPERIMENTS 127
APPENDIX G- FFT OF PRESSURE DATA 131
APPENDIX H- EXPOSURE HEAT FLUXES 133

LIST OF FIGURES

Figure 2.1: Experimental Setup 11

Figure 2.2: Example Test Case 12

Figure 2.3: Effect of Ceiling Height on Gas Temperature: a) 50 kW, b) 90 kW 17

Figure 2.4: Effect of *HRR* on Gas Temperature: a) L_f/H=2, b) L_f/H=1.5, c) L_f/H=1, d) L_f/H=0.85 and L_f/H=0.8 18

Figure 2.5: Gas Temperature Experimental Results Compared with Simulation Results: a)50 kW, H=0.64 m, b) 90 kW, H=0.64 m, c) 50 kW, H=1.51 m, d) 90 kW, H=1.51m 19

Figure 2.6: Effect of Relative Ceiling Height on Velocity a) 50 kW, V vs. $z/Q^{2/5}$, b) 90 kW, V vs. $z/Q^{2/5}$, c) 50 kW, V vs. z/H, d) 90 kW, V vs. z/H 21

Figure 2.7: Effect of *HRR* on Velocity: a) L_f/H=2, b) L_f/H=1.5, c) L_f/H=1, d) L_f/H=0.85 and L_f/H=0.8. 22

Figure 2.8: Velocities Scaled by parameters given in Ref. [3]: a) L_f/H=2, b) L_f/H=1.5, c) L_f/H=1, d) L_f/H=0.85 and L_f/H=0.8. 22

Figure 2.9: Velocity Experimental Results Compared with Simulation Results:a)50 kW, H=0.64 m, b) 90 kW, H=0.64 m, c) 50 kW, H= 1.51 m, d) 90 kW, H=1.51m 23

Figure 2.10: Gas Temperature Comparison with McCaffrey[3], Cox and Chitty [4], You and Faeth [16] 25

Figure 2.11: Velocity Comparison with McCaffrey [3], Cox and Chitty [4], You and Faeth [16] 26

Figure 2.12: Gas Temperature and Velocity Comparison with Kung et al.[5] 27

Figure 3.1: Experimental Setup 39

Figure 3.2: Top View of Measurement Locations Relative to Ceiling 40

Figure 3.3: Hybrid Heat Flux Gauge design, a) Hybrid heat flux gauge thermopile design with attached thermocouples, where TC_1=Ts and TC_2=Tb Dimensions for the thermopile are l=9.65 mm, w=5.08 mm, and δ=3.18 mm, b) non-cooled configuration, Housing dimensions are l=25.4 mm, w= 12.7 mm, and h =3.18 mm, c) air-cooled configuration, diameter of 12.7 mm 41

Figure 3.4: Raw Heat Fluxes and Temperatures for 90 kW, L_f/H=1.5 test condition, a) Measured Non-cooled heat flux, b) Measured Air-cooled Heat Flux, c) Non-cooled Temperatures, d) Air-cooled Temperatures. 47

Figure 3.5: Gas Temperatures for 90 kW, L_f/H=1.5 test condition, a) Near velocity probe, b) Near ceiling. 48

Figure 3.6: Heat Flux and Temperatures at Ceiling Stagnation Point: a) 50 kW Heat Fluxes, b) 90 kW Heat Fluxes, c) 50 kW Gauge Surface Temperatures, d) 90 kW Gauge Surface Temperatures. 49

Figure 3.7: Gas Temperatures: a) 50kW *HRR*, b) 90 kW *HRR* 50

Figure 3.8: Reference Method 1 *h* Values: a) 50 kW *HRR*, b) 90 kW *HRR* 52

Figure 3.9: Reference Method 1 Average *h* Values 53

Figure 3.10: Reference Method 2 *h* Values: 90 kW *HRR*, L_f/H=1.5 54

Figure 3.11: Average *h* Values for Reference Method 2 55

Figure 3.12: Slope Method 1 *h* Values: 90 kW, L_f/H=1.5 57

Figure 3.13: Average *h* Values for Reference Method 2 58

Figure 3.14: Slope Method 2 *h* Values: 90 kW, L_f/H=1.5 59

Figure 3.15: Average *h* Values Slope Method 2: 90kW, L_f/H=1.5 60

Figure 3.16: Summary of Average *h* Values for all Methods of Calculating *h*, a) 50 kW, b) 90 kW 61

Figure 3.17: Average *V, Re, Ra*: a) *V* , b) *Re* number, c) *Ra* number, Equation (15), d) *Ra* number, Equation (16) 66

Figure 3.18: Separated Heat Transfer Components: a-b) L_f/H=2, 50 and 90 kW *HRR* respectively, c-d) L_f/H=1.5, 50 and 90 kW *HRR* respectively,e-f) L_f/H=1, 50 and 90 kW *HRR* respectively. 70

Figure 3.19: Relative Variations in the Calculated *h* Values for all methods and experimental configurations. 72

Figure 3.20: Calculated Standard State Heat Fluxes: a) 50 kW, L_f/H=2 b) 90 kW, L_f/H=2 , c) 50 kW, L_f/H=1.5, d) 90 kW, L_f/H=1.5, e) 50 kW, L_f/H=1, f) 90 kW, L_f/H=1 76

Figure 3.21: Comparison of Experimental Data with Refs. [19, 24], a) q_o vs. L_f/H b) non-dimensional q_o vs L_f/H 78

Figure 3.22: Comparison of Calculated *h* Values with Ref. [25] 80

Figure A.1. Relative Uncertainty in Non-cooled heat flux in a) convection only and b) mixed-mode environments 90

Figure A.2. Reference Method Squared Sensitivity Coefficients: a) convection only, and b) mixed mode 92

Figure A.3. 95% CL Relative Uncertainty in Reference Method Heat Transfer Coefficient in a) convection only and b) mixed-mode environments. 93

Figure B.1: Pneumatic Cylinder with valves 103

Figure B.2: Air-cooled Gauge Voltage vs. Absorbed Heat Flux 108

Figure B.3: Air-cooled Gauge Differential Sensitivities 109

Figure B.4: Air-cooled Gauge Slug Sensitivities 109

Figure B.5: Non-cooled Gauge Voltage vs. Absorbed Heat Flux 110

Figure B.6: Non-cooled Gauge Differential Sensitivities 111

Figure B.7: Non-cooled Gauge Slug Sensitivities 111

Figure D.1: Setra Gauge 115

Figure D.2 Bi-directional Probe 116

Figure D.3: Ceiling Apparatus 116

Figure D.4: Bi-directional and Aspirated Thermocouple Probe Placement 117

Figure E.1: Setra Gauge 120

Figure E.2: Bi-directional Probe 121

Figure E.3: Ceiling Apparatus 121

Figure E.4: Gauge Placement 122

Figure E.5: Bi-directional and Aspirated Thermocouple Probe Placement 124

Figure E.6: Aspirated Thermocouple Placement 124

Figure E.7: Gauges with Soot 125

Figure F.1: Original Reference Method vs. Reference Method 1- 40 kW/m^2-K case 128

Figure F.2: Reference Method 2- 40 kW/m^2-K case 129

Figure F.3: Slope Method 1-40kW/m^2 case..... 129

Figure G.1: Sample of Pressure Data..... 132

Figure G.2: Sample of FFT of Pressure Data 132

Figure H.1: T_∞-T and q_{exp} for 50 kW HRR: a) L_f/H=2, b) L_f/H=1.5, c)L_f/H=1 134

LIST OF TABLES

Table 2.1: Test Matrix 13

Table 2.2: Thermo-physical properties of ceiling material 15

Table 3.1: Maximum Velocity Elevations 44

Table 3.2: Test Matrix 45

Table 3.3: Summary of *h* Values 64

Table 3.4: Summary of Average V, Re (Equation 14), and Ra (Equation 15) 67

Table 3.5: Correlations from Ref. [3, 17, 23] 79

Table A.1: Non-cooled heat flux Uncertainty Components 89

Table A.2: Uncertainty Budget for Reference Method Coefficient of Heat Transfer 92

Table A.3 Sensitivity Coefficients of Slope Method 95

Table C.1: Gauge Emissivities 113

Table D.1: Test Matrix for Velocity Measurements 115

Table E.1: Test Matrix for Heat Flux Measurements 120

Table E.2: Max Velocity Heights for Each Test Condition 123

Table F.1: Summary of Comparisons for *h* Methods 130

1. Introduction and Thesis Organization

1.1. Introduction

Flames impinging onto a horizontal ceiling create high levels of localized heat flux and temperatures within the stagnation region of ceiling structures. These types of localized fires may cause ignition of combustible surfaces, burn through of materials, and aide in the spread of the fire through convective and radiative heat transfer [1, 2]. The gas temperature and velocity along the centerline of an impinging fire plume govern the amount of convective heat transfer from the flame to the ceiling stagnation point. These flow conditions must be quantified to validate computational and mathematical models used to predict the thermal insult of a ceiling exposed to fire.

Measurements of gas temperature and velocity for the unbounded case were used to develop correlations of the flow characteristics of the fire plume [3, 4, 5]. These studies did not show the effect that bounding had on the plume characteristics. You and Faeth [6] conducted an extensive study of a ceiling bounded fire plume; however, their measurements corresponded to small scale fires. Measurements of a bounded fire plume on a larger scale are needed to accurately quantify the effect that the presence of a ceiling may have on a more realistic fire.

The fire thermal boundary conditions on the ceiling are necessary parameters used in computational fire models to predict the thermal response of the ceiling materials which are exposed to the fire. Well defined boundary conditions provide more accurate predictions of material behavior under the thermal stresses present in a fire. The thermal boundary is most commonly defined using total heat flux and temperature. The total heat flux to the ceiling is measured using water-cooled heat flux gauges [7]. Separation of the convection and irradiation components is usually accomplished through the use of two heat flux gauges; either at different, known emissivities [8, 9, 10-12, 13], or by using a total heat flux gauge, and a windowed radiometer [14, 15]. Soot formation on the gauges and the need for water-cooling lines or gas purging of the window make these measurements difficult in fires. Quantifying the convective heat transfer coefficient has been attempted using models and numerical inverse techniques [16, 17]; however, there were non-negligible errors associated with both methods.

This research focuses on defining the flow characteristics and heat transfer modes from a diffusion flame impinging onto a ceiling. Measurements of gas temperature and velocity were

made along the centerline of the fire plume. The temperature and velocity profiles were compared to the unbounded case and were used to provide insight into the behavior of the convective heat transfer to the ceiling. Measurements of heat flux using a hybrid heat flux gauge and gas temperature were also made at the impingement point of the ceiling. Four different methods of calculating the convective heat transfer using two and one heat flux gauge were investigated and used to separate the components of heat transfer. These measurements provide the capability to define a more detailed boundary condition which can be used in future fire models.

1.2. Organization

This thesis is organized into two manuscripts. The first manuscript corresponds to the second chapter of this thesis and the second manuscript corresponds to the third chapter. References for each can be found at the end of each chapter. Figures are embedded into the text to allow for ease of reading. Supplementary material can be found in the Appendices.

The second chapter of this thesis focuses on measurements of gas temperature and velocity along the centerline of a propane diffusion flame impinging onto a ceiling. Fire heat release rate (*HRR*) and ceiling height were varied to investigate the effects they have on the time averaged gas temperature and velocities of the fire plume within the various regions of the flame. Comparisons were made with existing unbounded fire plume correlations and with simulations performed using Fire Dynamics Simulator (FDS).

The third chapter of this thesis focuses on the separation of the convection and irradiation from the fire to the ceiling. Heat flux and gas temperature measurements were made at the impingement point of the ceiling. Four different methods of calculating the convective heat transfer coefficient were applied and developed for this fire scenario. The components of heat transfer were separated using the gas temperature and heat flux measurements. Fire *HRR* and ceiling height were varied to determine their effects on the components of heat transfer to the ceiling.

References

1. Hinkley, P.L, Wraight, H.G.H., Theobald, C.R., The contribution of flames under ceilings to fire spread in compartments, Fire Safety Journal 7 (1984) 227-242.

2. Hasemi, Y., Firesafety of building exposed to a localized fire-scope and experiments on ceiling/beam system exposed to localized fire, in 1st International Conference ASIAFLAM (1995) 351-361.
3. McCaffrey, B.J., Report NBSIR 79-1910, National Bureau of Standards, (1979).
4. Cox, G., Chitty, R., A study of the deterministic properties of unbounded fire plumes, Combustion and Flame 39 (1980) 191-209.
5. Kung, H.C., Stavrianidis, P., Buoyant plumes of large-scale pool fires, in: Nineteenth Symposium (International) on Combustion (1982) 905-912.
6. You, H-Z., Faeth, G.M., An investigation of fire impingement on a horizontal ceiling, Report NBS-GCR-80-251, National Bureau of Standards, (1979).
7. Diller, T. E., Heat Flux Measurement, Ch. 18, in: Handbook of Measurement in Science and Engineering, Ed. M. Kutz, John Wiley & Sons, NY (2013) 639-643.
8. Lattimer, B.Y., Vandsburger, U., and Langley, L.W., Detecting fires using a thin-film heat flux microsensor, ASME Winter Annual Meeting, Chicago, Illinois, HTD, Vol. 296, November (1994) 137-142.
9. Lennon, P. and Silcock, G., A Preliminary Investigation into the Partitioning of the Convective and Radiative Incident Heat Flux in Real Fires, Fire Technology 42(2) (2006) 109-129.
10. You, H-Z., Faeth, G.M., An investigation of fire impingement on a horizontal ceiling, Report NBS-GCR-79-188, National Bureau of Standards, (1978).
11. You, H.Z., Faeth, G.M., Ceiling heat transfer during fire plume and fire impingement, Fire and Materials, **3**, (1979) 140-147.
12. You H.Z., An investigation of fire-plume impingement on a horizontal ceiling, Fire and Materials, **9** (1985) 46-56.
13. Kokkala, M.A., Experimental study of heat transfer to ceiling from an impinging diffusion flame, in: Proceedings of the 3rd International Symposium on Fire Safety Science (1991) 261-270.
14. Blanchat, T., O'Hern, T., Kearney, S., Ricks, A., and Jernigan, D., Validation experiments to determine radiation partitioning of heat flux to an object in a fully turbulent fire, in: Proceedings of the Combustion Institute 32(2) (2009) 2511-2518.

15. Nakos, J. T., Keltner, N.R., The radiative-convective partitioning of heat transfer to structures in large pool fires, American Society of Mechanical Engineers, Heat Transfer Division, HTD 106 (1989).
16. Weng, W.G., and Hasemi, Y., Heat transfer to an unconfined ceiling from an impinging buoyant diffusion flame, Heat and Mass Transfer 42 (2006) 652-659.
17. Zhang, J., Delichatsios, M.A., Determination of the convective heat transfer coefficient in three-dimensional inverse heat conduction problems, Fire Safety Journal 44 (2009) 681-690.

2. Influence of a Ceiling on Fire Plume Velocity and Temperature

Rachel Wasson*, Mohammad N. Nahid, Brian Y. Lattimer, Thomas E. Diller

Department of Mechanical Engineering

Virginia Tech

2.1. ABSTRACT

A series of experiments with a fire impinging onto a ceiling were conducted to quantify the influence of a ceiling on the fire plume centerline gas temperatures and velocities. A 0.3m square porous burner with propane as the fuel type provided a steady-state diffusion flame. Time averaged gas temperatures and velocities were measured at 76 mm vertical intervals along the centerline of the impinging fire plume for fire heat release rates (*HHRs*) of 50 kW and 90 kW and flame height to ceiling height ratios of L_f/H=2, 1.5, 1, and 0.8/0.85. The effects of each on the fire plume gas temperature and velocities were investigated. At elevations close to the burner surface, gas temperature and velocity were independent of ceiling height. As the elevation above the burner increased, gas temperatures decreased slightly with increasing ceiling height, while velocities differed greatly across ceiling heights, initially increasing with elevation followed by a decrease close to the ceiling. Both gas temperature and velocity differed significantly between *HRR*s, with the exception of gas temperatures close to the burner surface and within the plume region. Measured gas temperature and velocity results compared favorably with a simulation performed in Fire Dynamics Simulator (FDS), with their maximum values within 5.74 % and 11.6% of each other, respectively. Comparisons with existing fire plume correlations showed that maximum gas temperatures were slightly lower within the flaming region, and shifted in the intermittent regions for the 50 kW *HRR*. Velocities were lower in all regions, due to the presence of the ceiling. It is suggested that the unbounded correlations can be used as a good approximation of the gas temperature for the ceiling bounded case; while the correlations for the velocity can only be used for elevations up to approximately 60% of the ceiling height.

*Author for Correspondence:
Rachel Wasson
United States of America
1-505-681-0447
awrach9@vt.edu

NOMENCLATURE

C	Calibration/Empirical constant (--)
C_p	Specific heat at constant pressure (KJ/kg-K)
D^*	characteristic fire diameter
g	Gravitational constant (9.8 m/s^2)
H	Ceiling Height (m)
HRR	Heat release rate
L_f	Free flame length (m)
Δp	Differential pressure (Pa)
Q	Heat release rate (kW)
T_∞	Gas temperature (^{o}C)
ΔT	Temperature rise above ambient (^{o}C)
t	time (s)
V	Vertical velocity component (m/s)
z	Elevation above burner (m)
z_o	Virtual origin (m)

Greek

ρ	density (kg/m$^{3)}$
δx	computational cell size

Subscripts

o	origin
∞	gas
f	flame
c	convective

2.2. Introduction

Flames impinging onto ceilings create high levels of localized heat flux and temperatures within the stagnation region of ceiling structures. These types of localized fires may cause ignition of the ceiling, burn through of materials, and aide in the spread of fire [1, 2]. The increased amount of convective heat transfer at the stagnation point helps to accelerate fire spread along the ceiling and to other room structures. The gas temperature and velocity along the centerline of an impinging fire plume govern the amount of convective heat transfer from the flame to the ceiling stagnation point. These flow conditions must be quantified to validate computational and mathematical models used to predict the thermal insult onto a ceiling exposed to fire.

Measurements of velocities and gas temperatures have been made in previous experiments found in the literature. Several works have concentrated on making these measurements within the flaming region of the plume, i.e. fire plume; however, the data presented is mostly for the unbounded case only [3-5]. McCaffrey [3] conducted experiments using a natural gas buoyant diffusion flame with a 0.3 m porous burner for fire heat release rates (*HRR*s) ranging from 14kW to 58 kW. Differential pressure and gas temperature measurements were made in the fire plume centerline at various elevations using a 16mm diameter bi-directional probe and 1 mm diameter Type K thermocouple. Cox and Chitty [4] conducted a similar study as that of McCaffrey using a natural gas 0.3 m square porous burner with *HRR* ranging between 14 kW and 47 kW. Vertical velocity component measurements were made with an electrostatic probe and gas temperature measurements were made with 0.16 mm Type K thermocouples. Kung and Stavrianidis [5] measured gas temperature and velocity within and above the flaming region of unbounded large-scale pool fires. Pool diameters and fuel type were varied to obtain different heat release rates. A set of Type K thermocouple and bi-directional probes were placed at nine elevations to measure centerline and radial distributions of temperature and velocity

These works identified three distinct regions within the flame: 1) the continuous flaming region, $0.03<z/Q^{2/5}<0.08$, 2) the intermittent region, $0.08<z/Q^{2/5}<0.20$, and 3) the non-combusting plume region $z/Q^{2/5}>0.20$. The continuous region was characterized by a constant temperature with no dependence on z or Q. McCaffrey [3] measured a temperature rise above ambient, ΔT, of 800^{o}C and Cox and Chitty measured 880^{o}C [4]. The difference between the two

measurements was attributed to radiation effects on the thermocouple used in the measurements of McCaffrey. Kung and Stavrianidis [5] found a better collapse to their data when including the virtual origin of the source, z_o. They defined the continuous flaming region as $(z\text{-}z_o)/Q^{2/5} < 0.14$ with a measured ΔT of 900 ^oC [5]. The velocity within the continuous region was determined to be independent of Q, however increased with elevation as $V=Cz^{1/2}$ for Refs. [3, 4]. McCaffrey measured C= 6.84, while Cox and Chitty measured C=6.83. Kung and Stavrianidis measured velocity to be independent of elevation in the region of $(z\text{-}z_o)/Q^{2/5} < 0.14$ with a range from 1.3-1.8.

In the intermittent region of the flame, ΔT was measured to be dependent upon both z and Q, with $\Delta T = 70Q^{2/5}z^{-1}$ [3] and $\Delta T = 63Q^{2/5}z^{-1}$ [4]. For $(z\text{-}z_o)/Q^{2/5} > 0.14$, Kung and Stavrianidis [5] found that $\Delta T = CQ^{2/3}(z\text{-}z_o)^{-5/3}$, where $C = 8.6g^{-1/3}(c_p\rho_\infty T_\infty)^{-2/3}Q_c^{2/3}(z-z_o)^{-5/3}$. Velocity within this region was independent of z; however, it had a slight dependence on Q with values of $V=1.93Q^{1/5}$ and $V=1.85Q^{1/5}$ from McCaffrey and Cox and Chitty, respectively. Kung and Stavrianidis measured a velocity dependent on $Q_c^{1/3}$ and $(z\text{-}z_o)^{-1/3}$ for $(z\text{-}z_o)/Q^{2/5} > 0.18$. The works of McCaffrey, Cox and Chitty, and Kung and Stavrianidis provide a clear insight into the gas temperatures and velocities of fire plumes. However, they fail to provide data on how the presence of a ceiling within the fire plume may affect these parameters.

Work has been done for cases of plume and fire plume impingement on ceilings [6-11]. These experiments correspond to either the non-combusting plume region impinging onto the ceiling, or to the ceiling jet region of the fire plume, rather than the flaming region of the fire. Very few studies have been conducted where gas temperatures and velocities were measured along the centerline of an impinging fire plume.

McCaffrey's work included experiments with a floor and ceiling present. He discussed that although the floor caused the flame to be more susceptible to outside disturbances, there were only minor differences in the temperature and velocity, with both being slightly higher within the flame and slightly lower above the flame. With the ceiling present, McCaffrey stated that there were no noticeable differences up to about 70% of the ceiling height [3]. No data was shown with either ceiling or floor present. Kokkala [12] conducted experiments using a methane buoyant diffusion flame. Heat flux to the ceiling and gas temperature 18 mm below the ceiling were measured at the stagnation point of the flame and in the ceiling jet region. Temperature measurements were made with 0.25 mm Type K thermocouples. Heskestad and Hamada [13]

measured gas temperatures beneath an impinging flame onto a ceiling from round propane burners. Burner diameters between 0.15-0.61 m were used with free flame length to ceiling height ratios, L_f /H, of 0.52-1.24 m. Chatterjee et al. [14] conducted experiments within the fire plume of an impinging flame onto a ceiling to validate their computational model used for automatic sprinkler activation calculations. HHRs of 1500-5000 kW with ceiling height of 3.0-6.0 m were studied, which were chosen to simulate the large *HRR*s associated with rack storage fires [14]. Excess temperature and velocity along the centerline of the fire plume was measured for the unbounded case only. Radial distributions of temperature and velocity in the ceiling jet region were also measured. Results compared favorably with data from Kung et al. [15].

Kokkala [12] compared his data with the work of McCaffrey for the unbounded fire plume [3]. Kokkala's temperatures were higher than those of McCaffrey within the continuous flaming region, with values above 1000^{o}C. He measured a steeper decrease in temperature with ceiling height than the temperatures measured by McCaffrey. These differences were attributed to the jet-like characteristics associated with Kokkala's flames [12]. Heskestad and Hamada compared their data with that of Kung and Stavrianidis [5]. Rather than scaling *z* with the virtual source, they scaled the ceiling height, H, with the virtual source. This provided a favorable comparison with the data of Kung and Stavrianidis [5] for the unbounded fire plume. Kokkala as well as Heskestad and Hamada only measured gas temperatures near the ceiling. Their work did not include velocity measurements at various elevations within the fire plume. Both gas temperature and velocity are needed to make predictions on the overall thermal insult to the ceiling.

You and Faeth [16] conducted experiments within a turbulent flame impinging on a horizontal ceiling. This study was the most extensive investigation of gas temperature and velocity along the centerline of a fire plume impinging on a ceiling, and most closely matches with the current work. Natural gas, consisting of approximately 95% methane was used as the fuel type. Their fires were on a much smaller scale, than the current research, with a 0.055 m diameter source producing *HRR*s of 1.67 kW and 8.41 kW [16]. Experiments were run with a ceiling placed 0.41 m above the burner and without a floor in place. Centerline gas temperature was measured with fine wire platinum-rhodium thermocouples, while centerline average velocities and velocity fluctuations were measured using a laser Doppler anemometer. The data was scaled according to McCaffrey and compared with data from Refs. [3, 4, 17-20]. The three

flame regimes discussed in Refs. [3, 4] were also observed; however, discrepancies existed in the data at elevations near the burner surface. You and Faeth attributed this to differences in burner characteristics. You and Faeth's three regimes consisted of 1) increasing temperature and velocities near the burner surface, 2) slowly varying temperature and velocities near the flame tip, and 3) decreasing temperature and velocity above the flame. You and Faeth's work provided both gas temperature and velocity data within impinging flames; however, their data corresponded to very small-scale fires. These small scale experiments are not realistic in naturally occurring fires; therefore, larger scale testing is needed to determine if their results are applicable to real fire scenarios.

This research focuses on larger scale testing using propane diffusion flames impinging onto ceilings. A series of experiments were performed to measure the gas temperatures and velocities at various elevations along the centerline of the flame impinging onto a ceiling. *HRR* and ceiling height were varied to capture the effects these parameters have on the time- averaged gas temperatures and velocities beneath the ceiling. Comparisons were made to existing fire plume correlations [3-5] and to smaller scale testing with a ceiling [16] to determine if the presence of the ceiling makes a significant difference in the gas temperatures and velocities in this fire scenario. Comparisons were also made to simulations from Fire Dynamics Simulator (FDS).

2.3. Experimental Methods

Experiments were performed using a propane diffusion flame impinging onto a ceiling. A picture of the experimental setup is shown in Figure 2.1. A Unistrut® apparatus was designed to support a square gypsum board ceiling which was centered over a square diffusion burner. Gas temperature and velocity were measured with an aspirated thermocouple and a bi-directional probe along the centerline of the impinging fire plume. The entire setup was surrounded my metal mesh and placed under a fume hood.

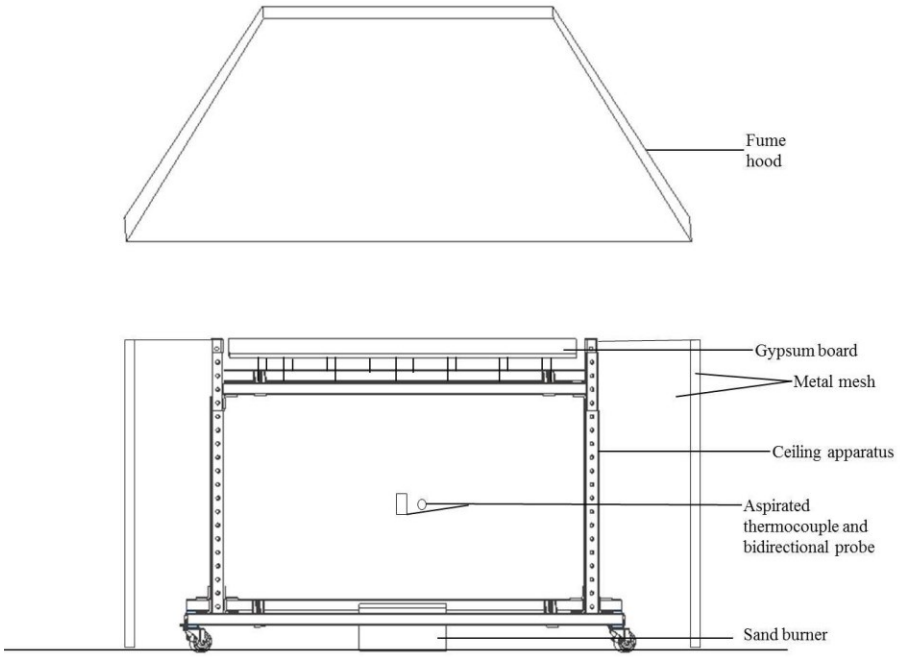

Figure 2.1: Experimental Setup

2.3.1. Burner and Experimental Apparatus

Propane diffusion flames were generated using a 0.3 m square porous sand burner with a height of 0.15 m, and the burner located on a concrete floor. Propane gas supplied to the burner was set using an Alicat MC-100 mass flow controller with a range of 120 SLPM and an accuracy of ±0.2% full scale. This type of burner setup generates a steady-state diffusion flame that simulates the characteristics associated with a naturally occurring fire.

An apparatus was designed to hold a square ceiling over the burner. As illustrated in Figure 2.1, it consisted of telescoping Unistrut® tubing to allow for adjustable ceiling heights. The apparatus was designed to accommodate ceiling heights up to 1.51 m above the burner surface. For these experiments, the ceiling consisted of a 1.22 m square piece of 15.9 mm thick, Type X, fire-resistant gypsum board. The ceiling is supported by 127 mm long, 6.3 mm diameter bolts to reduce the amount of heat transfer by conduction from the frame to the ceiling, and to provide a path for the smoke to flow out from under the ceiling. One layer of steel diamond screen, with 6.35 x 12.7 mm hole size, was placed around the entire experimental setup to reduce disturbances caused by air drafts in the test room. Figure 2.2 displays the experimental setup during an example test case.

Figure 2.2: Example Test Case

2.3.2. Gas Temperature

Gas temperature was measured along the centerline of the fire plume at various elevations above the burner to quantify the thermal environment produced by the fire plume. Measurements were made along the centerline of the fire plume at 76 mm vertical intervals, starting at 0.23 m above the burner up to the ceiling. An aspirated thermocouple was used to measure the gas temperature to minimize radiation errors associated with using bare bead thermocouples [22]. As suggested in Ref. [22], a bare bead Type K thermocouple with 0.25 mm diameter Inconel sheathed wires was placed into a 6.35 mm diameter stainless steel tube attached to a pump. The pump drew air over the bead at a velocity of 15 m/s, creating a convection-dominated environment and thereby reducing radiation effects on the bead. The thermocouple bead was located along the axial centerline of the tube, 19 mm from the tube inlet. Data was collected using a National Instruments 9213 thermocouple module at a sampling rate of 200 Hz.

2.3.3. Velocity

Differential pressures were measured using a 19 x 50 mm bi-directional probe [23] located directly adjacent to the aspirated thermocouple. Measurements were made along the centerline of the fire plume at 76 mm vertical intervals up to the ceiling. The bi-directional probe was connected to a Setra Model 264 differential pressure transducer with a range of ± 62.3 Pa, and an accuracy of 0.22 % full scale. Data was collected using a National Instruments 9205 module at a sampling rate of 200 Hz.

Velocities were calculated from the differential pressure measurements according to the methodology outlined in Ref. [23]. Using the Bernoulli equation, and assuming pressure effects on density are negligible, the velocity can be calculated as follows,

$$V = \frac{1}{C}\sqrt{\frac{2\Delta p}{\rho}} \quad (1)$$

where C is a calibration constant determined in Ref. [23]. For this work, C was set to 1.08, corresponding to higher Reynolds numbers. The gas temperature measurements were used to determine the elevated temperature density in Equation (1).

2.3.4. Test Matrix

Fire *HRR*, ceiling height, and elevation above the burner were the three parameters investigated in this series of experiments. A summary of the test matrix is provided in Table 2.1. *HRRs* of 50 kW and 90 kW and ceiling heights of 0.49-1.51 m were used in this study to produce a range of free flame lengths to ceiling height ratios, L_f/H. Free flame lengths, L_f, were calculated based off a correlation developed by Hasemi [2]. Hasemi found that the total heat flux from an impinging diffusion flame to a ceiling experiences the steepest growth in the region from L_f/H=2.5 to L_f/H=1 [2]. Therefore, ceiling heights of L_f/H=2, L_f/H=1.5, and L_f/H=1 were chosen to better capture the changes in the velocities and gas temperatures where heat transfer has been measured to change. Two other points at L_f/H=0.8 (50 kW fire) and L_f/H=0.85 (90 kW fire) were selected to look at conditions where the ceiling was placed at an elevation above the flames, in the plume region. Velocities and gas temperatures were measured along the centerline of the fire at 0.076 m increments above the burner starting at an elevation of 0.23 m.

Table 2.1: Test Matrix

	Ceiling Height Above Burner, *H* (m)	
Relative Ceiling Height Above Burner, L_f/H	**50 kW (L_f = 0.98 m)**	**90 kW (L_f = 1.28 m)**
2	0.49	0.64
1.5	0.64	0.85
1	0.97	1.28
0.8	1.22	-
0.64, 0.85	1.51	1.51

At the 1.51m ceiling height, measurements were made for both *HRR*s to allow for a comparison to FDS simulation results.

2.3.5. Experimental Procedure

Each test was performed following the same procedure to ensure repeatability in the results. Prior to each test, the bi-directional probe and aspirated thermocouple were adjusted to the appropriate elevation above the burner and placed side by side at the centerline of the flame. A two minute baseline was recorded for both probes, before ignition of the fire. Following the baseline measurement, the propane mass flow was set to achieve the desired *HRR* and the burner was lit. After the aspirated thermocouple reached a steady state, data was recorded for 90 seconds from both the aspirated and bi-directional probes. Three repetitions were performed for each experimental configuration at each elevation above the burner. Results from the three repetitions had a variation from the mean within 8.47% for all tests with the exception of the 1.51m height for the 50 kW fire, which had variation from the mean within 14.2%.

Data from each test was first filtered using a Hann window with a cutoff frequency of 15 Hz. This was done to get rid of the strong 60 Hz signal induced into the measurement from the fume hood in the laboratory. The results were then time averaged, neglecting the portions in time when the flame leaned away from the probes.

The diffusion flame was unstable at times, with the flame occasionally leaning off the centerline. This occurred even with the metal screen around the burner setup. This flame behavior was attributed to air drafts in the test room, thermal gradients in the test room causing natural convection currents, and ambient air entrained horizontally near the burner surface due to the presence of the floor. This behavior was also observed by McCaffrey [3]. Data from times when the flame leaned was not used in the analysis and is not shown here.

2.4. Fire Dynamics Simulations

Computational modeling was used to validate measured fire plume gas temperature and velocity measurements. Simulations on fire conditions were conducted using Fire Dynamics Simulator (FDS), Version 6.0 [24]. FDS is a computational fluid dynamics (CFD) model that uses large-eddy simulation to predict the buoyancy driven flows, thermal conditions and species concentrations that develop due to fire. FDS includes predictions of conditions in the gas phase as well as the condensed phase (i.e., solid boundaries). In the gas phase, FDS predicts the fire plume location, heat release rate of the fire, gas temperature and velocity, gas species concentrations, and visibility through smoke. In this study FDS simulations were performed on a

standard x86-Linux cluster with a dual-socket quad-core 2.26 GHz Intel Nehalem processor and 24GB of memory.

The computational domains of the experimental setup were 2.2m high, 2.0 m wide and 2.0 m deep. All domain boundaries were set to an open condition. The ceiling modeled in FDS was 1.22 m x 1.22 m with a thickness of 0.1 m and constructed of gypsum board using the thermo-physical properties provided in Table 2.2. The geometry of the ceiling was prescribed using rectangular obstructions which conforms to the rectilinear grids. The fire burner used in the simulation was 0.3m x 0.3m x 0.1m obstruction. The vents covering the top surface of the burner obstruction were prescribed a constant value of heat release rate per unit area (*HRR*PUA) depending on the simulated fire heat release rate. The fuel for the fire was propane with a CO yield of 0.0 kg/kg and a soot yield of 0.0 kg/kg. To account for the radiative loss from the flames, the radiative fraction was set to a value of 0.45 based on the diameter of the burner and the data provided by Koseki [25]. All FDS simulations were performed using the default turbulence model proposed by Deardorff.

Table 2.2: Thermo-physical properties of ceiling material

Material	Specific heat (kJ/kg-K)	Conductivity (W/m-K)	Density (kg-m3)	Thickness (m)
Gypsum Board	0.9	0.16	790	0.1

FDS simulations results greatly depend on the cell size chosen for the simulation. Floyd et al. [26] recommended that the ratio of characteristic fire diameter and cell size, D*/δx, should be used for the prediction of the optimal grid size, where δx is the computational cell size and D* is defined as

$$D^* = \left(\frac{\dot{Q}}{\rho_\infty c_p T_\infty g^{1/2}} \right)^{2/5} \tag{2}$$

This study used a cell size of D*/δx = 10, which corresponds to a cell size of 0.029 m, 0.029 m, and 0.029 m for the 50 kW fire scenario. This has shown elsewhere [26] to provide converged results on predicting gas temperature and velocity. Gas temperature and velocity were extracted from the simulations by locating a slice file along the centerline of the burner. Gas temperature and velocity reported in the results section are averaged over a 50 second period.

2.5. Analysis and Discussion

Results are shown to highlight the effects of *HRR* and ceiling height. Therefore, gas temperature and velocity were plotted to compare *HRR*, holding relative ceiling heights constant and to compare ceiling heights, holding *HRR*s constant. One way analyses of variance (ANOVA) were also performed on the data to further investigate the main effects of *HRR* and ceiling height on gas temperature and velocity. The analysis was performed with the statistical software package JMP with Type I error rate of 0.05, allowing inferences to be made with 95% confidence. *HRR* and ceiling height were considered ordinal variables. The experimental results were also compared to a simulation using FDS and to existing fire plume correlations.

2.5.1. Gas Temperature Results

2.5.1.1. Effect of Ceiling Height on Gas Temperature

Figure 2.3 compares the average centerline gas temperatures for the different ceiling heights. The elevation above the burner, z, was normalized by $Q^{2/5}$ to highlight the different flame regimes as developed by McCaffrey. Over the range considered, there is no apparent effect of ceiling height on the measured gas temperatures within the continuous flaming region. This corresponds to $z/Q^{2/5}<0.06$ for the 50 kW *HRR* and $z/Q^{2/5}<0.08$ for the 90 kW *HRR*. At elevations close to the burner, the results are within the experimental uncertainties, particularly for the 90 kW fire. The $L_f/H=2$ height is the exception due to its slightly higher temperatures. This result is expected from the unbounded measurements in Refs. [3-5]. The results indicate that the continuous flaming region for the 50 kW *HRR* ends slightly sooner than reported in Ref. [3] at $z/Q^{2/5}=0.06$. As elevation above the burner increases, the gas temperatures differ significantly up to $z/Q^{2/5}= 0.13$ for the 50 kW fire tests. For the 90 kW fire, at $z/Q^{2/5}>0.09$, the gas temperatures are, in general, significantly different, with $L_f/H=0.8$ having lower temperatures than the other ceiling heights. In summary, the analysis reveals that gas temperature has a slight dependence on ceiling height at elevations above the continuous flaming region.

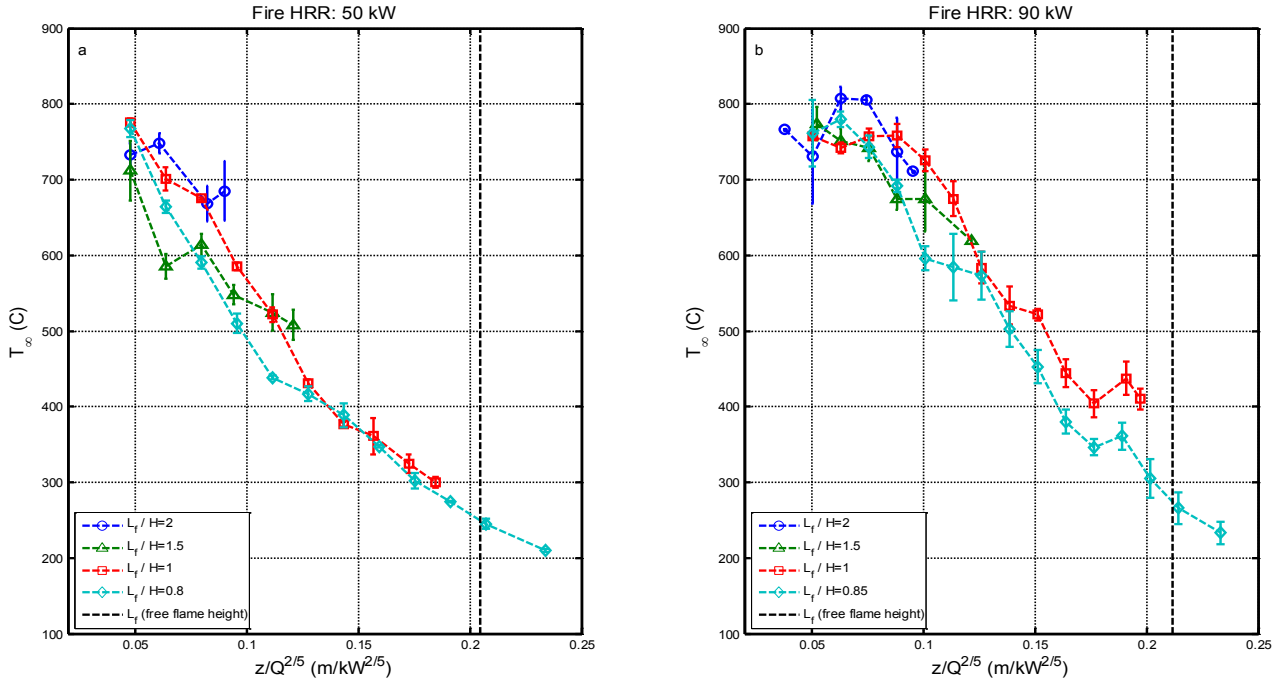

Figure 2.3: Effect of Ceiling Height on Gas Temperature: a) 50 kW, b) 90 kW

2.5.1.2. Effect of HRR on Gas Temperature

Figure 2.4 shows a comparison of the gas temperatures for different *HRR*s at each ceiling height. For the *HRR*s tested, it can be seen that *HRR* does have an effect on the gas temperature within the fire plume. The 90 kW fires produced gas temperatures up to 170°C higher than those measured for the 50kW fire. These larger temperature differences occur mostly as the elevation above the burner increases, indicating that gas temperatures within the continuous flaming region are less dependent on *HRR*. Significant differences in gas temperature were not detected for $z/Q^{2/5}<0.06$, nor at $z/Q^{2/5}=0.09$ for the $L_f/H=2$ case. As expected from unbounded fire plume data [3-5], maximum gas temperatures for each individual *HRR* occurred in the continuous flaming region. The $L_f/H=2$ case consisted of measurements made within the continuous flaming region alone. Therefore, the gas temperatures remain relatively constant with elevation above the burner. This behavior also occurs for the other relative ceiling heights at lower elevations, particularly with the 90 kW fire. Significant differences between gas temperatures of the two *HRR*s were detected within the intermittent region for all ceiling heights. It is within this region that the maximum temperature differences occur. In the plume region, $z/Q^{2/5}>0.2$, the gas temperatures were not detected to be significantly different; however, from Figure 2.4, gas temperature does increase slightly with *HRR*. This result agrees with those of Refs. [3, 4].

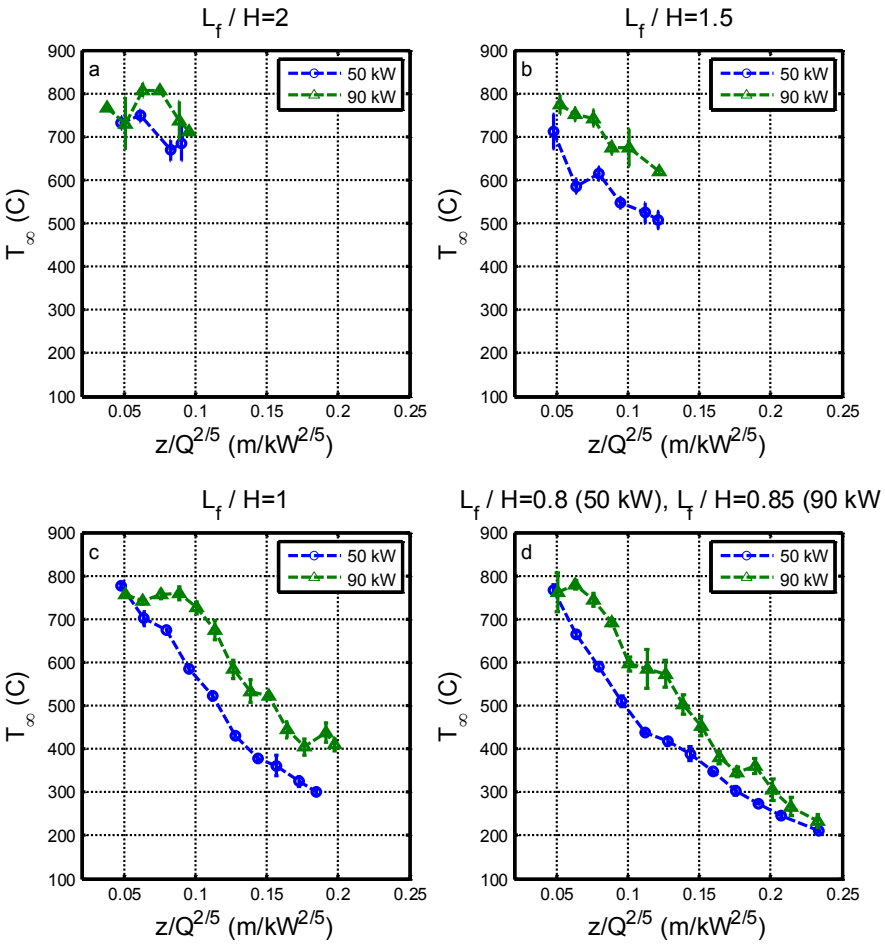

Figure 2.4: Effect of *HRR* on Gas Temperature: a) L_f/H=2, b) L_f/H=1.5, c) L_f/H=1, d) L_f/H=0.85 and L_f/H=0.8.

2.5.1.3. Comparison to FDS Simulation

The gas temperatures from the 0.64 m and 1.51 m ceiling heights were compared with the results from the FDS simulation. The comparisons are shown in Figure 2.5. Overall, the trends in the FDS results predict the data well for all cases. Maximum average gas temperatures for all cases are within 5.74% of each other.

There is some disagreement in the magnitudes of the gas temperatures, particularly for the lower ceiling heights. The trends match with those of the FDS simulations; however, the experimental values are approximately 50-110^{o}C lower. The disagreements between the two data sets are more pronounced at lower elevations. The FDS simulations have a decrease in temperature at elevations approaching the burner surface, which is consistent with the results of You and Faeth [16]. You and Faeth attributed this to differences in burners; however, Beyler attributes it to a region of cooler gas in the fuel rich core of the fire [8]. The FDS simulation also

shows a slight increase in temperature near the ceiling surface. It is believed that this is attributed to circulation eddies occurring near the impingement point when the flames and hot gases turn radially outward towards the ceiling. This behavior was not captured with the aspirated thermocouple probe.

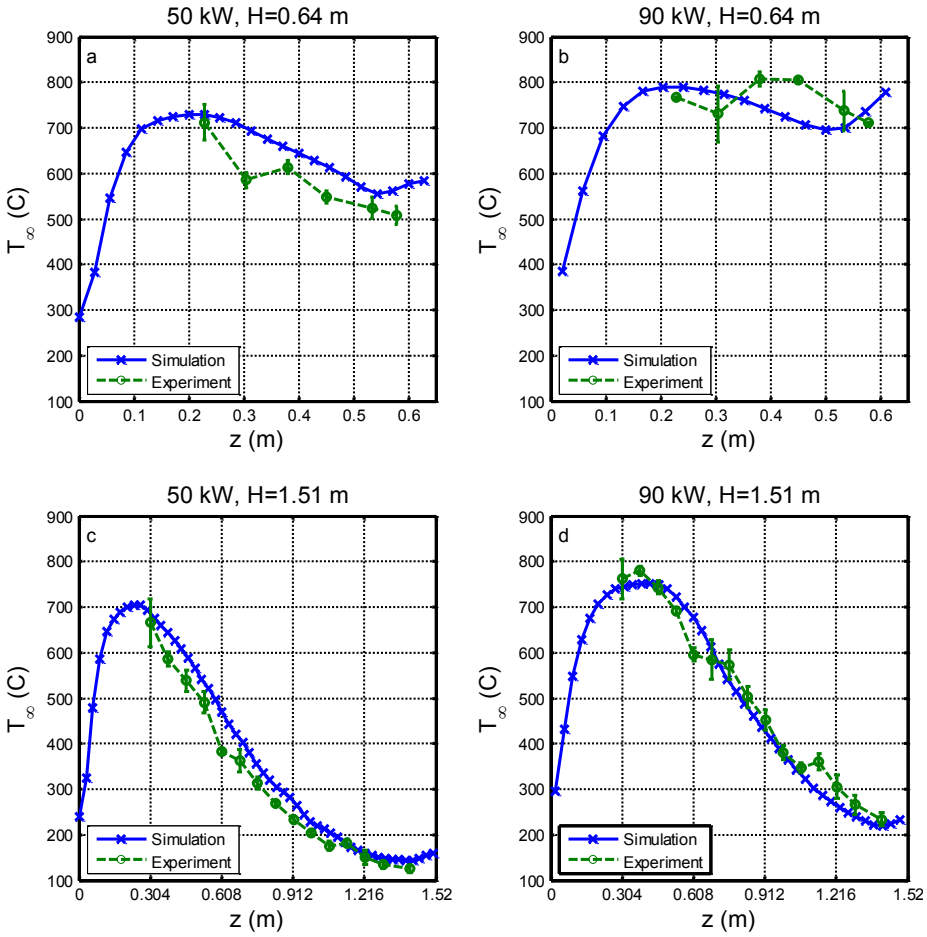

Figure 2.5: Gas Temperature Experimental Results Compared with Simulation Results: a)50 kW, H=0.64 m, b) 90 kW, H=0.64 m, c) 50 kW, H=1.51 m, d) 90 kW, H=1.51m

2.5.2. Velocity Results

2.5.2.1. Effect of Ceiling Height on Velocity

Figures 2.6a and 2.6b present the effect that the presence of a ceiling at different heights has on the fire plume velocities for the 50 kW and 90 kW *HRR* respectively. The elevation above the burner was normalized according to Ref. [3] to highlight the different regimes within the flame. The velocity is low near the burner, increases with z to a maximum, and then decreases as it approaches the impingement surface. A maximum velocity occurs in the

intermittent region of the flame. This marks the end of the continuous flaming region, where more ambient air will be entrained and heated, thus increasing the mass flow rate, and in turn increasing the overall velocity. As the flame approaches the ceiling, its vertical velocity decreases, where it becomes zero at the impingement point.

The effect of ceiling height on velocity is more pronounced than with the gas temperature. Within the continuous flaming region, the ceiling does not have a significant effect on the flow velocities for the various ceiling heights. This corresponds to $z/Q^{2/5}<0.06$ for the 50 kW *HRR*, and $z/Q^{2/5}< 0.08$ for the 90 kW *HRR* (with the exception of $L_f/H=0.8$ for 90 kW). For ceiling heights placed within the flame, the velocity increases as the ceiling height increases. At $z/Q^{2/5}>0.06$ for the 50 kW *HRR*, the velocities at the $L_f/H=1.5$ and 2.0 heights significantly differ from those of the $L_f/H=1$ and 0.8 heights. This indicates that the intermittent region may actually occur at $z/Q^{2/5}=0.06$ rather than 0.08, indicated by McCaffrey [3]. For the ceiling heights placed at the flame height and slightly above the flame height, there is no significant difference until the velocities start to decrease due to the presence of the ceiling, which occurs at $z/Q^{2/5}> 0.14$ and $z/Q^{2/5}> 0.16$ for the 50 kW and 90 kW *HRR*, respectively.

Figures 2.6c and 2.6d show velocity versus elevation relative to ceiling height, z/H, which helped to collapse the data such that the velocity drop off due to the presence of the ceiling could be consolidated. From these plots, it becomes apparent that the velocities drop off significantly around values of $z/H=0.6$ and 0.7 for the 50 kW and 90 kW *HRR*, respectively. This result agrees with the assessment made by McCaffrey [3]. The differences between the maximum velocities according to ceiling height range from 2.0-16% for the 50 kW fire and from 3.1% to 15% for the 90 kW fire. The maximum of each *HRR* occur roughly at the same relative elevation above the burner, between z/H of 0.5 and 0.6 for both *HRR*s.

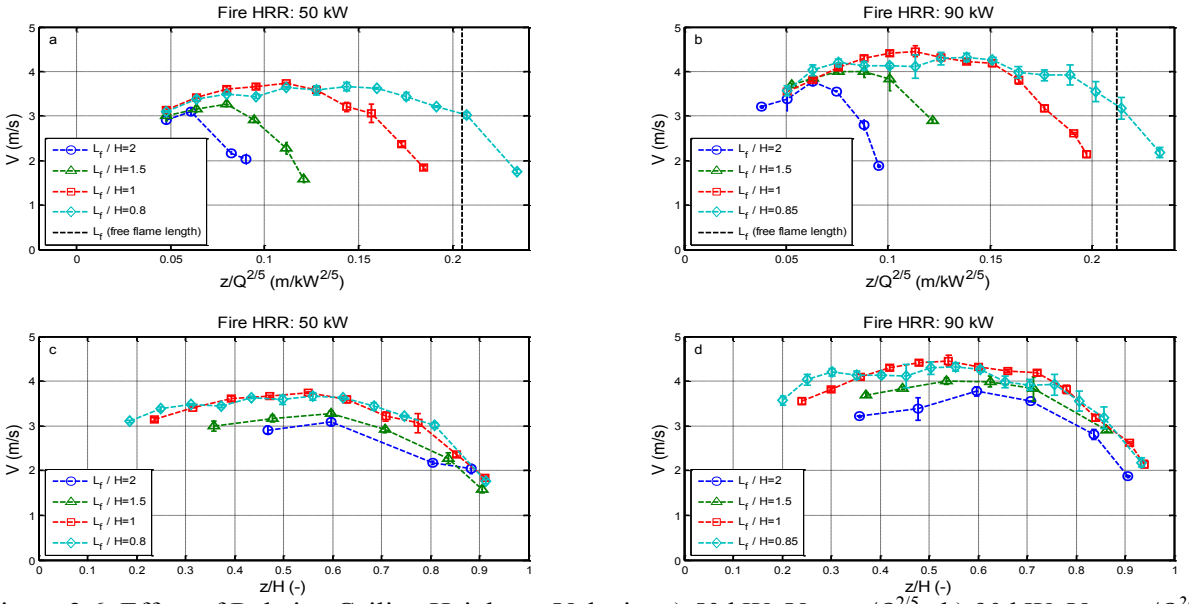

Figure 2.6: Effect of Relative Ceiling Height on Velocity a) 50 kW, V vs. $z/Q^{2/5}$, b) 90 kW, V vs. $z/Q^{2/5}$, c) 50 kW, V vs. z/H, d) 90 kW, V vs. z/H

2.5.2.2. Effect of HRR on Velocity

Figures 2.7 and 2.8 contain comparisons of the vertical velocities for different *HRR*s at each ceiling height. Similar to the gas temperature, velocity increases with an increase in *HRR*. The ANOVA detected that *HRR* caused significant differences between velocities at all elevations for all ceiling heights, with the exception of measurements made in the plume region for L_f/H=0.8 and 0.85. The maximum of each *HRR* occurred in the region of $z/Q^{2/5}$ from 0.06 to 0.14; slightly before and within the intermittent region as defined in Ref. [3]. The difference between each maximum value ranges from 0.66 and 0.73 m/s for all relative ceiling heights. The 90 kW fire has maximum velocities 15.2-18.3% greater than the maximum 50 kW velocities. These results do not agree with the results in Refs. [3, 4] in the continuous flaming region, and therefore the velocities were plotted according to the scaling parameters found in Ref. [3] in Figure 2.8. This plot shows that within the continuous flaming region, velocities are unaffected by *HRR*, but do increase with elevation. Although scaled by *HRR*, there is still a vertical shift present in the data for the two *HRR*s within the intermittent and plume regions for ceiling heights placed within the flames. This indicates that the effect of *HRR* in the fires studied in this research is greater than measured by McCaffrey.

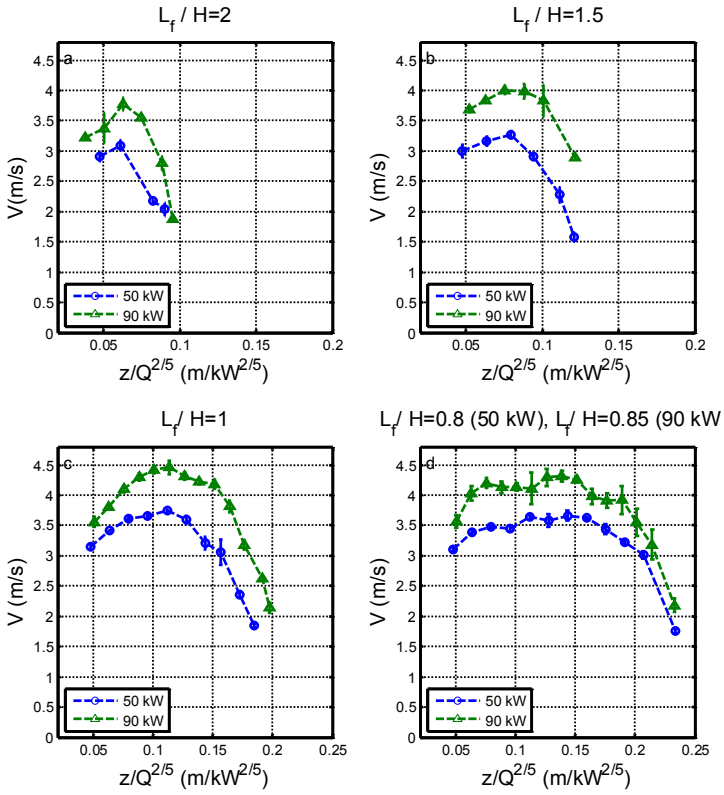

Figure 2.7: Effect of *HRR* on Velocity: a) L_f/H=2, b) L_f/H=1.5, c) L_f/H=1, d) L_f/H=0.85 and L_f/H=0.8.

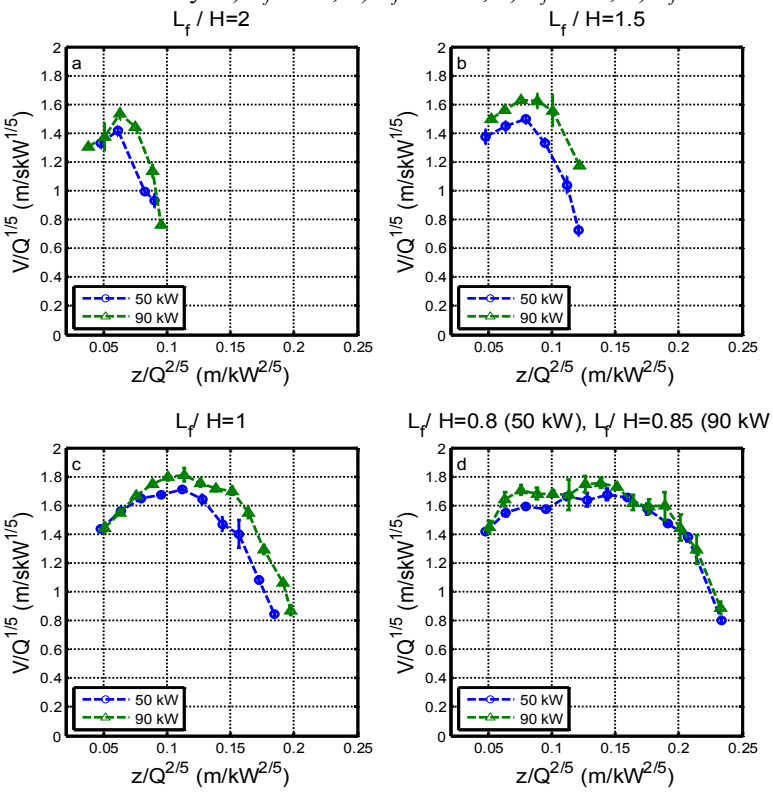

Figure 2.8: Velocities Scaled by parameters given in Ref. [3]: a) L_f/H=2, b) L_f/H=1.5, c) L_f/H=1, d) L_f/H=0.85 and L_f/H=0.8.

2.5.2.3. Comparison to FDS Simulation

The velocities from the two *HRR*s beneath ceiling heights of 0.64 m and 1.51 m were compared with the velocities predicted using FDS. The comparisons are shown in Figure 2.9. The overall trends are the same and the maximum average values are within 11.6% of each other. The largest difference between the maximum measured and simulation results occurred for the 90 kW *HRR* at the 0.64 m ceiling height. Most of the disagreement between the simulation results and the measured averages occurred near the maximum velocities. Overall, the measured data and simulation results compare favorably. The maximum percent difference between the simulation and experimental velocities was 18%; however, when the experimental uncertainty was considered, the percent difference decreased to approximately 13%.

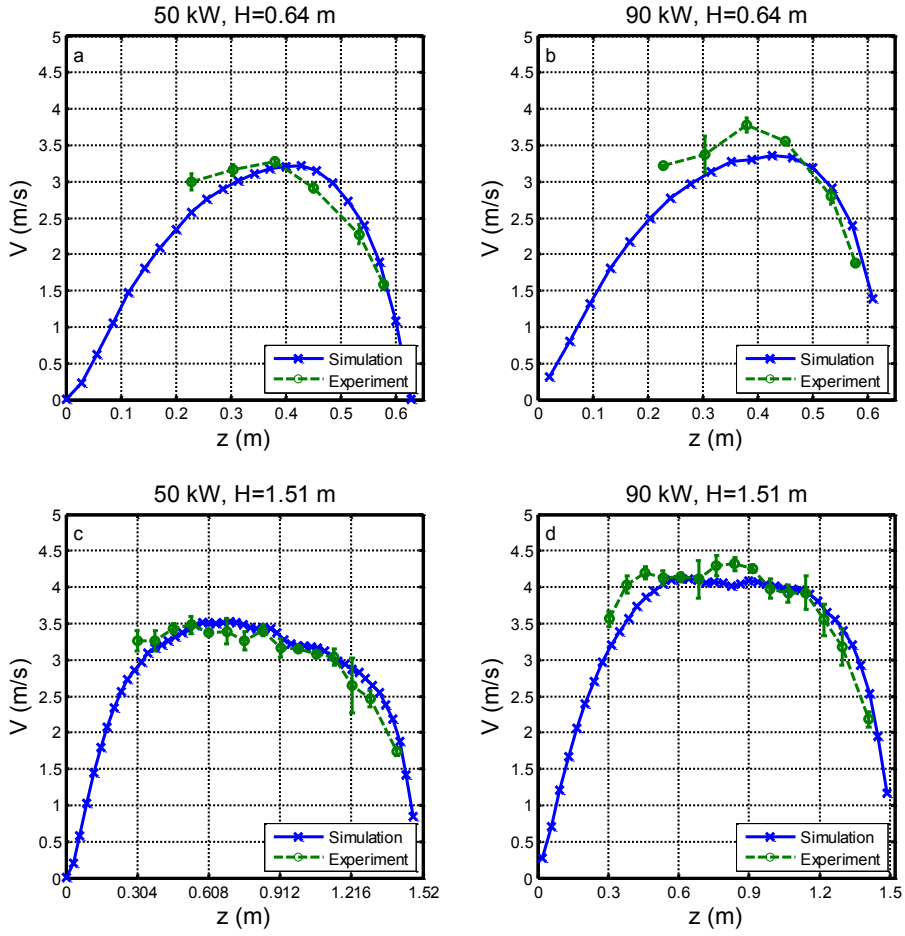

Figure 2.9: Velocity Experimental Results Compared with Simulation Results: a)50 kW, H=0.64 m, b) 90 kW, H=0.64 m, c) 50 kW, H= 1.51 m, d) 90 kW, H=1.51m

2.6. Discussion

2.6.1. Comparison to Correlations Found in the Literature

The gas temperature and velocity results of this work were compared to the work found in Refs. [3-5, 16]. This was done to highlight the differences in each parameter between an unbounded fire plume and a ceiling bounded fire plume. The gas temperature and velocity results were normalized by the parameters discussed in Refs. [3, 5] and plotted according to the correlations developed in each respective work.

Figure 2.10 contains the experimental gas temperature rise measured in this work compared with the correlations and data in Refs. [3, 4, 16]. The gas temperatures agree best with the work of McCaffrey. In the continuous flaming region, $z/Q^{2/5} < 0.08$, the maximum temperatures above ambient are between 700 and 800^{o}C and remain relatively constant for the 90 kW *HRR*. The data measured for the 50 kW *HRR* does not correlate as well. It is shifted slightly to the left, just reaching the maximum temperature region. This indicates that its intermittent region happens sooner than that given by McCaffrey, around $z/Q^{2/5}=0.06$ rather than 0.08. You and Faeth [16] measured a maximum at higher values around 1100^{o}C; however, for values of $z/Q^{2/5}< 0.08$, the temperature rise above ambient decreased monotonically. This type of behavior agrees with the FDS simulation results. You and Faeth [16] attributed this behavior to differences in burner characteristics. Beyler attributed this decrease to a fuel rich core at elevations close to the burner, where lower gas temperatures can be found [8]. You and Faeth [16] also noticed that an increase in the *HRR* increased the slope within this region. Experimental measurements in this work were not made close enough to the burner to capture this behavior. In the intermittent region, the gas temperature rise follows well with that of McCaffrey. It is noteworthy to point out that data from different ceiling heights are not clearly distinguishable when the data is normalized in this way. This further supports the result that ceiling height has a small effect on the gas temperature. Only one ceiling height allowed measurements to be made within the plume region ($z/Q^{2/5}> 0.2$). These measurements follow the relationships with elevation as outlined by McCaffrey.

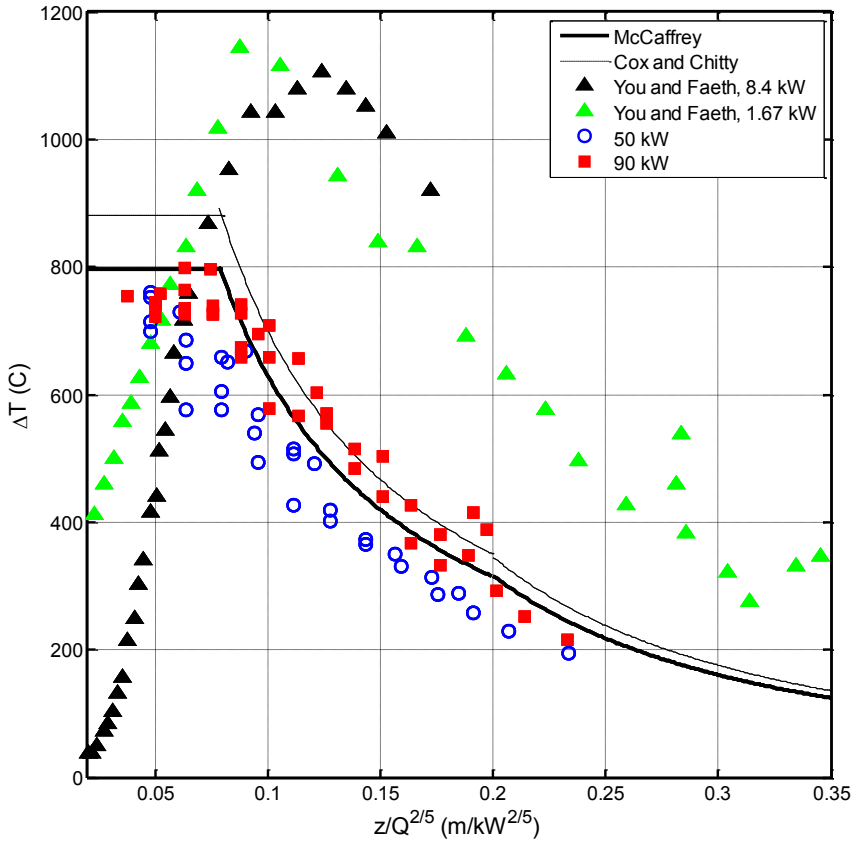

Figure 2.10: Gas Temperature Comparison with McCaffrey[3], Cox and Chitty [4], You and Faeth [16]

Figure 2.11 contains the velocity data measured in this work compared with the correlations in Refs. [3, 4, 16]. The results follow the general trend from Refs. [3, 4]; however, the data is shifted and appears as a family of curves. This is due to the presence of the ceiling causing the flame velocity to decrease as it approaches the impingement point, preventing some of the flame regimes from developing. The velocities in the continuous flaming region for the fire plume impinging on the ceiling increase with elevation as do the correlations from Refs. [3, 4]; however, the bounded data was measured to have a more gradual increase with elevation. A stronger dependence of velocity on the ceiling height is also shown. This, in part, is reflected by the severe drop off in the velocities as the flow reaches the ceiling at z/H values greater than 0.6. In and near the intermittent region is where the velocities reach a maximum, lower than those measured by McCaffrey and Cox and Chitty. These lower values are consistent with the work of You and Faeth [16], with their scaled velocities reaching a maximum near 1.5 m/s. When the ceiling height is above the flame height (L_f /H<1), the velocity remains relatively constant within the intermittent region. As expected, this agrees with the unbounded fire plume data in Refs. [3,

4] due to the ceiling being at an elevation far enough above the flame to not have any significant effect on the fire plume flow field. Note that the velocities severely drop off, before the intermittent region for the first ceiling height, and right after the intermittent region for the highest ceiling height. This is where the flame velocity decreases due to the ceiling presence. As mentioned earlier, this occurs roughly at 60-70% of the ceiling height. The unbounded correlations should not be used within this region. The velocities within the intermittent region in Ref. [16] are not shown to have this trend. Rather, the velocities are monotonically increasing with $z/Q^{2/5}$ up until a $z/Q^{2/5}$ value about 0.25. The diminished velocities due to the presence of the ceiling are not shown in the data from Ref. [16]. You and Faeth attributed the differences to burner design and operating conditions [16].

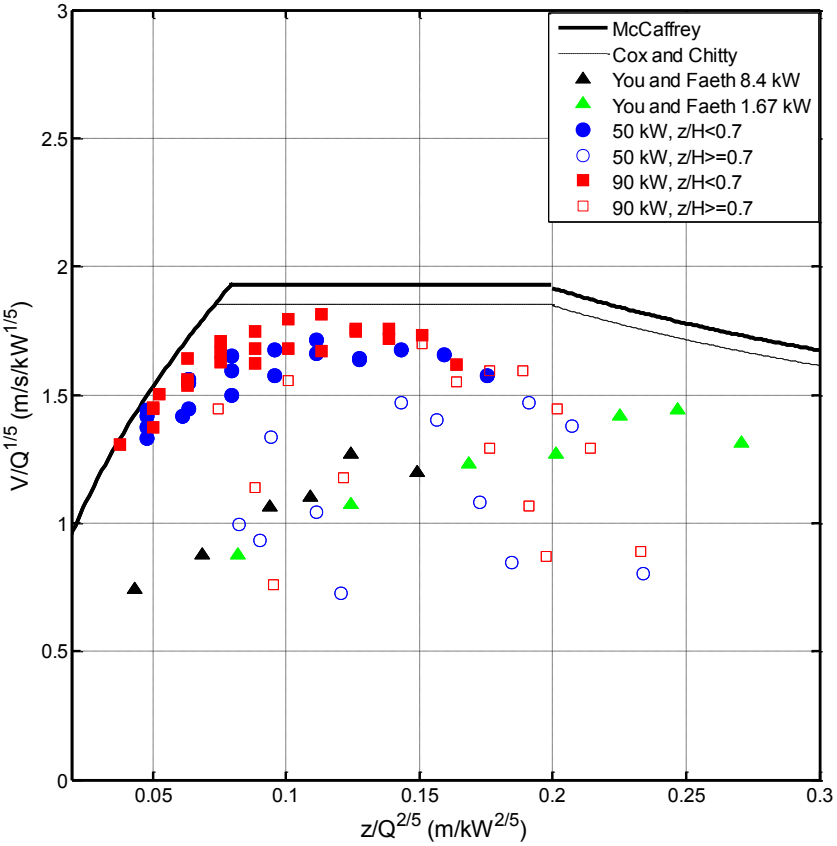

Figure 2.11: Velocity Comparison with McCaffrey [3], Cox and Chitty [4], You and Faeth [16]

Figure 2.12 contains plots of the gas temperatures and velocities measured in this work compared with the correlations in Ref. [5]. Kung and Stavrianidis found that their measurements for $z/Q^{2/5}<0.45$ collapsed better when including the virtual origin, z_o, in their

normalization of z. This corresponds to all of the data measured in this work. Therefore, the virtual origin for these measurements was calculated using a correlation given by Heskestad [27] and the experimental results were plotted accordingly. Explicit correlations were not given in Ref. [5], therefore they are not shown. The results from the normalizing according to Ref. [5] did aide in reducing the spread between the gas temperatures for the two *HRRs*. This helps to explain the shift in the 50 kW HRR from the other correlations. However, normalizing the velocities with the convective heat release rate, Q_c, caused the data from the two *HRRs* to shift in magnitude. This normalization revealed results similar to those previously discussed. The gas temperatures appear to be unaffected by the presence of the ceiling, while the fire plume velocities decreased when the flow approached the impingement point. To fully evaluate this, the effect of varying burner diameters and a larger range of fire sizes should be investigated.

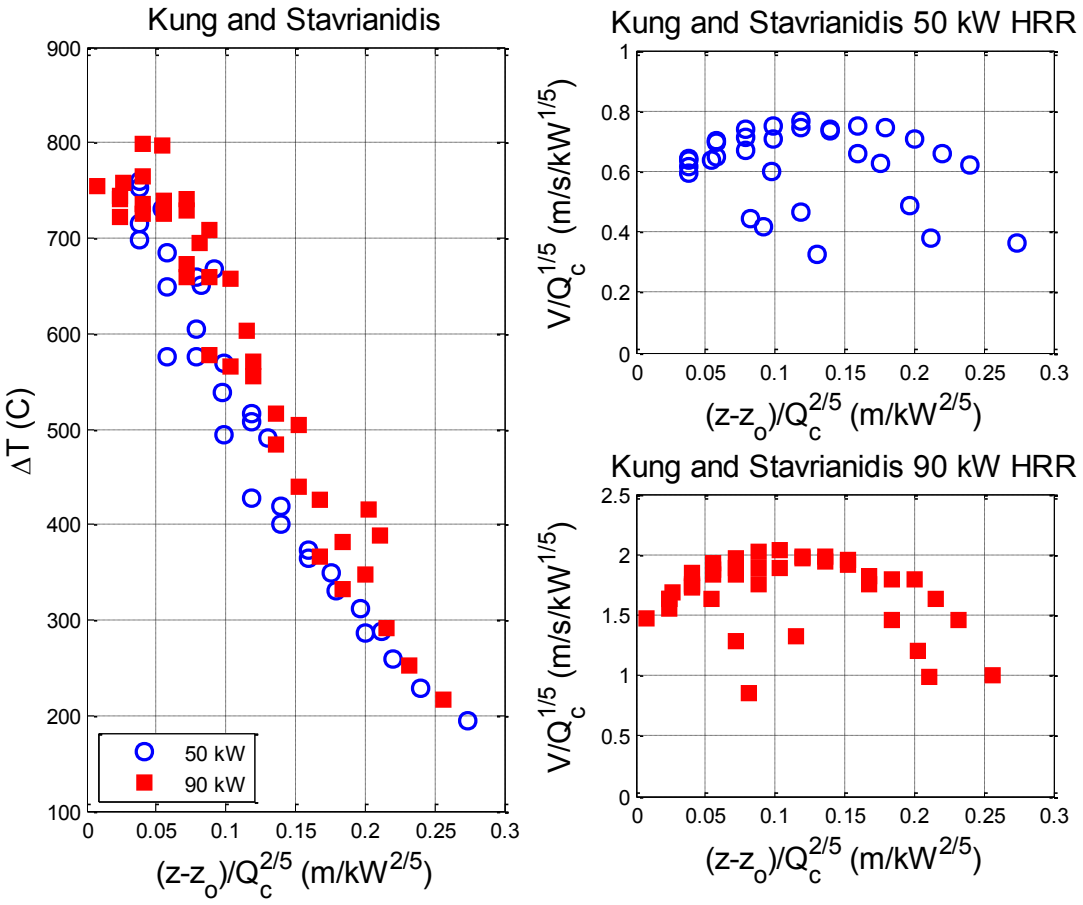

Figure 2.12: Gas Temperature and Velocity Comparison with Kung et al.[5]

2.7. Conclusions

Measurements of time averaged gas temperature and velocity were made along the centerline of a fire plume impinging onto a ceiling. Experiments were performed with a 0.3m square sand burner with propane as the fuel type. It was shown that the gas temperature within the continuous flaming region remained relatively constant, with little dependence on *HRR* and ceiling height. The velocities near the burner increased with z, and were independent of ceiling height, yet had a slight dependence on *HRR*. As elevation above the burner increased into the intermittent region for $z/Q^{2/5}>0.6$ and 0.8, temperature decreased and velocity increased to a maximum. Within the intermittent region of the flame, gas temperature and velocity increased with *HRR*. Velocity increased with ceiling height, while gas temperature decreased slightly with an increase in ceiling. Closer to the ceiling, both parameters decreased as the flame reached the impingement point. The experimental results of this work agree with the correlations developed by McCaffrey, with slightly lower temperatures and velocities. The fire plume correlations can be used as a good approximation for the gas temperature; however, the velocity correlations should only be used up to elevations which are below 60% of the ceiling height. Anything above this region is where the unbounded fire plume correlations break down due to the presence of the ceiling. This substantial effect on the velocities due to the presence of the ceiling had not been discussed in previous work. The comparison between the experimental results and the FDS simulation were favorable, with maximum temperatures within 5.74 % and maximum velocities within 11.6%.

2.8. Acknowledgements

The authors would like to thank Joshua McNeil, Christian Rippe, Joseph Starr, and Akashdeep Singh Virk for their help in the lab and with the propane system.

References

1. Hinkley, P.L, Wraight, H.G.H., Theobald, C.R., The contribution of flames under ceilings to fire spread in compartments, Fire Safety Journal 7 (1984) 227-242.
2. Hasemi, Y., Firesafety of building exposed to a localized fire-scope and experiments on ceiling/beam system exposed to localized fire, in 1st International Conference ASIAFLAM (1995) 351-361.
3. McCaffrey, B.J., Report NBSIR 79-1910, National Bureau of Standards, (1979).

4. Cox, G., Chitty, R., A study of the deterministic properties of unbounded fire plumes, Combustion and Flame 39 (1980) 191-209.
5. Kung, H.C., Stavrianidis, P., Buoyant plumes of large-scale pool fires, in: Nineteenth Symposium (International) on Combustion (1982) 905-912.
6. Alpert, R.L., Turbulent ceiling-jet induced by large-scale fires, Combustion Science and Technology 11 (1975) 197-213.
7. Motevalli, V., Marks, C.H., Characterizing the unconfined ceiling jet under steady-state conditions: A reassessment, in: Proceedings of the 3rd International Symposium on Fire Safety Science (1991) 301-312.
8. Beyler, C.L., Fire plumes and ceiling jets, Fire Safety Journal 11 (1986) 53-75.
9. Evans, D.D., Ceiling jet flows, Society of Fire Protection Engineers Handbook, 2nd Ed., Chapter 4, Section 2, 32-39.
10. Oka, Y., Imazeki, O., Temperature and velocity distributions of a ceiling jet along an inclined ceiling-Part 1: approximation with exponential function, Fire Safety Journal 65 (2014) 41-52.
11. Kung, H.C., Spaulding, R.D., Stavrianidis, P., Fire induced flow under a sloped ceiling, in: Proceedings of the 3rd International Symposium on Fire Safety Science (1991) 271-280.
12. .Kokkala, M.A., Experimental study of heat transfer to ceiling from an impinging diffusion flame, in: Proceedings of the 3rd International Symposium on Fire Safety Science (1991) 261-270.
13. Heskestad, G. and Hamada, T., Ceiling jets of strong fire plumes, Fire Safety Journal 21 (1993) 69-82.
14. Chatterjee, P., Meredith, K.V., Ditch, B., Yu, H., Wang, Y., Tamanini F., Numerical Simulations of Strong-Plume Driven Ceiling Flows in: Draft-Proceedings of the 11th International Symposium on Fire Safety Science (2014).
15. Kung, H.C., You, H.Z, Spaulding, R.D., Ceiling flows of rack storage fires, in: 21st International Symposium on Combustion, The Combustion Institute (1986) 121-128.
16. You, H-Z., Faeth, G.M., An investigation of fire impingement on a horizontal ceiling, Report NBS-GCR-80-251, National Bureau of Standards, (1979).
17. Thomas, P.H., Baldwin, R., Heselden, A.T.M., Buoyant diffusion flames: some measurements of air entrainment, heat transfer, and flame merging, Proceedings of the 10th Symposium on Combustion, The Combustion Institute (1965) 983-996.

18. Rouse, H., Yih, C.S., Humphreys, H.W., Gravitational Convection from a Boundary Source, Tellus 4 (1952) 201.
19. Yokoi, S., Student on the prevention of fire spread caused by hot upward current, Report No. 34 Building Research Institute Japanese Government (1960).
20. Cooper, L.Y., Heat transfer from a buoyant plume to an unconfined ceiling, Journal of Heat Transfer ASME 104 (1982) 446-451.
21. Diller, T.E., Convective Heat Transfer Chapter
22. Blevins, L.G. , Pitts, W.M., Modeling of bare and aspirated thermocouples in compartment fires, Fire Safety Journal 33 (4) (1999) 239-259.
23. McCaffrey, B.J., Heskestad, G., A robust bidirectional low-velocity probe fore flame and fire application, Combustion and Flame 26 (1976) 125-127.
24. J. Floyd, G. Forney, S. Hostikka, T. Korhonen, R. McDermott, and K. McGrattan, Fire dynamics simulator user's guide, Gaithersburg, Maryland, USA (2013).
25. H. Koseki, Large scale pool fires: results of recent experiments, in: Proceedings of the 6th International Symposium of Fire Safety Science (1999) 5-9.
26. J. Floyd, G. Forney, S. Hostikka, T. Korhonen, R. McDermott, and K. McGrattan, Fire dynamics simulator technical reference guide-volume 3: Validation, National Institute of Standards and Technology: Gaithersburg, Maryland, USA, 2013.
27. Heskestad, G., Engineering relations for fire plumes, Fire Safety Journal 7 (1984) 25-32.
28. Cengel, Y.A., Ghajar, A.J., Heat and Mass Transfer Fundamentals and Applications, Fourth Ed., New York, 2010.

3. Partitioning Measurements of Convection and Irradiation Heat Transfer Components from Diffusion Flames Impinging onto Ceilings

Rachel Wasson*, Brian Y. Lattimer, Thomas E. Diller

Department of Mechanical Engineering

Virginia Tech

3.1. ABSTRACT

Recently developed experimental techniques have been applied to quantify the amount of convection and irradiation from an impinging diffusion flame to the stagnation point of the ceiling. Experiments were performed using a 0.3 m square porous sand burner with propane as the fuel type. Fire heat release rates (*HRR*s) of 50 kW and 90 kW and free flame length to ceiling height ratios, L_f/H, of 2, 1.5, and 1 were investigated to determine the effects they might have on the components of heat transfer at the impingement point. Hybrid heat flux gauges were used to measure the heat flux at the impingement point on the ceiling. Gas temperature at the ceiling and velocity of the fire plume were also measured. The convective heat transfer coefficient, *h,* was calculated using four methods; two reference methods and two slope methods. The components of heat transfer at the impingement point were separated using the calculated *h* values. The reference method 2, and both slope methods resulted in *h* values which were in agreement with each other, however the *h* values calculated using reference method 1 resulted in values up to 15.8 times lower than the other methods. These large differences in *h* greatly influenced the separated amount of convection to the ceiling, particularly at the lowest ceiling heights. Convection calculated using the *h* from reference method 1 contributed only 2-5% of the total exposure heat flux at the lowest ceiling heights, whereas with the other methods convection contributed 20-50% of the total exposure heat flux. The limitations of each method are discussed.

*Author for Correspondence:
Rachel Wasson
United States of America
1-505-681-0447
awrach9@vt.edu

NOMENCLATURE

C	Calibration constant (--)	**Subscripts**	
C_p	Heat capacity at constant pressure (kJ/kg-K)	*air-cooled*	air-cooled gauge heat flux
D	burner diameter (m)	*amb*	ambient temperature
h	convective heat transfer coefficient (kW/m^2-K)	*avg*	average
H	Ceiling Height (m)	*b*	bottom surface
HRR	Total heat release rate (kW)	*c*	convective
k	Thermal conductivity (W/m-K)	*conv*	convection
L_f	Free flame length (m)	*diff*	differential heat flux
Δp	Differential pressure (Pa)	*exp*	exposure heat flux
q	Heat flux (kW/m^2)	*film*	film temperature
Pr	Prandtl number (--)	*irr*	irradiation heat flux
Q	Heat release rate (kW)	*meas*	measured heat flux
Ra	Rayleigh number (--)	*non-cooled*	non-cooled gauge heat flux
S	Elevated temperature sensitivity (μV/W/cm^2)	*o*	Standard state heat flux/temperature
S_o	Room temperature sensitivity (μV/W/cm^2)	*s*	top surface
std. dev.	standard deviation	*rr*	reradiation heat flux
T	Temperature (^{o}C or K)	*slug*	slug heat flux
ΔT	Temperature rise above ambient (^{o}C or K)	∞	gas
t	time (s)		
V	Vertical velocity (m/s)		
z	Elevation above burner (m)		
Greek			
δ	thickness (m)		
ε	emissivity (--)		
ρ	density (kg/m$^{3)}$		
σ	Stefan-Boltzmann constant (kW/m^2-K^4)		

3.2. Introduction

Flames impinging onto a horizontal ceiling create high levels of localized heat flux and temperatures within the stagnation region of ceiling structures. These types of localized fires may cause ignition of combustible surfaces, burn through of materials, and aide in the spread of the fire through convective and radiative heat transfer [1,2]. The fire thermal boundary conditions on the ceiling are necessary parameters used in computational fire models to predict the thermal response of the ceiling materials which are exposed to the fire. Well defined boundary conditions provide more accurate predictions of material behavior under the thermal stresses present in a fire.

Fire thermal environments consist of convection from buoyantly driven gases, and radiation from the flames. It is necessary to quantify and understand the heat transfer mechanisms found within this fire scenario, so that advancements can be made in structures and materials which may help to quell the damage caused by these types of fires. In order to quantify the heat transfer components to the surface, the heat flux and the coefficient of convective heat transfer, h, of the surface need to be quantified. Currently, computational codes such as Fire Dynamics Simulator (FDS), estimate the convective heat transfer coefficient using combinations of natural convection and turbulent boundary layer correlations [3]. These types of correlations are estimated to have uncertainties as high as 50% [4] when applied in real world scenarios. In the flaming region where the gas temperature is high, assuming an h of 0.02 kW/m^2-K and a gas temperature 300K above the surface temperature, this magnitude of error in h can result in convective heat flux differences of ±3.0 kW/m^2. Limited work has been done to quantify h through experimental methods for a flame impinging onto a ceiling.

The hybrid gauge is a heat flux gauge which can operate in temperatures up to 1000^{o}C without water cooling [5]. It has been used to experimentally separate the heat transfer components through the calculation of the coefficient of convective heat transfer [6-8]. The focus of this research is to apply these methods in a real fire experiment to determine the heat transfer components from a diffusion flame impinging onto a ceiling.

The majority of heat flux measurements in fire testing are made using water-cooled heat flux gauges such as Schmidt-Boelter or Gardon gauges [9]. These gauges are actively cooled using water-cooling lines which keep the gauge temperature at the temperature of the water used to cool it. When the gauge is cooled to standard temperature conditions (T=298 K), it measures

the standard state heat flux, q_o, and standard state temperature, T_o. Water-cooled heat flux gauges have several drawbacks when used in fire testing. One of these drawbacks is that the water temperature must be kept above the dew point to prevent condensation on the gauge surface. It can also be a challenge to run water-cooling lines to the gauges in some applications. Water-cooled gauges are capable of only measuring the total heat flux to a surface, and therefore cannot be used alone to separate the convective and irradiation components in a fire. This necessitates the use of a correlation for the convective heat transfer coefficient or the use of multiple total heat flux gauges.

In this work, an air-cooled hybrid heat flux gauge is used to provide a reference heat flux and temperature measurement, $q_{meas,air\text{-}cooled}$ and T_{ref}. An air-cooled gauge was selected instead of a traditional water-cooled gauge to avoid any issues involved with condensation forming on the gauge. Without cooling, the hybrid heat flux gauge is capable of measuring the heat flux of a surface at elevated temperatures, $q_{meas\ non\text{-}cooled}$. Energy balances on both the air-cooled and the non-cooled gauge surfaces can be used to relate the two gauge conditions, assuming that they are exposed to the same thermal environment and flow conditions, have the same emissivity, ε_s, and are gray and diffuse.

$$q_{meas,air-cooled} = \varepsilon_S q_{irr} - \varepsilon_S \sigma T_{ref}^4 + h\left(T_\infty - T_{ref}\right) \tag{1}$$

$$q_{meas,non-cooled} = \varepsilon_S q_{irr} - \varepsilon_S \sigma T_S^4 + h\left(T_\infty - T_S\right) \tag{2}$$

The first term on the right hand side of the equation is the absorbed irradiation into each surface, the second term is the amount of reradiation from the surface, and the third term is the amount of convection to each surface. It is assumed that the gas temperature and the irradiation are the same between the two surfaces, and ε and h are independent of the surface temperature. Solving Equation (1) for q_{irr}, substituting into Equation (2) and rearranging leads to the following expression relating the measured heat flux of the elevated temperature surface to the reference heat flux of the air-cooled surface [6,10,11],

$$q_{meas,non-cooled} = q_{meas,air-cooled} - \varepsilon_S \sigma\left(T_S^4 - T_{ref}^4\right) - h\left(T_S - T_{ref}\right) \tag{3}$$

The most common approach to experimentally quantify the amount of convection and irradiation to a surface is through the use of two heat flux gauges. In one method, the two gauges are coated to have different, but known emissivities. This method requires an energy balance on both gauges. If the total heat flux to the surface is measured, the energy balances can

be used to solve for *h*. Lattimer et al. [12] and Lennon and Silcock [13] used this approach. Lattimer et al. used two thermopiles with different emissivities, while Lennon and Silcock used two thin plate devices; one coated in gold foil and one painted black. Results using this method compared reasonably well with a reference radiometer for middle to high range heat flux values, however, low heat fluxes resulted in larger discrepancies in the radiation component of heat transfer [13]. A common problem encountered using two gauges with different emissivities is that when using sooty fuels the gauges with low emissivities become coated with soot as a result of incomplete combustion [13]. This increases the surface emissivity of the low emissivity gauge during the test and therefore the method cannot be used to effectively separate the heat transfer components.

Another method to quantify the heat transfer components within a fire is to use a total heat flux gauge in conjunction with a windowed radiometer. The radiometer will only measure the irradiation heat flux component; therefore, the two signals can be subtracted to provide the convective heat flux. Blanchat et al. [14] used this methodology with a Schmidt-Boelter gauge and a windowed radiometer in a fully turbulent methane pool fire. Nakos and Keltner [15] used plate calorimeter temperature data in conjunction with an inverse heat conduction code to calculate the net absorbed heat flux in a large jet fuel pool fire. Windowed radiometers were embedded into the plate calorimeters to measure the irradiation to the surfaces. These measurements, along with a series of energy balances, were used to solve for the convective portion of heat transfer and thereby separate the heat transfer components. Blanchat et al. found radiative portions of 60% for locations in the flame, and 25% for those out of the flame [14]. Nakos and Keltner found that in large pool fires, radiation contributed approximately 80-90% of the total heat flux [15]. Windowed gauges are also known to have problems with soot formation, and therefore require the use of gas purging to prevent soot from forming on the window. The window transmittance also needs to be quantified, and the two gauges have to be placed close to each other such that the assumption of equal irradiation can be satisfied. These are significant challenges associated with using this method.

Zhang and Delichatsios [16] used a 3D inverse heat conduction algorithm along with Gardon gauge heat flux and temperature measurements of a steel plate surrounded by insulation to numerically solve for *h* in under-ventilated enclosure fires. The first method calculated a time invariant *h* through the use of energy balances between a Gardon gauge and the steel plate. A

value for *h* was assumed and the error between measured and calculated temperatures was minimized to provide an optimal *h*. The second method calculated a time dependent *h* using energy balances on the steel plate and insulation and a predictor-corrector method to estimate the incoming heat flux and conduction losses. High, low and medium heat flux levels were tested. The initial values of the time dependent method were inaccurate due to small temperature difference between the two surfaces in which the energy balances were taken [16]. Low *h* values were calculated with averages between 0.011-0.015 kW/m^2-K [16]. Higher heat fluxes resulted in lower *h* values. The methods were particularly sensitive to the heat flux measurement accuracy, with relative differences of up to 17% in the calculated *h* value for a ±0.005 kW/m^2-K change in heat flux [16].

Vega et al. [6-8] developed a reference method and a slope method to experimentally quantify *h* using the hybrid heat flux gauge without water cooling. Experiments were performed in a cone calorimeter [6,7] and with an apparatus designed to control the amount of convection and radiation to the gauge surface [8]. The separation of the heat transfer components was achieved through the use of Equation (2) in conjunction with gas temperature measurements and heat flux measurements from the hybrid gauge. Vega et al. showed good agreement between both methods and with correlations appropriate for the various test configurations. This methodology requires the use of only one heat flux gauge. It also provides a direct value of *h,* providing a more detailed thermal boundary condition on the surface of interest, without the need for a correlation. The methods used to calculate *h* also do not require the use of a gas temperature, thereby avoiding the errors associated with making measurements of gas temperature.

Work has been done to quantify the amount of convection and irradiation in a fire plume impinging onto a ceiling. Cooper [17] and Alpert [18] focused on determining the convective heat transfer to a ceiling placed within the plume region of the fire, i.e. above the flames. Cooper developed formulae for estimating *h* and the amount of convection to the ceiling from buoyant fire plumes both inside and outside the stagnation region through the use of works developed by You and Faeth [19-22] and Donaldson et al. [23]. Alpert focused on the ceiling jet region of the flow above the flames and used the integral method with boundary layer theory [18]. He applied the Boussinesq approximation, where gas density differences are small. Both of these works

were conducted for ceiling heights much larger than the flame heights, i.e. in the plume region of the fire.

You and Faeth [19-22], and Kokkala [24] separated the components of heat transfer in a diffusion flame impinging onto an unconfined ceiling. They used a similar approach as Refs. [12, 13], however, rather than solving explicitly for h, they simply subtracted the convection heat flux measured by a foil coated gauge, from the total heat flux obtained with a high emissivity gauge. You and Faeth measured the heat flux at the plume and flame impingement point for burner diameters of 55 mm [19] and 10-76 mm [20], ceiling heights of 410 mm [19] and 60-940 mm [20] with *HRR*s of 1.67, 8.41 kW [19] and 0.05-3.46 kW [20]. Measurements were made in the early stages of the fire, when radiation losses were small and convection was significant. Kokkala [24] measured the total heat flux at the impingement point of a 1 m diameter ceiling. A burner with a 64 mm diameter was used with methane as the fuel type. Hasemi [2] did not separate the components of heat transfer; however, he measured the total heat flux at the stagnation point of the ceiling. He used a 1.82 m square ceiling with 0.3 and 0.5 m square porous burners with propane as the fuel type. Ceiling heat fluxes were measured with water-cooled Schmidt-Boelter gauges and gas temperatures with Type K thermocouples. Weng and Hasemi [25] developed a model to separate the convection and radiation components through a series of energy balances on the upper and lower surfaces of a ceiling exposed to a diffusion flame. Round porous burners with 0.3- 1.0 m diameters were used with propane as the fuel [25]. Water-cooled Schmidt-Boelter gauges measured heat flux at the impingement point and radially outward from it.

You and Faeth [19-22] correlated stagnation point heat fluxes with ceiling height, *HRR*, *Pr* and *Ra* numbers using the impinging jet and plume theories of Sibulkin [26], Donaldson et al. [23], and Rouse et al. [27] for $L_f/H<1.5$. You and Faeth found that the measured stagnation point total heat flux decreased for L_f/H greater than1.5. This was attributed to the impingement of the core region of the flame on the ceiling, which was previously measured to have lower velocities and temperatures, thus decreasing the heat transfer to the ceiling [19]. For the larger fire size, 30% of the total heat transfer was attributed to radiation, however for the majority of the tests, radiation contributed under 20% for $L_f/H<1$ [19, 20]. The stagnation point heat fluxes were determined to be independent of fuel type and L_f/H was not measured to have an effect on the stagnation point heat flux for $L_f/H< 1.5$ [20]. Kokkala [24] found that the maximum stagnation

point heat flux occurred in the $1.5<L_f/H<3.5$ region, with a value of 60 kW/m^2. Inside the flaming region, radiation contributed roughly 40% to the total heat flux and reached a maximum of 50-60% near the average flame height [24]. Overall, Kokkala's data matched well with You and Faeth's [20], with the exception of the intermittent and flame regions. This was attributed to the jet-like nature of the flame in Kokkala's experiments [24]. Hasemi [2] measured the steepest change in the stagnation point heat flux within the region of $1<L_f/H<2.5$, where it reaches a maximum of 80-100 kW/m^2. He also observed larger heat fluxes at smaller ceiling height to burner diameter ratios, H/D. This was thought to be caused by the increase of irradiation within this region [2]. Hasemi's region of steepest increase in heat flux was slightly different from Kokkala. This difference was attributed to the smaller diameter burner used by Kokkala [2]. Weng and Hasemi [25] used a correlation formulated by Cooper [17], in conjunction with experimental data to quantify h within the stagnation and ceiling jet regions of the flow. They reported that the convection heat transfer is often several times larger than the net heat transfer, particularly close to the stagnation point [25]. Experimental measurements compared well with model predictions, for low to medium heat flux values only. The model overestimated the convection heat flux within the stagnation region. This was attributed to inaccuracy in the estimated h due to a lack of experimental data within the stagnation region [25].

All of the above mentioned techniques, require the use of two heat flux gauges, increasing the intrusiveness of the measurement and requiring that both gauges have the same irradiation and convective coefficient of heat transfer. They also require using water-cooling lines and windowed radiometers, further complicating the measurement process. Problems were also encountered with soot development on gauge surfaces [13, 19-22, 24]. The inconsistencies between the fire plume impingement data calls for more analysis to be done within this region. You and Faeth's work [19-22] was performed on a very small scale, and therefore may not be valid in larger fire scenarios. The discrepancies between Kokkala's and You and Faeth's data in the flaming and intermittent region raise concern when dealing with flame impingement. Weng and Hasemi [25] was the only study which attempted to directly calculate h for an impinging flame; however, their model overestimated the convective heat flux in the stagnation region. Further measurements are required to quantify h within the stagnation region, and thus separate the convection and irradiation components of heat transfer to the ceiling. A more detailed study

on the effect that ceiling height and *HRR* may have on the stagnation point heat flux is necessary to further understand the thermal insult experienced by the ceiling.

This research focused on expanding upon the work of Vega et al. [6-8], in determining *h* experimentally for a propane diffusion flame impinging onto a ceiling. Hybrid heat flux gauges were used to measure the ceiling heat flux. The existing reference and slope methods were modified, which added two more methods for calculating *h*. Fire heat release rate (*HRR*) and ceiling height, *H*, were varied to investigate the roles they play in the contribution of convection and radiation heat transfer in an impinging flame. These measurements quantify the thermal boundary conditions at the extreme environment of the impingement region.

3.3. Experimental Methods

A series of experiments were performed with a propane diffusion flame impinging onto a ceiling. Measurements of heat flux and gas temperature were made at the impingement point of the ceiling along with measurements of differential pressure and gas temperature within the fire plume used to calculate the velocity of the flame. A picture of the setup is shown in Figure 3.1.

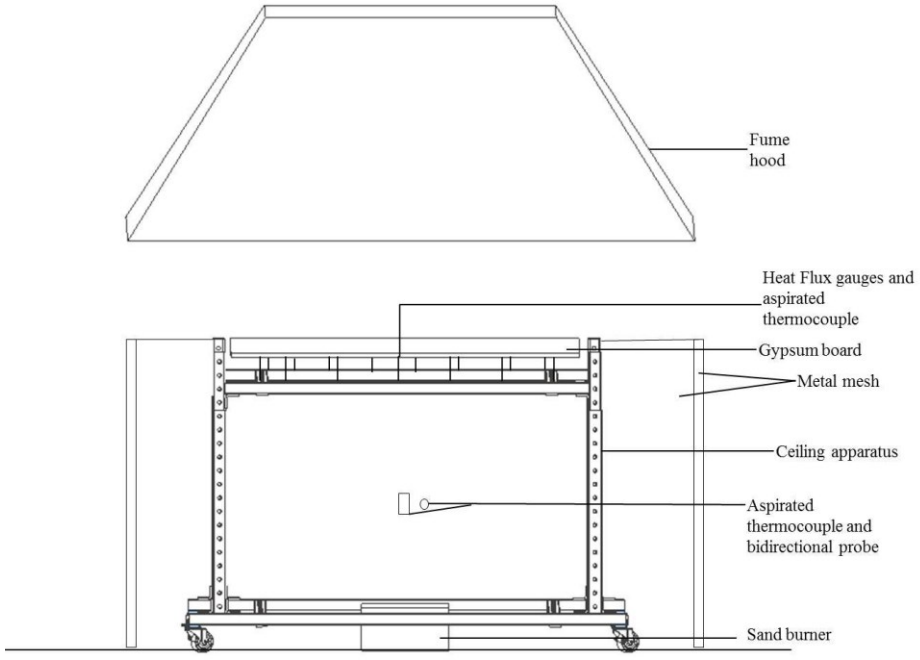

Figure 3.1: Experimental Setup

The locations of the various gauges from a top view are shown in Figure 3.2, where the x marks the center point of the ceiling. The heat flux gauge edges were equally spaced 19 mm

apart from the center of the ceiling. This resulted in the air-cooled gauge and non-cooled gauge being 25.4 mm and 31.8 mm from the center of the ceiling, respectively. The gas temperature probe was placed at the center of the ceiling, approximately 25.4 mm from the bottom ceiling surface. The velocity probe was placed 12.7 mm from the edge of the non-cooled heat flux gauge, which translates to 63.5 mm from the center of the ceiling. A second gas temperature probe was placed along the right hand side of the velocity probe. It was expected that this placement of the velocity probe would result in lower velocities than the centerline velocity, since the probe is essentially in the wings of the flame, where the flame is more intermittent. *HRR* and ceiling height were varied to capture any effects these parameters might have on the components of heat transfer within the impingement region.

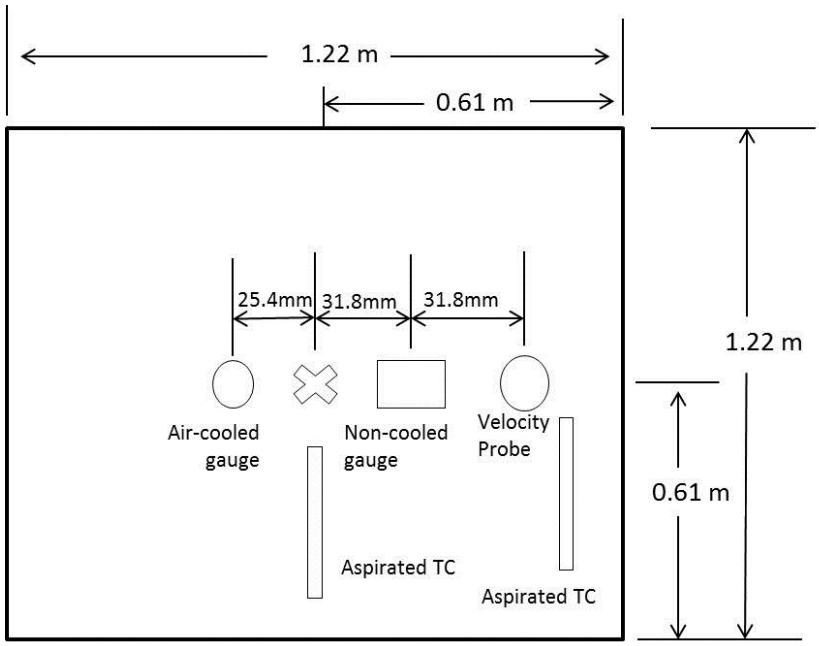

Figure 3.2: Top View of Measurement Locations Relative to Ceiling

3.3.1. Burner and Experimental Apparatus

Experiments were conducted using a 0.3 m square porous sand burner with a height of 0.15 m, with the burner located on a concrete floor. Propane gas supplied to the burner was set using an Alicat MC-100 mass flow controller with an accuracy of ±0.22% full scale. This type of burner setup generates a steady-state diffusion flame, which simulates the characteristics associated with a naturally occurring fire.

An apparatus was designed to hold a square ceiling over the burner. As illustrated in Figure 3.1, it consisted of telescoping Unistrut® tubing to allow for adjustable ceiling heights. The apparatus was designed to accommodate ceiling heights up to 1.51 m above the burner surface. For these experiments, the ceiling consisted of a 1.22 m square piece of 15.9 mm thick, Type X, fire-resistant gypsum board. The ceiling is supported by 127 mm long, 6.3 mm diameter bolts to reduce the amount of heat transferred by conduction from the frame to the ceiling, and to provide a flow path for the smoke to flow out from under the ceiling. One layer of steel diamond screen, with 6.35 x 12.7 mm hole size, was placed around the entire experimental setup to reduce disturbances caused by air drafts in the test room.

3.3.2. Heat Flux

Air-cooled and elevated temperature, non-cooled surface measurements of heat flux were made at the impingement point of the flame on the ceiling. These measurements were made with a hybrid heat flux gauge [5, 28], shown in Figure 3.3.

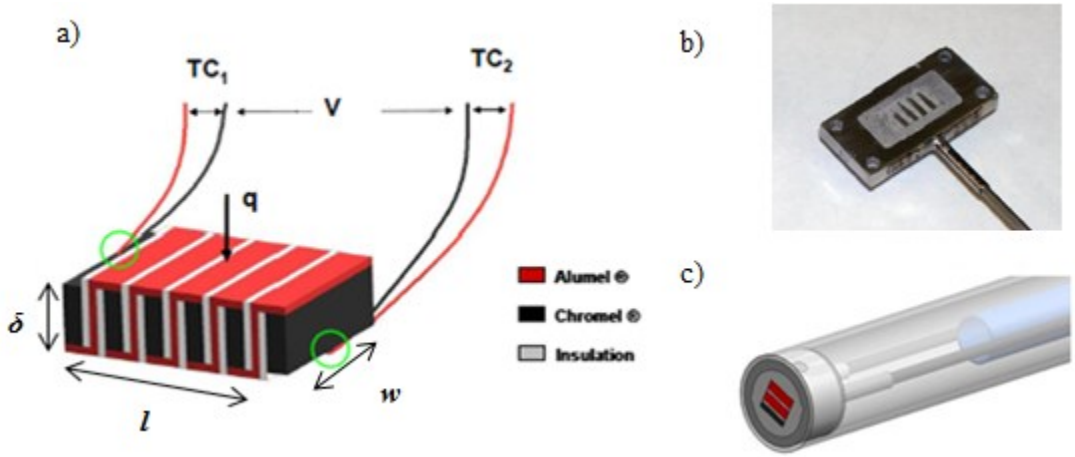

Figure 3.3: Hybrid Heat Flux Gauge design, a) Hybrid heat flux gauge thermopile design with attached thermocouples, where TC_1=Ts and TC_2=Tb Dimensions for the thermopile are l=9.65 mm, w=5.08 mm, and δ=3.18 mm, b) non-cooled configuration, Housing dimensions are l=25.4 mm, w= 12.7 mm, and h =3.18 mm, c) air-cooled configuration, diameter of 12.7 mm

The gauge uses a thermopile, shown in Figure 3.3a, consisting of Type K thermocouple alloys to generate a voltage signal proportional to an applied heat flux. The gauge directly outputs a differential voltage signal, a top surface temperature and a bottom surface temperature. The elevated surface temperature heat flux was measured using the non-cooled gauge configuration shown in Figure 3.3b (Ref. [36]). The non-cooled hybrid gauge is capable of

measuring heat fluxes at temperatures over 1000°C without water cooling [5]. The thermopile for the non-cooled configuration is placed in an Inconel housing which has four holes for direct mounting of the gauge onto a substrate. In this study, the non-cooled heat flux gauge was surface mounted onto the gypsum ceiling. A reference surface heat flux was measured with an air-cooled configuration of the hybrid gauge, shown in Figure 3.3c. The air-cooled gauge thermopile is contained in a plug housing which is press fit into a stainless steel cylindrical body, fit with an air inlet and outlet. Within the body is an internal cooling line, placed 25.4 mm from the back side of the thermopile, which supplies compressed air to the back side of the gauge. An air-cooled configuration was selected to avoid any issues of condensation forming on the gauge surface associated with water-cooled heat flux gauges. The air-cooled gauge was fed through the ceiling and placed at the same depth below the ceiling as the non-cooled gauge.

The hybrid heat flux gauge operates as a differential heat flux gauge and as a slug calorimeter. For differential measurements, the heat flux through the gauge is determined using the one-dimensional version of Fourier's Law. This heat flux is proportional to the direct voltage output of the gauge divided by the elevated gauge sensitivity, S. The differential heat flux can be written as,

$$q_{diff} = \frac{k\left(T_s - T_b\right)}{\delta} = \frac{Voltage}{S} \tag{4}$$

where k is the thermal conductivity of the gauge materials and δ is the thickness of the gauge. This type of measurement requires that the gauge be mounted onto a good heat sink to provide for a temperature difference across the thermal resistance of the gauge.

Slug calorimeters were designed to measure the amount of thermal energy stored in a slug of material as a function of time. A transient energy balance is performed on the gauge and the heat flux stored by the gauge becomes,

$$q_{slug} = \rho C_p \delta \frac{dT_{avg}}{dt} \tag{5}$$

where $\rho C_p \delta$ is the thermal mass per area of the gauge and dT_{avg}/dt is the temperature derivative with respect to time taken using the average of the top and bottom gauge surface temperatures. This type of measurement requires transient data and cannot be used in a steady-state environment. The hybrid heat flux method, derived in Ref. [28], combines the differential and slug responses to calculate the net heat flux into the gauge surface.

$$q_{meas} = q_{diff} + \tfrac{1}{2} q_{slug} \tag{6}$$

The hybrid gauge can therefore be used in both steady-state and transient environments. This approach makes the gauge relatively insensitive to backing material as opposed to traditional differential and slug gauges [28].

The hybrid gauge requires calibration for both the room temperature sensitivity and the thermal mass per area of the gauge. The differential room temperature sensitivity, S_o, is then used to determine the elevated temperature gauge sensitivity, S. This was determined in Ref. [29] to be

$$S = S_o\left[1 + A\left(T_{avg} - 273\right) + B\left(T_{avg} - 273\right)^2 + C\left(T_{avg} - 273\right)^3 + D\left(T_{avg} - 273\right)^4\right] \tag{7}$$

where, the polynomial coefficients are A=3.4923x10^{-4}, B=1.0238x10^{-6}, C= -3.5056x10^{-9}, and D=1.9126x10^{-12}. An elevated gauge temperature sensitivity is required due to the fact that the gauge thermal properties change as a function of temperature. However, since all hybrid heat flux gauges are made of the same material, with the same dimensions, S does not change from gauge to gauge and therefore Equation (7) can be used for all hybrid gauges. Thus, only a room temperature calibration is required to determine S_o for each gauge. Calibration procedures and results for the gauges used in this experiment can be found in Appendix B.

In preliminary experiments, it was found that the gauges became covered in carbon soot during the test due to the incomplete combustion of the propane gas. Therefore, the soot-covered gauge surface emissivity had to be characterized prior to the experiments. The emissivity was determined to be 0.8 through a radiation calibration with the gauge exposed to a halogen lamp. The data for the emissivity can be found in Appendix C.

3.3.3. Gas Temperature

Gas temperature is required to separate the heat transfer components near the gauge surface according to Equations (1) and (2). Therefore, gas temperature was measured at the impingement point, between the two gauges as shown in Figure 3.2. Gas temperature was also necessary to determine the elevated temperature density used in velocity calculations. Measurements of gas temperature were made with aspirated thermocouple probes to minimize radiation errors associated with using bare bead thermocouples [30]. As suggested in Ref. [30], aspirated thermocouples were made using a bare bead Type K thermocouple, with a 0.254 mm diameter Inconel sheathed wires, placed into a 6.35 mm diameter stainless steel tube attached to

a pump. The pump drew air over the bead at a velocity of ~15 m/s, creating a convection dominated environment thereby reducing radiation effects on the bead. The thermocouple bead was located along the centerline of the tube, 19 mm from the tube inlets. Data was collected using a National Instruments 9213 thermocouple module at a sampling rate of 9 Hz.

3.3.4. Velocity

The velocity within the impinging fire plume can be used to provide a reference measurement for the amount of convection present within the fire. Differential pressure was measured with a 19 x 50 mm bi-directional probe [31]. Measurements were made within the fire plume at elevations above the burner where the velocity was expected to reach a maximum as previously determined in Chapter 2 and shown in Table 3.1. The bi-directional probe was placed 12.7 mm to the right of the non-cooled hybrid gauge (Figure 3.2) to prevent it from disturbing the flow to the heat flux gauges. The bi-directional probe was connected to a Setra Model 264 differential pressure transducer with a range of ± 62.3 Pa, and an accuracy of 0.22 % full scale. Data was collected using a National Instruments 9205 module at a sampling rate of 200 Hz.

Velocities were calculated from the differential pressure measurements according to the methodology outlined in Ref. [31]. Using the Bernoulli equation, and assuming pressure effects on density are negligible, the velocity can be calculated as follows,

$$V = \frac{1}{C}\sqrt{\frac{2\Delta p}{\rho}} \tag{8}$$

where C is a calibration constant determined in Ref. [31]. For this work, C was set to 1.08, corresponding to higher Reynolds numbers. The gas temperature measurements were used to determine the elevated temperature density in Equation (8).

Table 3.1: Maximum Velocity Elevations

	50 kW	**90 kW**
Relative Ceiling Height Above Burner, Lf/H	**z (m)**	**z (m)**
2	0.3048	0.381
1.5	0.381	0.457
1	0.533	0.686

3.3.5. *Test Matrix*

The effect of *HRR* and ceiling height on the components of heat transfer was investigated in this series of experiments. A summary of the test matrix is provided in Table 3.2. Fire *HRR*s of 50 kW and 90 kW and ceiling heights of 0.49-1.28 m were used in this study to produce a range of free flame lengths to ceiling height ratios, L_f/H. Free flame lengths, L_f, were calculated based off a correlation developed by Hasemi [2]. Free flame lengths to ceiling height ratios, L_f/H, of 2, 1.5, and 1were chosen to better capture the changes in h, where heat flux has been previously measured to change [2].

Table 3.2: Test Matrix

	Ceiling Height Above Burner, H (m)	
Relative Ceiling Height Above Burner, L_f/H	**50 kW (L_f=0.98 m)**	**90 kW (L_f=1.28 m)**
2	0.49	0.64
1.5	0.64	0.85
1	0.97	1.28

A custom design of experiments was generated to look at the main effects that the above levels of fire size and ceiling height have on the components of heat transfer from the impinging flame to the ceiling. This design was performed using the statistical software package, JMP. A custom design was chosen over a more classical experimental design to allow for flexibility in the treatment definitions and levels, the necessary effects the treatments may have on the data, and the total number of experimental runs. JMP optimizes the design taking all of these into consideration, while still providing the necessary power to make inferences on the desired effects. Three repetitions for each test configuration were performed and the order in which they were conducted was randomized. The randomization was intended to dampen any effect external thermal conditions, or conditions in the lab might have on the diffusion flame.

3.3.6. *Experimental Procedure*

Prior to each test, a fire was run to coat the gauge surfaces with soot. This was done to minimize the change in emissivity due to the incomplete combustion of propane. The gauges were placed in the center of the ceiling as shown in Figure 3.2 and the ceiling height was adjusted to 0.86 m above the burner. The center of the burner was aligned with the center of the

ceiling using a plumb bob. A 50 kW fire was run for approximately 15 minutes to provide a sufficient layer of soot on the gauges. After the gauges were covered in soot, the gauges and ceiling were allowed to cool down to room temperature. The bi-directional probe and the aspirated thermocouple adjacent to it were then adjusted to the appropriate elevation above the burner and placed beside each other, 12.7 mm from the center of the ceiling using the plumb bob. Prior to ignition of the burner for a test from the test matrix, the compressed air line to the air-cooled heat flux gauge was regulated to a pressure of 276 kPa. Once air-cooled gauge temperatures stabilized, a two minute baseline was recorded. The propane mass flow was then set to achieve the desired fire size and the burner was lit to provide a steady-state diffusion flame. Data was recorded from all gauges until a visual steady state was reached. Each experiment was recorded using a RGB video camera so that flame behavior could be correlated with measured parameters. Three repetitions were performed for each test configuration.

The diffusion flame was unstable at times, with the flame occasionally leaning off the centerline. This occurred even with the metal screen around the burner setup. This flame behavior could be attributed to air drafts, thermal gradients in the test room causing natural convection currents, and ambient air entrained horizontally near the burner surface due to the presence of the floor. This behavior was also noticed by You and Faeth [19-22]. If the flame severely swayed in these tests, the test was repeated and the data from that test was not used.

3.4. Results

Data is presented on the heat fluxes measured at the ceiling for the various fire sizes and ceiling heights listed in Table 3.2. Separation of the irradiation and convection in the mixed-mode fire environment requires the determination of the convective heat transfer coefficient, h. Four methods for determining h are provided. A statistical analysis was performed to determine if HRR or ceiling height had a significant effect on the calculated h values. The convection and irradiation components were separated using the experimentally determined coefficients of convective heat transfer. All results shown are taken from the first repetition out of the three for each experimental configuration.

3.4.1. Heat Fluxes and Temperatures

Figure 3.4 contains plots of the heat fluxes and temperatures of both the non-cooled and air-cooled gauges for the 90 kW, L_f/H=1.5 test condition. All three repetitions are shown to

show the variability between repetitions. The non-cooled gauge results show good repeatability. This low variation was consistent among the experimental configurations, with a few deviations at some instances in time. The measured heat fluxes and temperatures from the air-cooled gauge vary considerably more between repetitions than the non-cooled gauge. This is believed to be caused by inconsistencies in the air-cooling supplied from the compressed air-line. Also note the severe drop in heat flux for the air-cooled gauge. Traditional water-cooled gauges, such as the Gardon gauge, maintain a constant surface temperature throughout the exposure and therefore have a constant heat flux. The air for the air-cooled gauge does not provide sufficient cooling in order to keep the gauge temperature and heat flux constant. The temperature rise above ambient for the three repetitions of the air-cooled gauge ranged from 150 to 350K. The losses from the gauge are significant at these high temperatures, and the heat flux decreases significantly. As a result, the air-cooled gauge does not provide a true, standard state heat flux. It is important to note that the fluctuations in the measured heat fluxes are attributed to the puffing and turbulent nature of the flame rather than random noise in the signal. The puffing of the flame occurs at a frequency of roughly 3 Hz as discussed in Appendix F.

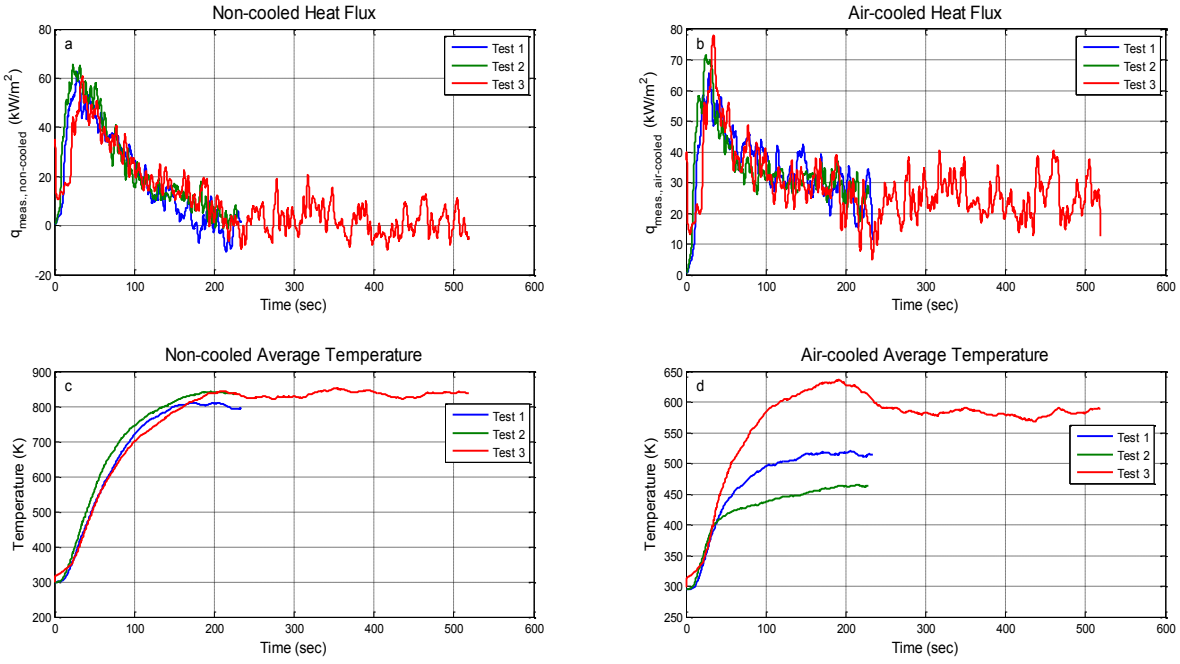

Figure 3.4: Raw Heat Fluxes and Temperatures for 90 kW, L_f/H=1.5 test condition, a) Measured Non-cooled heat flux, b) Measured Air-cooled Heat Flux, c) Non-cooled Temperatures, d) Air-cooled Temperatures.

Figure 3.5 contains the measured gas temperatures for the 90 kW *HRR* at L_f/H=1.5. The gas temperatures had more fluctuations in them than the gauge surface temperatures. Gas temperatures measured near the velocity probe were used in the calculation of the fire plume velocity. These gas temperatures had significantly more fluctuations within each test in comparison to the gas temperatures measured near the ceiling. As discussed earlier, the aspirated thermocouple located near the velocity probe was placed slightly off the centerline of the flame, i.e. the wings of the flame, and therefore was in a location where the flame intermittency was higher. The first repetition of each experimental configuration will be shown for the remainder of the results.

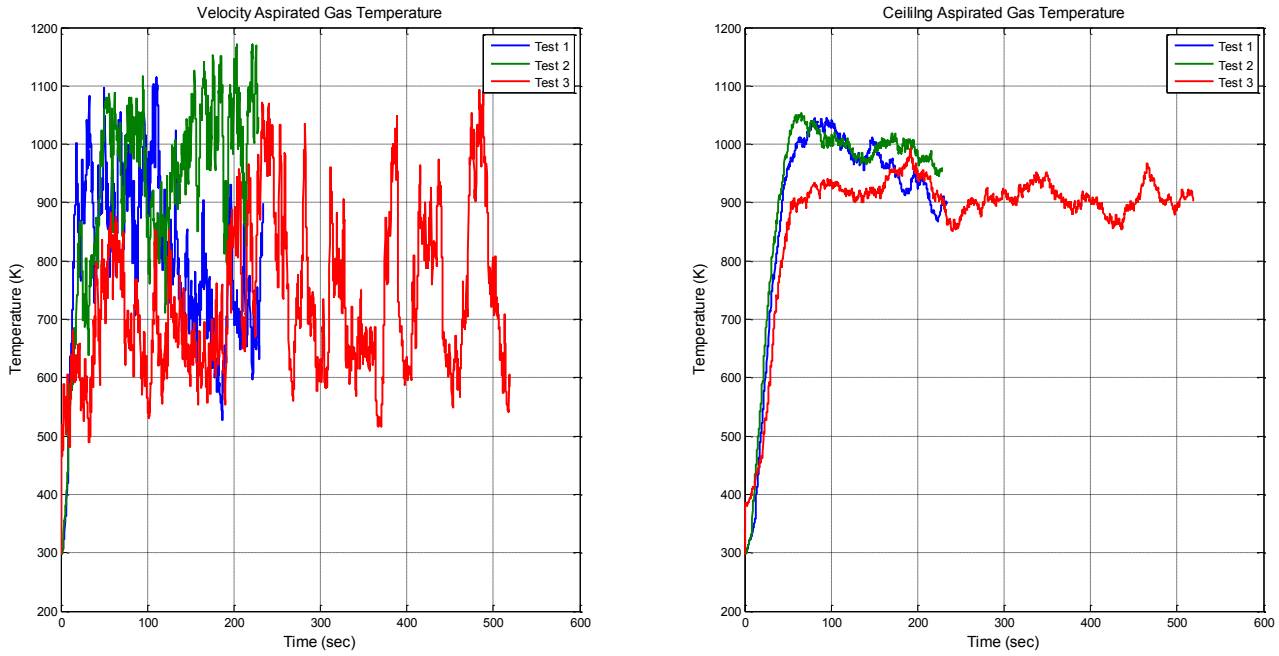

Figure 3.5: Gas Temperatures for 90 kW, L_f/H=1.5 test condition, a) Near velocity probe, b) Near ceiling.

Figure 3.6 contains plots of the heat flux and gauge surface temperatures for each experimental configuration. Results were plotted to highlight the effects that *HRR* and ceiling height have on the ceiling heat fluxes and temperatures at the stagnation point. Non-cooled (solid lines) and air-cooled (dashed lines) data were plotted on the same graphs to provide for easy comparisons between the gauges. It took longer for the higher ceiling heights to reach visual steady values; therefore, their test times are longer.

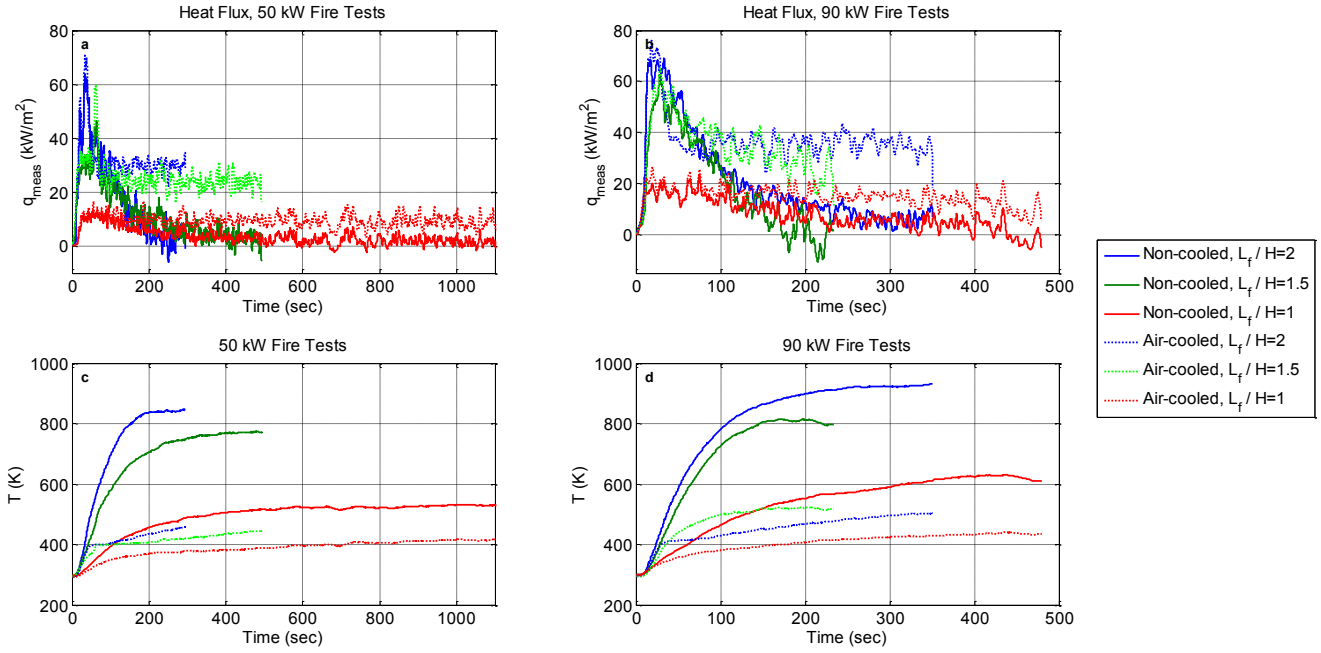

Figure 3.6: Heat Flux and Temperatures at Ceiling Stagnation Point: a) 50 kW Heat Fluxes, b) 90 kW Heat Fluxes, c) 50 kW Gauge Surface Temperatures, d) 90 kW Gauge Surface Temperatures.

The trends in the heat fluxes and temperatures provide insight into the physical occurrences within the fire. When the fire is first initiated, the gauge surface temperatures begin to rise and the heat fluxes increase sharply to a maximum value. From Equation (2), as the gauge surface temperatures increase and approach the surrounding gas temperature, the amount of convection to the gauge surfaces decreases and the amount of reradiation from the gauge surfaces increases. Thus, the measured net heat flux to the surface decreases with increasing exposure time. Eventually, the gauge temperatures and heat fluxes reach a steady state. The non-cooled gauge reaches steady-state values of approximately 4-5 kW/m^2. The air-cooled gauges have higher steady-state values since they are actively cooled with air, thereby maintaining lower surface temperatures and losses. The stagnation point non-cooled heat fluxes and temperatures decrease with increasing ceiling height; with the steepest decrease between the L_f/H=2 and L_f/H=1 ceiling heights. The maximum L_f/H=2 heat fluxes are approximately 50 kW/m^2 higher than the maximum L_f/H=1 heat fluxes for both *HRR*s, with temperature differences of 320 K for both *HRR*s. The difference between the maximum heat fluxes for the L_f/H=2 and L_f/H=1.5 cases is smaller, at approximately 10-15 kW/m^2, with temperature differences between 80-130 K . Both heat flux and temperature increase slightly with increasing

fire size. The L_f/H=2 ceiling height has the highest heat flux with maximum values of 60 and 70 kW/m^2 for the 50 kW and 90 kW *HRR*s, respectively. The difference between the maximum heat fluxes for the L_f/H=1.5 and L_f/H=1 ceiling heights is approximately 15 and 5 kW/m^2, for the 50 kW and 90 kW *HRR*s respectively.

Figure 3.7 contains plots of the gas temperatures at the ceiling for the six test conditions. The gas temperatures have similar trends with *HRR* and ceiling height as the heat flux gauge surface temperatures. The gas temperatures approach a constant value fairly early on in the test and remain steady throughout the exposure. The 90 kW, L_f/H=1.5 case displays some unsteadiness, which was attributed to swaying of the flame.

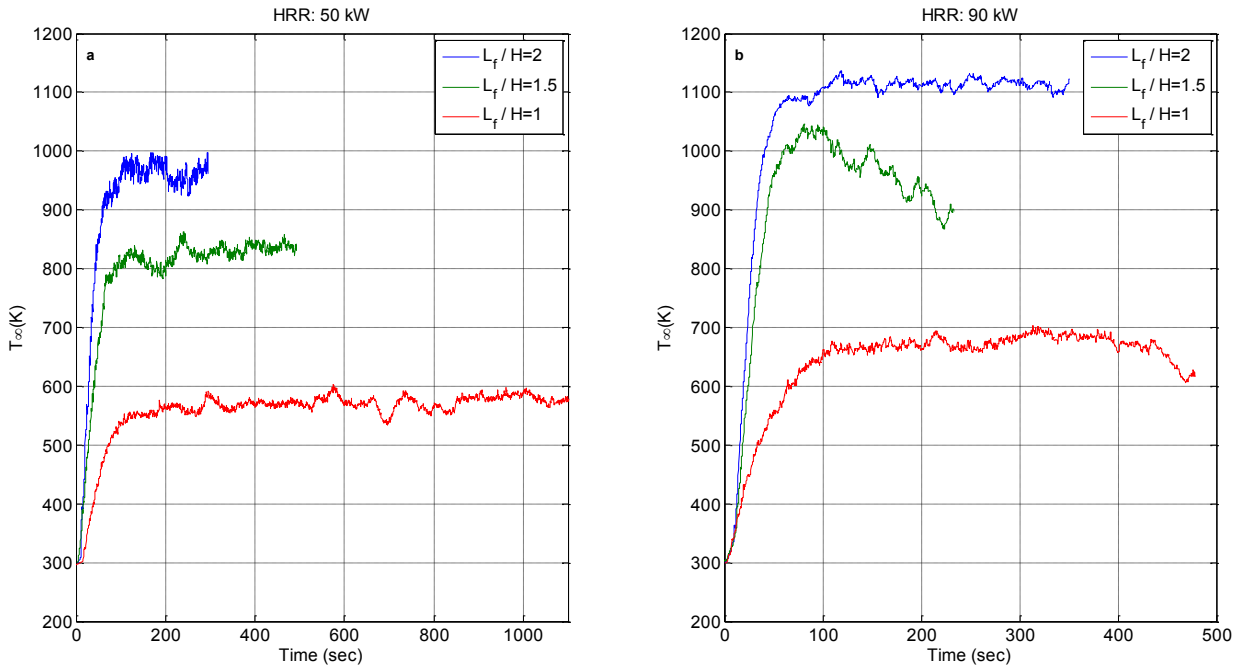

Figure 3.7: Gas Temperatures: a) 50kW *HRR*, b) 90 kW *HRR*

3.4.2. Convective Heat Transfer Coefficient

Four data processing methods were used to calculate the coefficient of convective heat transfer for separation of the radiative and convective components of heat flux. The first two methods require the use of a reference measurement which must be at a different surface temperature than the measurement it is compared to. The second two methods only require the use of one heat flux measurement in conjunction with the surface and gas temperatures. A one way analysis of variance (ANOVA) was performed on the average *h* values summarized in Table 3.3, with a Type I error rate of 0.05; allowing inferences to be made with 95% confidence.

Ceiling height and *HRR* were treated as ordinal variables. The ANOVA was performed to look at the main effects of *HRR* and ceiling height.

3.4.2.1. Reference Method 1, Two Gauges

Reference method 1 is an adaptation of the reference method developed and implemented in Refs. [6-8]. It follows the concepts given in Equations (1-3); requiring the use of two heat flux gauges at different surface temperatures. Assuming that the amount of irradiation to the two gauges, the gas temperature, and the ε_s $\varepsilon_s$and *h* are the same for both surfaces, Equation (3) can be rearranged to solve for *h*.

$$h = \frac{\left(q_{meas,air-cooled} - q_{meas,non-cooled}\right) - \varepsilon_s \sigma\left(T_s^4 - T_{ref}^4\right)}{\left(T_s - T_{ref}\right)} \tag{8}$$

In this research, the air-cooled gauge acted as the reference measurement and is shown as $q_{meas,air\text{-}cooled}$ in Equation (8). The other heat flux and elevated surface temperature were measured using the non-cooled hybrid gauge and are referred to as $q_{meas,non\text{-}cooled}$ and T_s, respectively. The measurements from each gauge were used to calculate *h* at each point in time, thereby providing a transient *h* value. Figure 3.8 contains the results from this method for all experimental configurations. The initial *h* values are unstable and have high uncertainties [8]. This is due to the temperature difference between the two gauges being small at early test times, prior to the non-cooled gauge heating up. These initial *h* values are not considered in the analysis. Averages were taken once T_s became sufficiently larger than T_{ref} and *h* stabilized. Average *h* values from the reference method 1 are summarized in Table 3.3. The reference method 1 for the 90 kW, L_f/H=2 test condition produced a negative *h* value very close to zero. This also occurred for the 50 kW, L_f/H=2 test condition in another repetition. This behavior is caused by a small difference in the gauge heat fluxes and a large temperature difference between the two gauge conditions. This did not occur for each repetition; however, the *h* values for other tests were also generally close to zero. An *h* value this small indicates that the heat transfer is dominated by radiation with a minimal amount of convection.

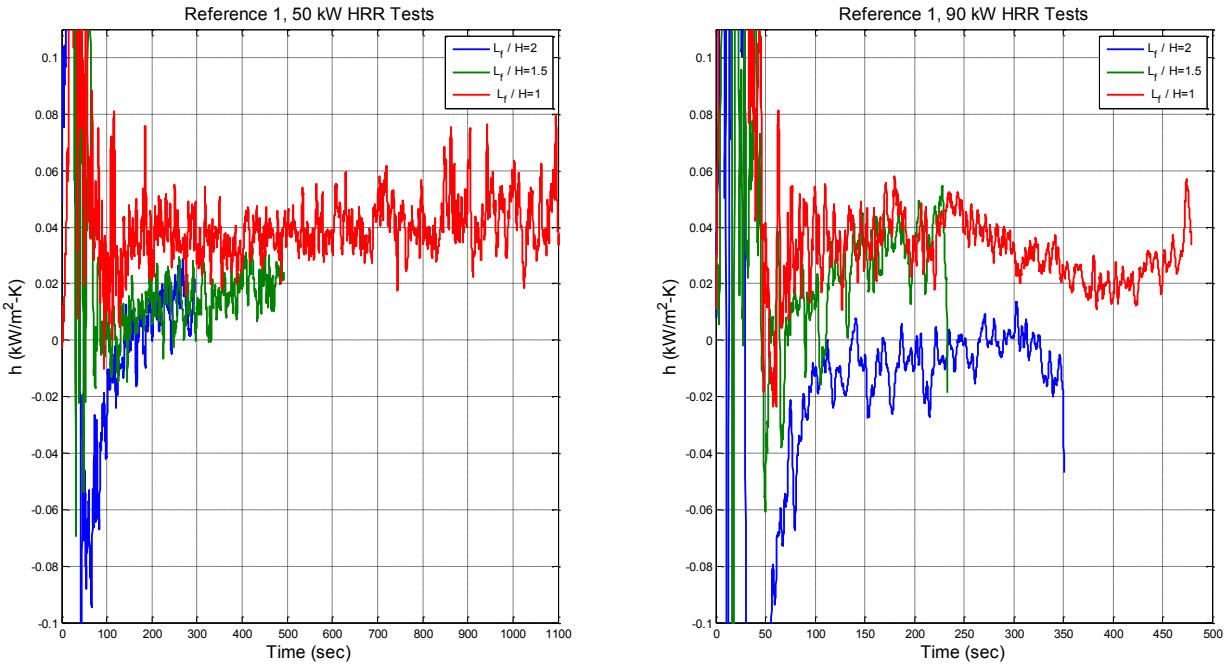

Figure 3.8: Reference Method 1 *h* Values: a) 50 kW *HRR*, b) 90 kW *HRR*

Figure 3.8 does not provide any clear trends in the reference method 1 *h* values due to *HRR* or ceiling height. All repetitions must be considered in determining the effect that these parameters have on the *h* values obtained with the reference method 1. Therefore, the average *h* values taken from all three repetitions are shown in Figure 3.9. The overall average taken using all three repetitions is also shown for each test condition. The *h* values obtained with the reference method 1 increased in a linear fashion with ceiling height for both 50 kW and 90 kW *HRR*s. For the 50 kW *HRR*, the *h* value from the L_f/H=2 ceiling height was significantly different from the *h* values at the other ceiling heights. The L_f/H=1.5 ceiling height had an overall average *h* 6.26 times higher than the L_f/H=2 case, while the L_f/H=1 ceiling height *h* value was 1.44 times higher than the L_f/H=1.5 ceiling height. For the 90 kW *HRR*, the L_f/H=1.5 ceiling height had an overall average *h* 2.03 times higher than the L_f/H=2 case, with the L_f/H=1 ceiling height *h* value also being 2.03 times higher than the L_f/H=1.5 ceiling height. This method produced *h* values which were insensitive to *HRR*, with the *h* values for each *HRR* being within each other's experimental uncertainty. These values are summarized in Table 3.

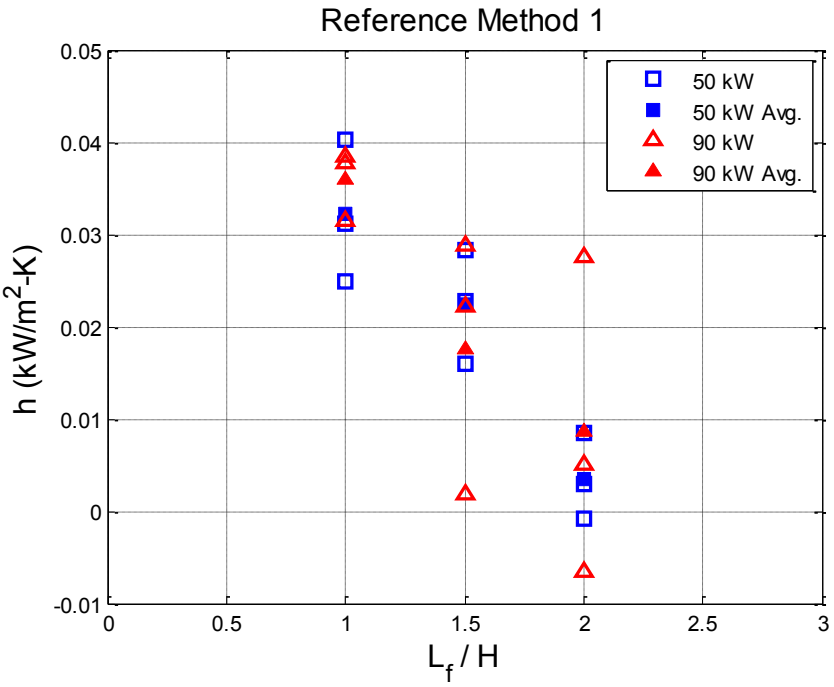

Figure 3.9: Reference Method 1 Average *h* Values

3.4.2.2. Reference Method 2, One Gauge

The second method used to calculate *h* was derived from the same methodology as the first reference method. The unpredictable and puffing nature of diffusion flames, along with soot formation on the gauge surfaces made it difficult to guarantee that the assumptions required for the reference method 1 were met when using two heat flux gauges in the fire. Therefore, a reference method using only one heat flux gauge was developed in this research. In order for the reference method 1 to work, the reference measurement must be at a different surface temperature than the elevated surface temperature, T_s. For this reason, reference method 1 was adapted so that the non-cooled gauge measurements could be used as a reference for itself. A previous point in time from the non-cooled gauge exposure is used as a reference for the entire exposure measured by the non-cooled gauge.

$$h = \frac{\left(q_{meas.,non-cooled} - q_{meas.,non-cooled,previous}\right) - \varepsilon_s \sigma\left(T_s^4 - T_{s,previous}^4\right)}{\left(T_s - T_{s,previous}\right)} \tag{9}$$

This method provides a transient *h* value for each selected reference point, just as in the reference method 1. Since this method requires the use of a previous measurement in time, the assumption must be made that *h* is the same across the entire exposure. Ref. [8] determined that

larger temperature differences resulted in lower uncertainties in *h* for the reference method; therefore, the transient *h* values from the reference method 2 are averaged once the temperature difference between the reference and actual surface temperature becomes sufficiently large. This ΔT is chosen based off of the ΔT required by reference method 1 to provide a stabilized *h* value. An average *h* is produced for each reference point. These averages are shown for the 90 kW *HRR*, L_f/H=1.5 test condition in Figure 3.10. An overall average is taken from all of the values in Figure 3.10 to provide one *h* value per repetition.

Initial values for each test repetition are not shown, nor are included in the averaging. Values at these times were negative, as they corresponded to the ramp up of the measured heat flux. Reference heat flux values taken during this initial ramp up time were smaller than the heat flux for the overall exposure time and therefore, negative *h* values were produced. This method differs from the reference method 1, in that early test times represent larger temperature differences. Therefore, later test times are also not included, since the temperature differences between the reference and the exposure will be small and the calculated *h* value will become unrealistically large.

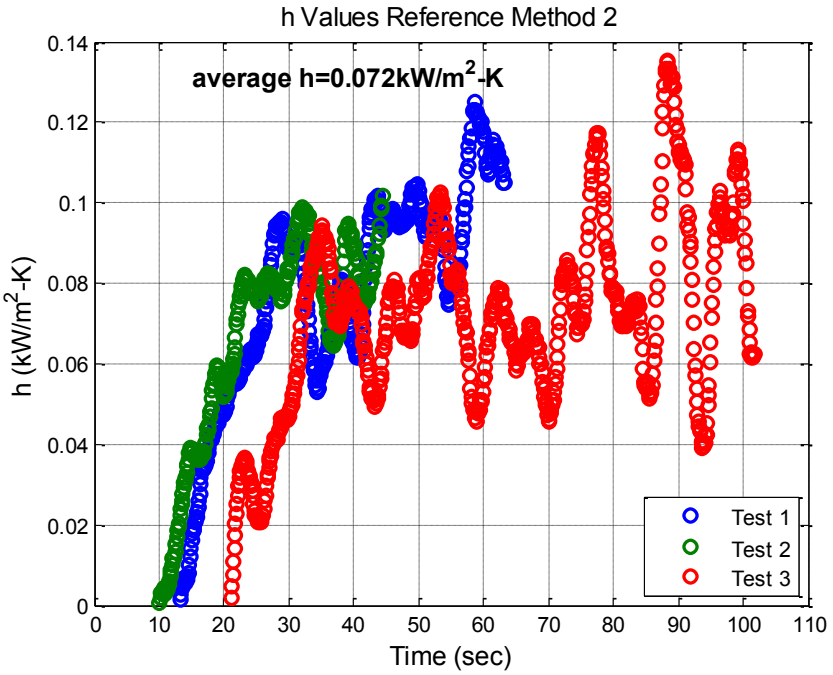

Figure 3.10: Reference Method 2 *h* Values: 90 kW *HRR*, L_f/H=1.5

The average *h* values taken from all three repetitions are shown in Figure 3.11. The overall average taken using all three repetitions is also shown for each experimental

configuration. The *h* values obtained with the reference method 2 had no strong general trends with ceiling height for either the 50 kW or 90 kW *HRR*s. The 50 kW *HRR h* values decreased by a factor of 0.8-0.9 with an increase in ceiling height, opposite the trend in the reference method 1. For the 90 kW *HRR*, the L_f/H=1.5 ceiling height had the highest overall average *h* with a value 1.23 times higher than the L_f/H=2 case. The L_f/H=1 ceiling height *h* value was 0.66 times the L_f/H=1.5 ceiling height. For the levels investigated in this research, there is a slight increase in the *h* values produced with this method with an increase in *HRR* for the L_f/H=1.5 case; where the 90 kW *HRR* has an *h* 1.77 times higher than the 50 kW *HRR h*. For the other two ceiling heights, the 90 kW *HRR* produces *h* values approximately 1.27 times higher than the 50 kW *HRR*; however, these values are within the experimental uncertainties of the data. These values are summarized in Table 3.

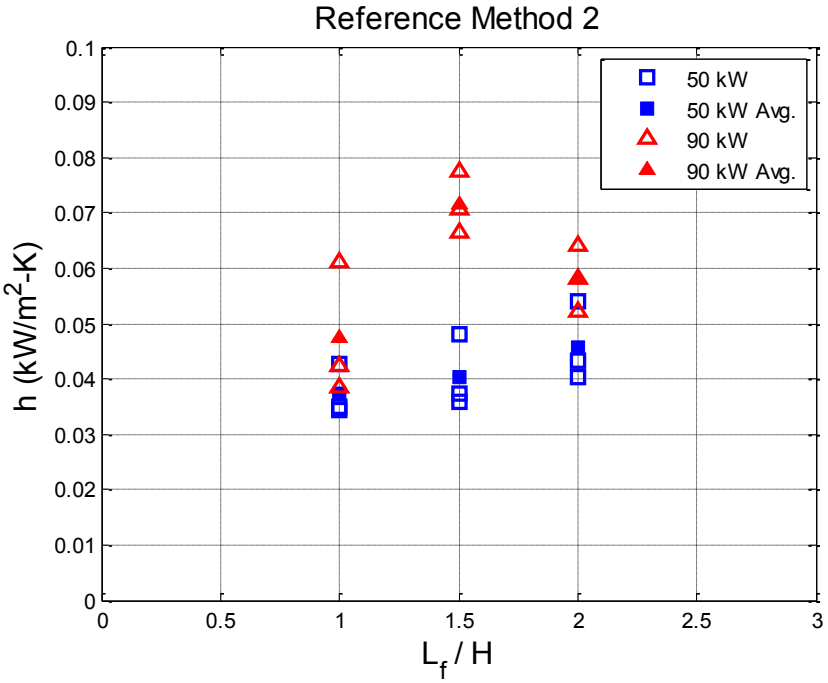

Figure 3.11: Average *h* Values for Reference Method 2

3.4.2.3. Slope Method 1, One Gauge

The third method used to calculate *h* was developed in Refs. [6-8] and employs the use of the absorbed exposure heat flux to the gauge surface which is defined as the amount of absorbed irradiation plus convection.

$$q_{\exp} = \varepsilon_S q_{irr} + h\left(T_\infty - T_S\right) \tag{10}$$

Taking the derivative of the exposure heat flux with respect to T_s, assuming the irradiation and gas temperature are constant, results in,

$$\frac{dq_{\exp}}{dT_S} = -h \tag{11}$$

Therefore, plotting $q''_{\exp}$ against T_s results in a negative slope which is equal to the convective heat transfer coefficient. This method requires the use of one heat flux gauge at elevated surface temperatures. Therefore the non-cooled gauge is used in the calculations. Since the method requires taking the derivative with respect to T_s, the slope method 1 can only be used with transient temperature measurements. Using Equations (2) and (10), the exposure heat flux can also be defined as,

$$q_{\exp} = q_{meas,non-cooled} + \varepsilon_S \sigma T_S^4 \tag{12}$$

Figure 3.12 shows the result of plotting the exposure heat flux calculated using Equation (12) versus the non-cooled gauge surface temperature for the 90 kW *HRR*, L_f/H=1.5 experimental configuration. To satisfy the assumptions, data was only used once the gas temperatures were constant and before the gauge surface temperatures reached a steady state. As a result, data during initial and late test times were not included in the calculation. This method contains a lot of variation about the linear trend. This variation comes from the heat flux measurement, which is actual physical fluctuation occurring as a result of the puffing nature of the flame. This causes the slope method 1 to have slightly more variability between repetitions.

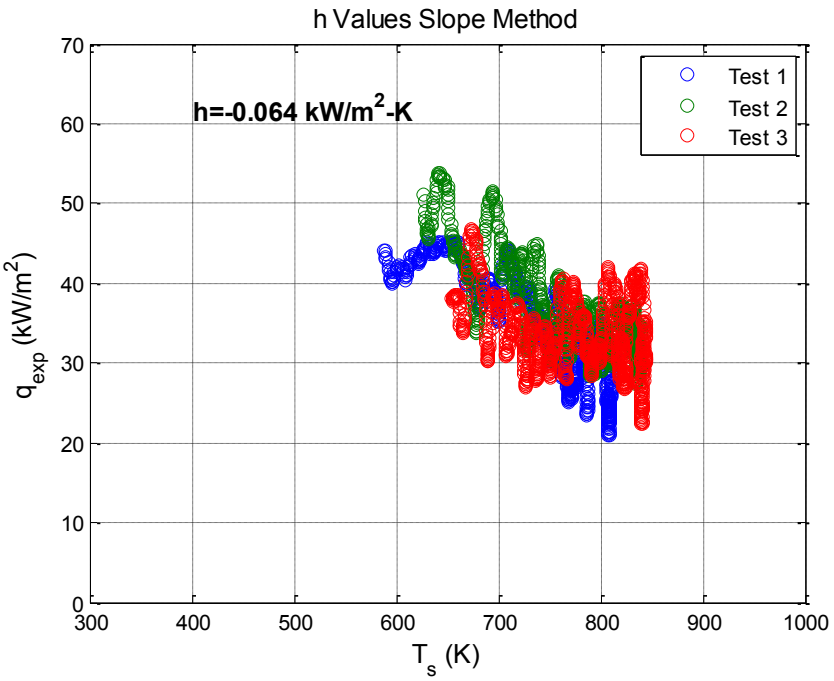

Figure 3.12: Slope Method 1 *h* Values: 90 kW, L_f/H=1.5

Figure 3.13 contains the *h* values of all three repetitions using the slope method 1. The overall average of all three repetitions is also shown for each experimental configuration. For the 50 kW *HRR*, as ceiling height increased, the overall average *h* values decreased in a linear fashion by a factor of 0.55-0.65. The L_f/H=2 ceiling height *h* was significantly different than the L_f/H=1 ceiling height *h*. For the 90 kW *HRR*, the L_f/H=1.5 ceiling height had an overall average *h* 1.13 times higher than the L_f/H=2 case, while the L_f/H=1 ceiling height *h* value was 0.58 times the L_f/H=1.5 ceiling height. For the levels investigated in this research, there is a slight increase in the *h* values produced with this method with an increase in *HRR*, particularly for the L_f/H=1 case, where the 90 kW *HRR* has an overall average *h* 1.9 times higher than the 50 kW *HRR* average *h*. For the L_f/H=2, L_f/H=1.5 ceiling heights, the 90 kW *HRR* produces *h* values approximately 1.8 and 1.03 times higher than the 50 kW *HRR*, respectively. These values are summarized in Table 3.

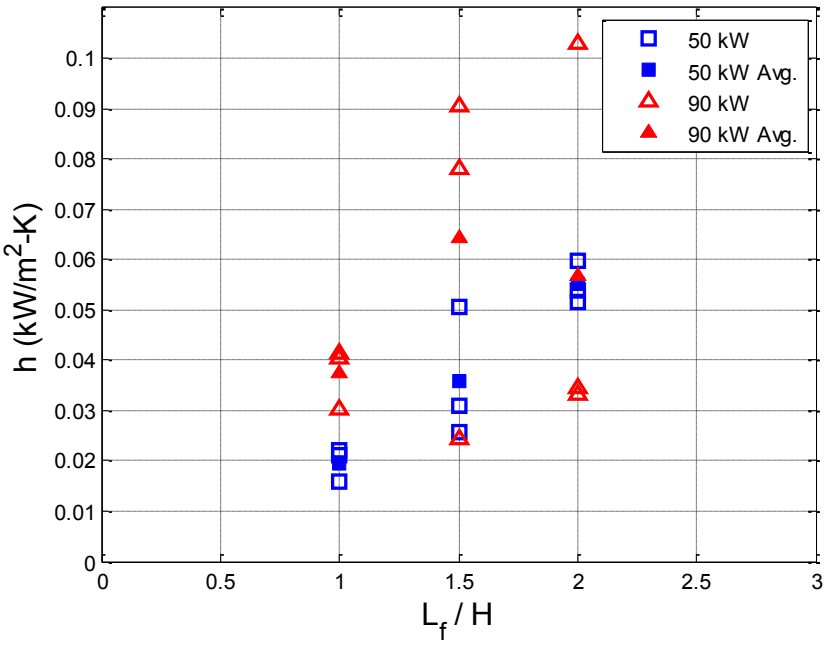

Figure 3.13: Average *h* Values for Reference Method 2

3.4.2.4. Slope Method 2, One Gauge

The slope method 2 is an adaptation of the slope method 1 to include the gas temperature measurement. The non-cooled gauge temperature and gas temperature at the ceiling are required measurements for this method. From Equation (10), rather than taking the derivative with respect to the gauge surface temperature, the derivative is taken with respect to the difference between the gas and the surface temperatures, assuming the irradiation is constant.

$$\frac{dq_{\exp}}{d(T_\infty - T_S)} = h \tag{13}$$

The use of gas temperature measurements is often associated with large errors when used in fire testing; however for this work, the gas temperature had the same fluctuations as the measured non-cooled heat flux. This aided in reducing some of the fluctuations found in the exposure heat flux, thus producing a more clear linear trend between exposure heat flux and gauge surface temperature. The results of the slope method 2 applied to the 90 kW, L_f/H=1.5 experimental configuration are shown in Figure 3.14. This method produces results which are opposite in appearance of the slope method 1. Smaller temperature differences (values near the origin) correspond to late test times and larger temperature differences between the gas and gauge surface correspond to early test times. Data was only used once the gas temperatures were

constant and before the gauge surface temperatures reached a steady state to remain consistent with the values obtained with the slope method 1. It is important to note that this method does not require a constant gas temperature.

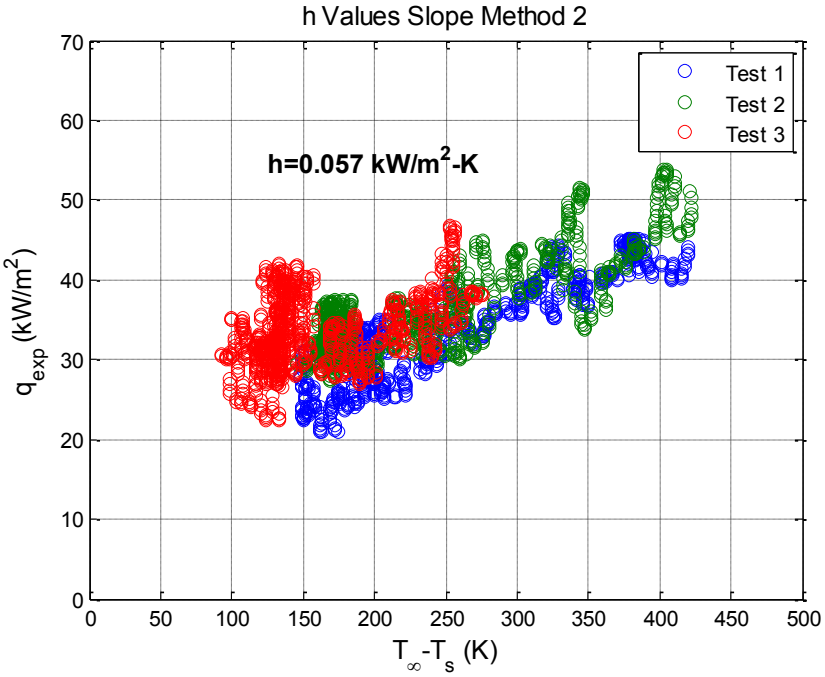

Figure 3.14: Slope Method 2 *h* Values: 90 kW, L_f/H=1.5

Figure 3.15 contains the *h* values of all three repetitions using the slope method 2. The overall average of all three repetitions is also shown for each experimental configuration. The *h* values obtained through the slope method 2 have no trends with ceiling height for either the 50 kW or 90 kW *HRR*. In addition, there is no clear trend with *HRR*, except for the L_f/H=1.5 ceiling height in which the 90 kW *h* is 1.6 times the 50 kW *h* value. These values are summarized in Table 3.

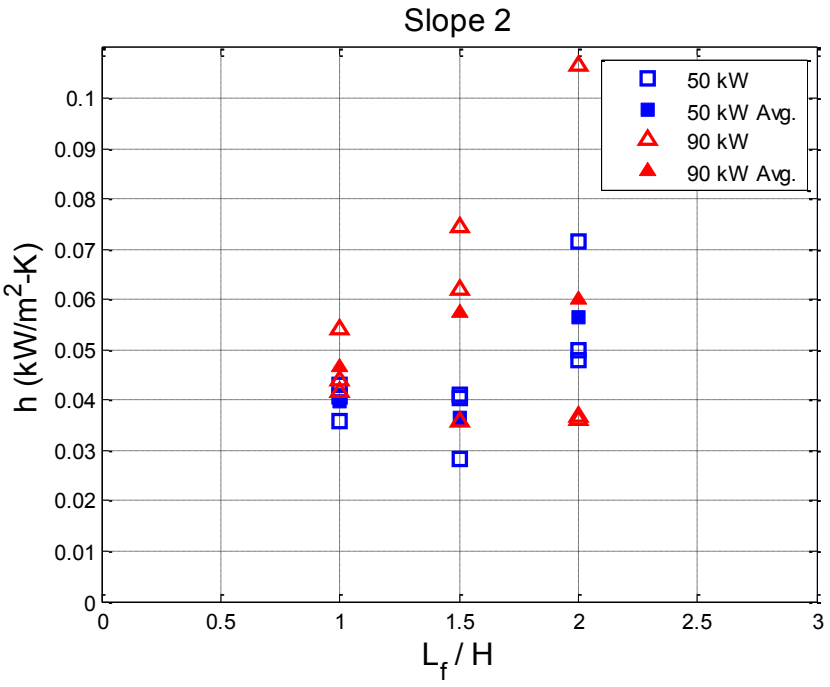

Figure 3.15: Average *h* Values Slope Method 2: 90kW, L_f/H=1.5

3.4.2.5. Summary of h Values and Effects of HRR and Ceiling Height

Table 3.3 summarizes the average *h* values obtained with the four methods discussed above. Figure 3.16 contains plots of all average *h* values for all four methods used to calculate *h*.

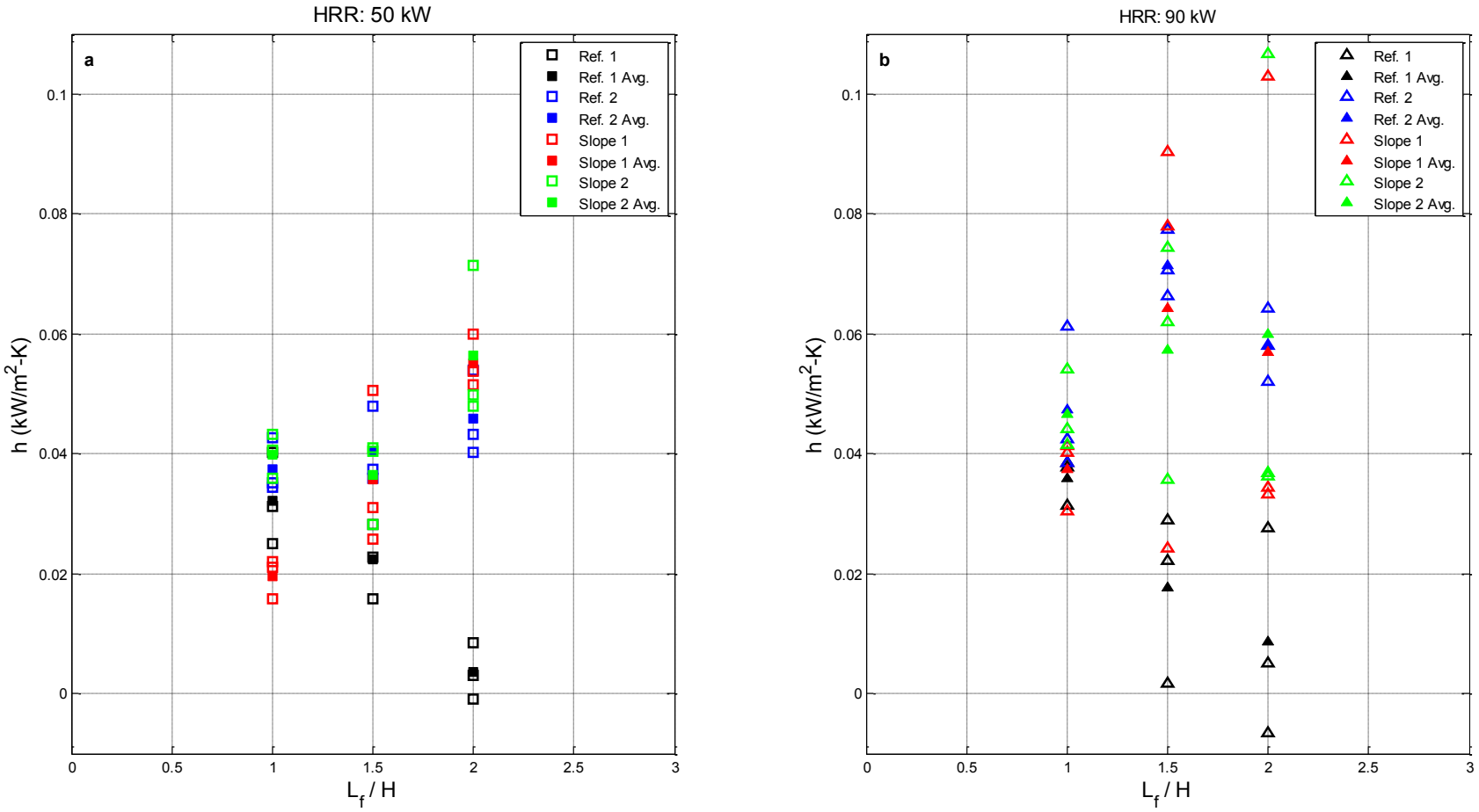

Figure 3.16: Summary of Average *h* Values for all Methods of Calculating *h*, a) 50 kW, b) 90 kW

In summary, for the 50 kW *HRR*, the average *h* determined with the reference method 1 for the L_f/H=2 ceiling height is significantly different from the other ceiling heights. *HRR* did not cause significant differences in the calculated *h* values obtained with the reference method 1 at any ceiling height. The reference method 2 *h* values the L_f/H=1 ceiling height was significantly different than the others for the 90 kW *HRR*. At the L_f/H=1.5 ceiling height, *HRR* had a significant effect on the calculated *h* values, with the 90 kW *HRR h* being 1.77 times higher than the 50 kW *HRR*. For the slope method 1, at *HRR* of 50 kW, the L_f/H=2 and L_f/H=1 ceiling height average *h* values were significantly different. Also, *HRR* was detected to have a significant effect on *h* at a ceiling height of L_f/H=1. The slope method 2 *h* values were not significantly different for either *HRR* or ceiling height.

The ANOVA results make more sense when looking at the variability within each experimental configuration in comparison to the variability between experimental configurations. If no significant differences were detected for a specific comparison, it means that the variability within each experimental configuration was greater than the variability between experimental configurations. For example, for the reference method 1, significant differences were detected between the average *h* values for the 50 kW *HRR* at the L_f/H=1 and L_f/H=2 ceiling heights; however, no significant differences were detected between the average *h* values for the 90 kW *HRR* at any ceiling heights. This was because the variability in the average *h* values for the 90 kW *HRR* ceiling heights encompassed each other, or in other words the results were within the experimental uncertainty. This is reflected in Figure 3.16.

The average *h* values from the methods using only the non-cooled gauge generally correspond well with each other, however, the average *h* values from the reference method 1 which uses two heat flux gauges, are far different from the others. Its average *h* values are often several times smaller than those calculated using one heat flux gauge. Its trends with ceiling height are opposite of the non-cooled gauge methods. The lack of agreement between the methods is the greatest at the lowest ceiling heights, with the *h* values calculated using the non-cooled heat flux gauge data being up to 15.8 times larger than the *h* calculated with the reference method 1. Such large disagreements between the methods using only one gauge, and the reference method 1 raises concern. It is assumed that *h* is the same for both heat flux gauges, and therefore there should not be any major disagreements between the methods. The coefficient of convective heat transfer is only dependent on the properties of the fluid surrounding the

gauge. These properties may change with the gas temperature; therefore, once the gas temperature becomes constant, h should also be relatively constant for the remainder of the exposure. It should be noted that at the L_f/H=1 ceiling heights, the methods tend to agree with each other more closely across all methods. These issues will be addressed in the discussion section of the paper.

Table 3.3: Summary of *h*

For Relative Ceiling Height of L_f/H=2

	50 kW				90 kW			
Test #	**Reference Method 1 (kW/m²K)**	**Reference Method 2 (kW/m²K)**	**Slope Method 1 (kW/m²K)**	**Slope Method 2 (kW/m²K)**	**Reference Method 1 (kW/m²K)**	**Reference Method 2 (kW/m²K)**	**Slope Method 1 (kW/m²K)**	**Slope Method 2 (kW/m²K)**
1	0.0085	0.0540	0.0599	0.0715	-0.0066	0.0521	0.0333	0.0368
2	-0.0008	0.0402	0.0538	0.0498	0.0276	0.0642	0.1030	0.1067
3	0.0030	0.0433	0.0515	0.0480	0.0051	0.0581	0.0344	0.0363
Avg.	**0.0036**	**0.0458**	**0.0551**	**0.0564**	**0.0087**	**0.0581**	**0.0569**	**0.0599**
Std. dev./avg(--)	1.3110	0.1580	0.0788	0.2318	1.9979	0.1041	0.7017	0.6758

For Relative Ceiling Height of L_f/H=1.5

	50 kW				90 kW			
Test #	**Reference Method 1 (kW/m²K)**	**Reference Method 2 (kW/m²K)**	**Slope Method 1 (kW/m²K)**	**Slope Method 2 (kW/m²K)**	**Reference Method 1 (kW/m²K)**	**Reference Method 2 (kW/m²K)**	**Slope Method 1 (kW/m²K)**	**Slope Method 2 (kW/m²K)**
1	0.0159	0.0375	0.0310	0.0410	0.0289	0.0774	0.0904	0.0744
2	0.0228	0.0480	0.0257	0.0282	0.0018	0.0664	0.0780	0.0620
3	0.0283	0.0359	0.0505	0.0405	0.0223	0.0707	0.0243	0.0357
Avg	**0.0223**	**0.0405**	**0.0357**	**0.0366**	**0.0177**	**0.0715**	**0.0642**	**0.0574**
Std. dev./avg(--)	0.2782	0.1624	0.3655	0.1983	0.7999	0.0775	0.5470	0.3445

For Relative Ceiling Height of L_f/H=1

	50 kW				90 kW			
Test #	**Reference Method 1 (kW/m²K)**	**Reference Method 2 (kW/m²K)**	**Slope Method 1 (kW/m²K)**	**Slope Method 2 (kW/m²K)**	**Reference Method 1 (kW/m²K)**	**Reference Method 2 (kW/m²K)**	**Slope Method 1 (kW/m²K)**	**Slope Method 2 (kW/m²K)**
1	0.0403	0.0351	0.0220	0.0359	0.0315	0.0386	0.0304	0.0441
2	0.0312	0.0427	0.0158	0.0432	0.0385	0.0424	0.0403	0.0416
3	0.0250	0.0344	0.0211	0.0406	0.0378	0.0612	0.0413	0.0542
Avg	**0.0322**	**0.0374**	**0.0196**	**0.0399**	**0.0359**	**0.0474**	**0.0373**	**0.0466**
Std. dev./avg(--)	0.2392	0.1231	0.1706	0.0927	0.1073	0.2553	0.1614	0.1431

3.4.3. Velocity, Reynolds and Rayleigh Number

The measured time-averaged velocities were used to determine the flow Reynolds number, *Re*, defined as

$$\mathrm{Re}_D = \frac{\rho V D}{\mu} \tag{14}$$

The diameter of the jet, D, approximated as the length of one side of the burner, was chosen as the characteristic length; treating the diffusion flame as an axisymmetric jet. Gas density, ρ, and dynamic viscosity, μ, were evaluated using the measured gas temperature taken near the bi-directional probe, assuming the gas concentrations could be approximated by air.

The Rayleigh number, *Ra*, was calculated using the fire plume gas temperature measurements taken adjacent to the bi-directional probe. In this research, *Ra* was calculated using the traditional definition of Rayleigh number, defined by temperature differences.

$$Ra_T = \frac{g\beta_{film}}{\nu_{film}\alpha_{film}}\left(T_\infty - T_{amb}\right)D^3 \tag{15}$$

In Equation (15) T_{amb} is the ambient temperature, T_∞ is the measured gas temperature, g is the gravitational constant, β, ν, and α, are the coefficient of thermal expansion, kinematic viscosity, and thermal diffusivity of the gas, respectively. All gas properties were evaluated at the film temperature defined as $T_{film}=(T_\infty+T_{amb})/2$. The diameter of the jet, approximated as the length of one side of the burner, was chosen as the characteristic length to remain consistent with axisymmetric jet theory and the calculated *Re* above. You and Faeth [19-22] also related their measured stagnation point heat fluxes to a Rayleigh number, defined by Equation (16). This version of Rayleigh number was compared to the calculated results using Equation (15).

$$Ra_Q = \frac{g\beta Q H^2}{\rho_{amb} c_p \nu_{amb}^3} \tag{16}$$

The *Re* and *Ra* numbers provide insight into the flow characteristics of the diffusion flame. They are parameters used to describe the forced and natural convection processes present in the flow and are indicative of the amount of heat transferred by convection to the ceiling from the diffusion flame.

The time-averaged *V*, *Re* and *Ra* are shown in Figure 3.17 and are summarized in Table 3.4. For the 50 kW *HRR*, the average V, *Re*, and *Ra* numbers all tend to increase with an increase in ceiling height. The velocity between the lowest and highest ceiling heights are

considerably different with the L_f/H=1 velocity being 1.43 times higher than the L_f/H=2 ceiling height. *HRR* increases the average velocities slightly; however, the difference is not significant. The *Re* number increases significantly with increasing ceiling height for both *HRR*s. More specifically, the L_f/H=1 ceiling height. This is the result of the increasing turbulence with height as more air is entrained into the flame. *HRR* does not cause a significant increase in the *Re* number as expected from the velocity measurements. The *Ra* number calculated using Equation (15) does not change significantly among ceiling heights or *HRR*s. Although it appears that the average values increase slightly with an increase in ceiling height, the variation within each experimental configuration is greater than the variation between experimental configurations. The *Ra* number calculated using the relation in Equation (16) is twice as large as the values calculated with Equation (15).

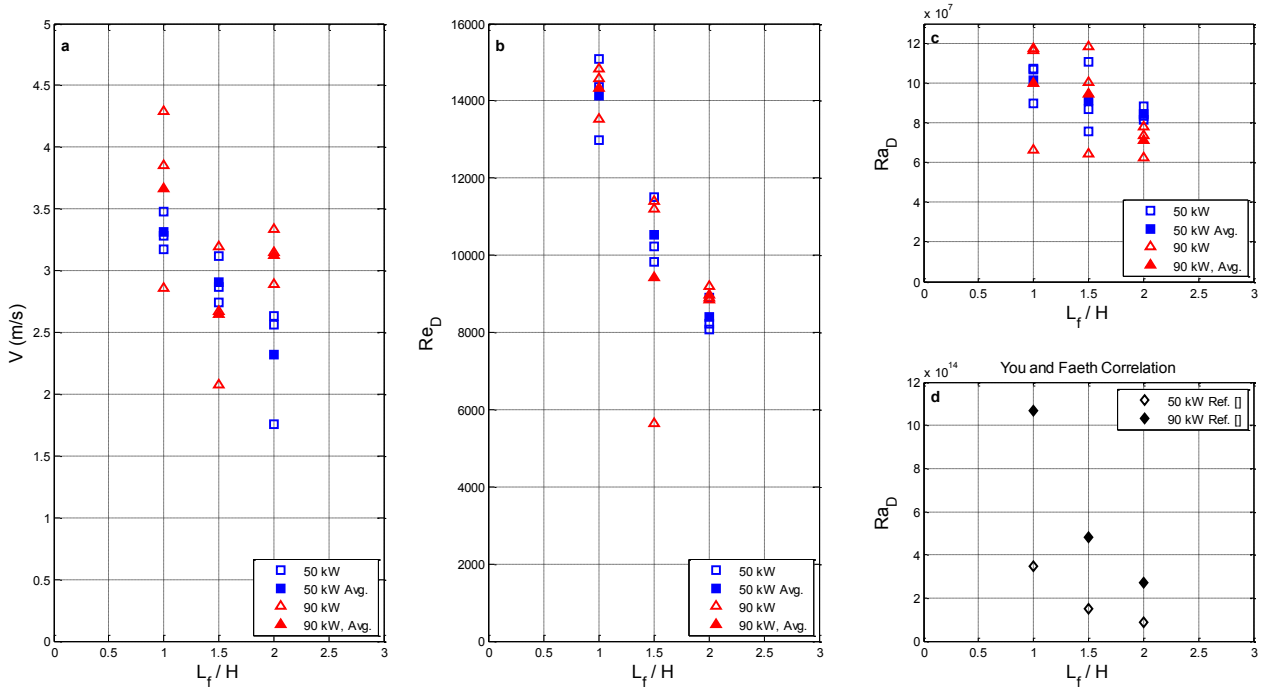

Figure 3.17: Average *V, Re, Ra*: a) *V* , b) *Re* number, c) *Ra* number, Equation (15), d) *Ra* number, Equation (16)

Table 3.4: Summary of Average V, Re (Equation 14), and Ra (Equation 15)

For Relative Ceiling Height of L_f/H=2						
	50 kW			90 kW		
Test #	**V (m/s)**	**Re_D**	**Ra_D**	**V (m/s)**	**Re_D**	**Ra_D**
1	1.76	8.08E+03	8.84E+07	3.34	8.84E+03	6.26E+07
2	2.63	8.23E+03	8.14E+07	2.89	9.21E+03	7.79E+07
3	2.56	8.89E+03	8.37E+07	3.15	8.89E+03	7.40E+07
Avg	**2.32**	**8.40E+03**	**8.45E+07**	**3.13**	**8.98E+03**	**7.15E+07**
std. dev.	0.49	4.31E+02	3.59E+06	0.23	1.98E+02	7.99E+06
For Relative Ceiling Height of L_f/H=1.5						
	50 kW			90 kW		
Test #	**V (m/s)**	**Re_D**	**Ra_D**	**V (m/s)**	**Re_D**	**Ra_D**
1	3.12	9.84E+03	7.59E+07	3.20	1.14E+04	1.18E+08
2	2.74	1.15E+04	8.67E+07	2.67	1.12E+04	1.00E+08
3	2.87	1.02E+04	1.11E+08	2.08	5.66E+03	6.47E+07
Avg	**2.91**	**1.05E+04**	**9.11E+07**	**2.65**	**9.43E+03**	**9.45E+07**
std. dev.	0.19	8.77E+02	1.77E+07	0.56	3.27E+03	2.74E+07
For Relative Ceiling Height of L_f/H=1						
	50 kW			90 kW		
Test #	**V (m/s)**	**Re_D**	**Ra_D**	**V (m/s)**	**Re_D**	**Ra_D**
1	3.28	1.51E+04	1.07E+08	4.29	1.48E+04	6.67E+07
2	3.48	1.30E+04	8.99E+07	3.85	1.35E+04	1.17E+08
3	3.17	1.44E+04	1.07E+08	2.86	1.46E+04	1.18E+08
Avg	**3.31**	**1.41E+04**	**1.01E+08**	**3.67**	**1.43E+04**	**1.00E+08**
std. dev.	0.16	1.07E+03	9.98E+06	0.73	6.86E+02	2.91E+07

3.4.4. Separated Heat Transfer Components

The components of heat transfer from the impinging fire plume to the ceiling were separated using the methodology developed by Vega et al. [6-8]. The amount of convective heat flux was calculated by,

$$q_{conv} = h\left(T_\infty - T_S\right) \tag{17}$$

where the convective heat transfer coefficient was chosen to be the average of the three repetitions for each of the four methods discussed above, T_s is the measured elevated surface temperature of the non-cooled gauge, and T_∞ is the measured gas temperature near the ceiling. From Equation (2), once the convective heat transfer is known, the amount of absorbed irradiation to the ceiling surface can be calculated as,

$$\varepsilon_S q_{irr} = q_{meas,non-cooled} - h\left(T_\infty - T_S\right) + \varepsilon_S \sigma T_S^4 \quad (18)$$

where the emissivity and all of the variables on the right hand side of the equation are known.

Figure 3.18 contains plots of the separated components for all six experimental configurations using data from the first repetition of each. The convection and absorbed irradiation components are shown using all four methods of calculating *h*. All of the methods of calculating *h* using the non-cooled gauge data produced similar levels of convection and irradiation. Therefore, the results can be grouped into values corresponding to the reference method 1 *h* values and values associated with using the reference method 2 and slope methods *h* values. Lower ceiling heights resulted in higher measured heat fluxes as well as higher reradiation heat fluxes. For all tests, reradiation became a significant component of heat transfer once the gauge surface temperature began to increase. It became larger than the measured non-cooled heat flux at approximately 100-200 seconds into the test for all configurations. At the L_f/H=2 ceiling height, the reradiation increased to a value approximately 5-10 times larger in magnitude than the measured heat flux for the 50 kW and 90 kW *HRR*s, by the end of the test. With increasing ceiling height, this difference in magnitude decreased. Just as the surface temperature and measured heat flux increased with *HRR*, so too did the reradiation from the gauge surface.

For both the 50 kW and 90 kW *HRR*s at the L_f/H=2 case, the convection was very close to zero using the reference method 1 *h* value. In the 50 kW fire, the convection decreased from 1 kW/m^2 to 0.2 kW/m^2, while in the 90 kW fire it decreased from 4 to 1.6 kW/m^2. Such low values of convection indicate a radiation dominated environment where the measured non-cooled heat fluxes were almost a direct measurement of the net radiation exchange. The calculated convection using the reference method 1 *h* value contributed approximately 2% and 5% of the total exposure heat flux for the 50 kW and 90 kW *HRR*s, respectively. The convection calculated using the non-cooled gauge *h* values, was much higher, ranging from 20 kW/m^2 early in the test to 6 kW/m^2 by the end of the test for the 50 kW *HRR* and from 30 kW/m^2 to 11 kW/m^2 for the 90 kW *HRR*. This corresponds to a contribution of 50% in the beginning of the tests to 20 and 30% of the total exposure flux at the end of the test, for the 50 kW and 90 kW *HRR*s, respectively. At the L_f/H=1.5 ceiling height, convection contributed approximately 40% of the total exposure heat flux for the 90 kW *HRR* and from 40% at the beginning of the test to

approximately 15% at the end of the test for the 50 kW *HRR* using the non-cooled *h* values. With the reference method 1 *h* values, at the L_f/H=1.5 ceiling height, convection contributed 18% at the beginning to 12% at the end of the test for the 90 kW *HRR* and 20%-9% for the 50 kW *HRR*. For the L_f/H=1 ceiling height, convection started out at approximately 50% and decreased to 20% by the end of the test for both *HRR*s and all *h* values.

The trends in the irradiation component remained relatively the same between methods despite the fact that the convection heat transfer component was greatly affected by the differences in the calculated *h* values. For all methods and experimental configurations, the initial absorbed irradiation is not constant due to the initial ramp up of heat flux and temperature; however, once the gas temperature reached a steady state, the irradiation did as well. The reference method 1 irradiation components were initially equal to the measured non-cooled heat flux due to the convection and reradiation being approximately equal at that time. The irradiation component calculated using the non-cooled gauge methods was initially smaller than the measured non-cooled heat flux. This was a result of the larger convection early in the test. For either *h,* once the reradiation component began to increase and surpassed the convection heat transfer, the irradiation component remained constant at a value larger than the measured non-cooled heat flux. For both *HRR*s and all *h* values, the irradiation decreased with an increase in ceiling height; with a major decrease occurring from the L_f/H=1.5 ceiling heights to the L_f/H=1 ceiling heights. This is expected since the L_f/H=1 ceiling height corresponds to a location right at the flame length where flame intermittency is increased, decreasing the influence of irradiation in this region. Within this region, the absorbed irradiation heat flux approached the value of the reradiation heat flux at the end of the exposure. This indicates that there is little net radiation exchange late in the test and convection becomes equal to the measured heat flux.

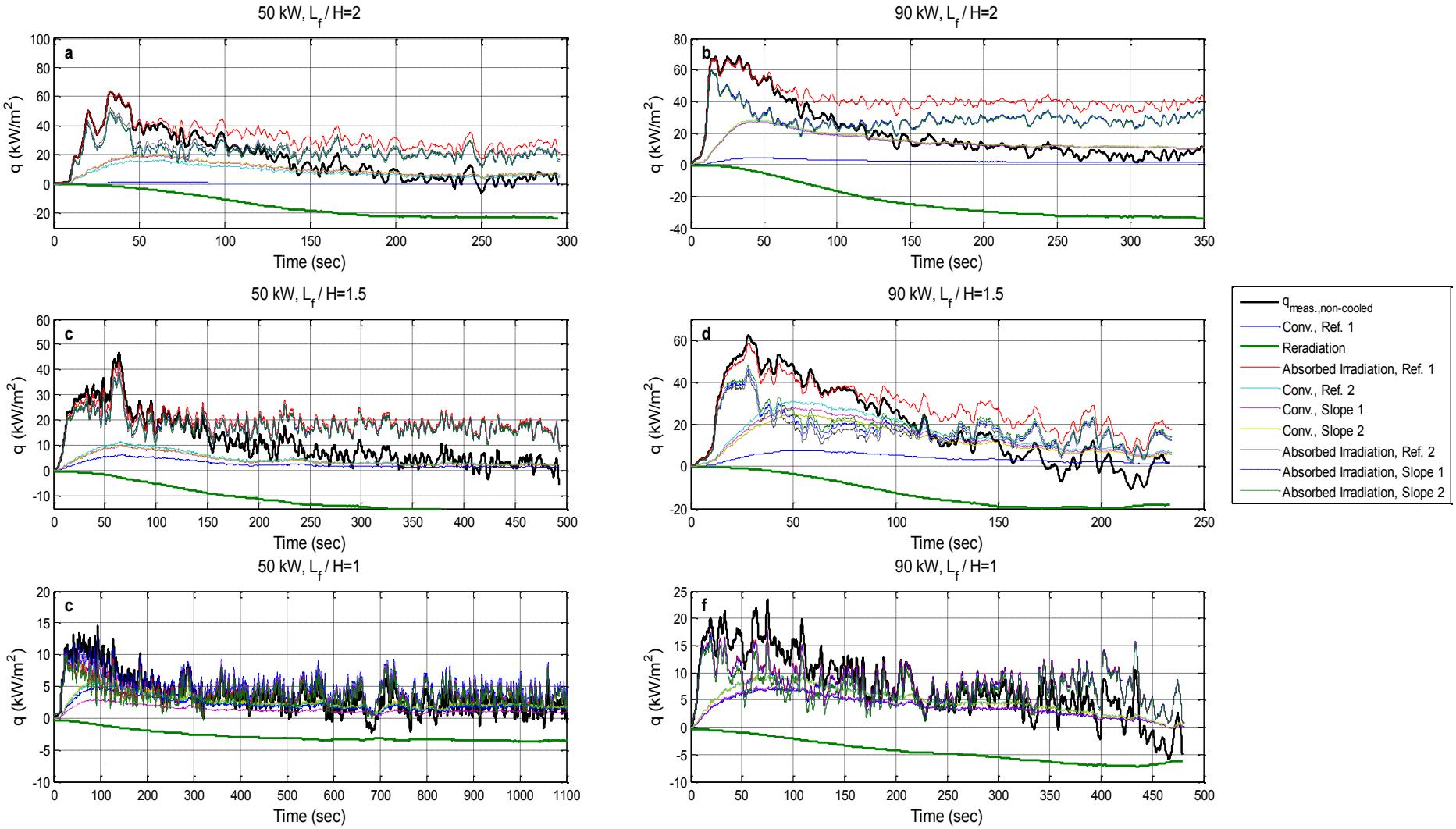

Figure 3.18: Separated Heat Transfer Components: a-b) L_f/H=2, 50 and 90 kW *HRR* respectively, c-d) L_f/H=1.5, 50 and 90 kW *HRR* respectively, e-f) L_f/H=1, 50 and 90 kW *HRR* respectively.

3.5. Discussion

3.5.1. Separated Components of Heat Transfer

The effect that the difference in the *h* values between methods has on the convection components of heat transfer was significant. For the *h* values calculated with the reference method 1, the convection was very near zero in the lower ceiling heights. Given that the velocities and *Re*, *Ra* numbers were not close to zero for these configurations, it is believed that the *h* was underestimated. For the *h* values calculated with the reference method 2, and slope methods, the convection at the end of the exposures approached the same value as the measured non-cooled heat flux, and in some cases, the convection was greater than the measured heat flux as shown in Figure 3.18. If Equation (2) is rearranged as,

$$h\left(T_\infty - T_s\right) - q_{net} = \varepsilon_s \sigma T_s^4 - \varepsilon_s q_{irr} \tag{19}$$

it becomes apparent that the reradiation must have been larger than the absorbed irradiation to the surface for the convection heat transfer to be greater than the measured non-cooled heat transfer. This occurred for both *HRR*s at the L_f/H=2 ceiling height and for the 90 kW case at L_f/H=1.5. The convection calculated using only the data from the non-cooled gauge for these cases was up to two or more times larger than the measured heat flux. This may seem like an odd result; however, only if the assumption is made that the flame acts as a blackbody, making the absorbed irradiation higher than the reradiation. In these experiments, this assumption cannot be made. This is because the irradiation from the fire source is dependent upon the flame emissivity, which in turn is dependent upon the optical thickness of the flames and the soot volume fraction [32]. Measurements were not made to quantify the flame emissivity or temperature and therefore, it cannot be assumed that the source irradiation acts as a blackbody. In fact, the flame emissivity has been measured to be as low as 0.4 [4]. In addition, although the measured heat flux reaches a small steady-state value, the other modes of heat transfer are still present. There will be convection as long as the gauge surface temperatures and the surrounding gas temperatures are different, which is the case in these experiments. Therefore, it is possible for the convection to contribute a non-negligible amount in comparison with the steady-state measured heat flux. Weng and Hasemi [25] also reported similar behavior in their model, where the convection component was up to eight times larger than the net heat flux at the stagnation point. This behavior was attributed to lack of experimental data in the stagnation region; therefore, an accurate distribution could not be obtained [25]. In this research, this only occurred

at the lower ceiling heights. As ceiling height increased, the convection at the end of the exposure was slightly smaller than the measured non-cooled heat flux.

3.5.2. Methods of Calculating h

The behavior of the heat transfer components discussed in Section 3.4.4 could also be attributed to the limitations of the methods used to calculate *h*. As discussed in Section 3.4.2.5, the *h* values calculated with the reference method 2, slope 1 and slope 2 methods were very similar with one another; however the *h* values calculated using the reference method 1 were drastically different, with values up to 15.8 times lower than the other methods. Due to these differences, each method will be analyzed in the following pages to determine if there are any limitations to their assumptions and their use within this fire scenario. Figure 3.19 shows a comparison between the relative variations of the *h* methods for each of the six experimental configurations. These values will be used in the discussions which follow.

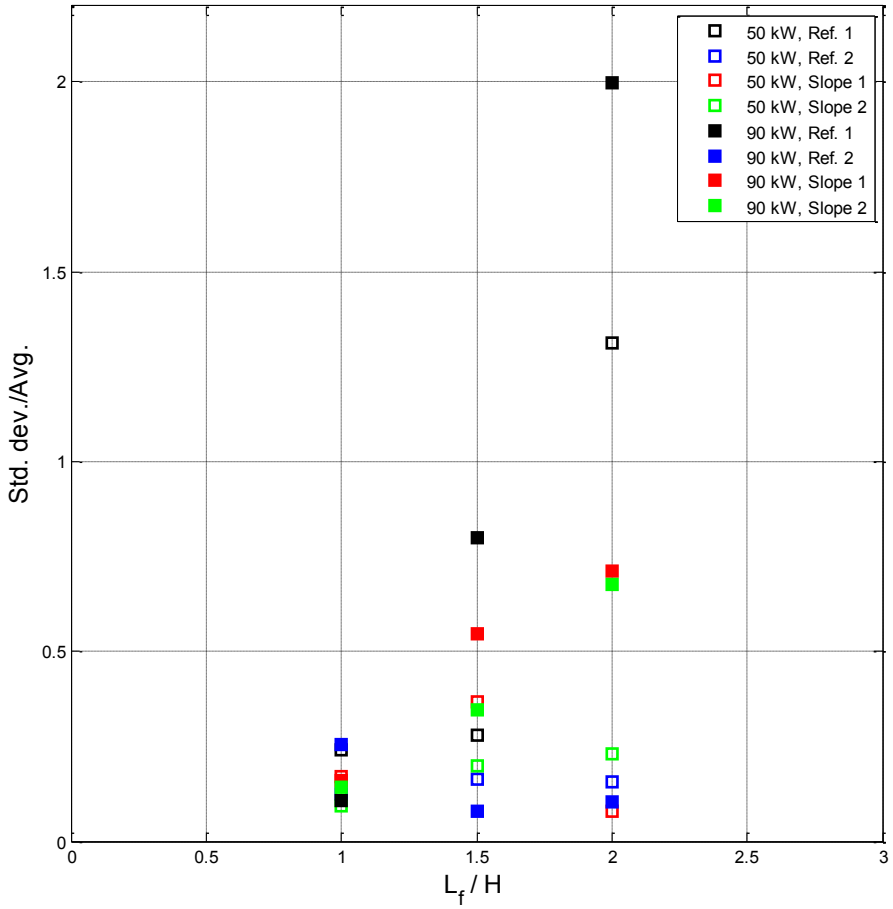

Figure 3.19: Relative Variations in the Calculated *h* Values for all methods and experimental configurations.

The reference methods follow the methodology from Equations (1-3) requiring that the two surfaces are exposed to the same flow conditions, have the same amount of irradiation and have the same emissivity and h across their surfaces. For the reference method 1, these assumptions apply to two hybrid heat flux gauge surfaces. For the reference method 2, the assumptions only apply to one gauge surface; however, since a previous point in time is used as the reference, the flow conditions, irradiation, emissivity and h must be the same across the entire exposure. In a fire scenario, these assumptions are difficult to ensure regardless if they are made between two surfaces or two instances in time. The puffing and swaying nature of the diffusion flame made it difficult to assume that the irradiation was the same across the two gauge surfaces or at different exposure times. Although, the gauges were covered in soot prior to each test, it could not be determined whether further soot collection on the gauge surfaces occurred during the exposure, and if the layers of soot on each gauge were the same for all repetitions and configurations. All of these variables could contribute to the possible violation of the assumptions made for both reference methods.

The relative variation in the reference method 1 h values is highest at the lowest ceiling height. This is also the region where the reference method 1 h values have the largest disagreement with the non-cooled methods. As ceiling height increases, the variation decreases within each test as well as among the methods used to calculate h. This could be attributed to the lack of sufficient cooling on the air-cooled gauge. The lowest ceiling height was at the midpoint of L_f, and therefore the heat flux gauges were subjected to the highest gas temperatures [Chapter 2]. The compressed air could not cool the gauge sufficiently or consistently at these higher rates of heat transfer to maintain a constant reference temperature on the cooled surface. This allowed the air-cooled gauge to reach varying high levels of temperature and varying levels of heat flux, changing reference throughout the entire exposure. Although this could be the cause for the high variability, more examination is needed to determine the true cause. Due to the fact that the reference method 1 produced results which were in large disagreement with the other methods, further investigation using an adequately cooled gauge is recommended.

It should be noted that the reference method 1 utilizes data throughout the whole test, however, when T_{ref} and T_s are close to each other early in the test, h is unstable and the uncertainty associated with it is high [8]. As time goes on, the h value approaches a steady value

and its uncertainty decreases. Therefore, the reference method 1 *h* is best utilized in separating the heat transfer components later in the test, once a steady value is reached.

The reference method 2 uses reference heat flux and temperatures which do not correspond to the same instance in time as the measured heat flux and temperatures, requiring that *h* remain constant throughout the entire exposure. This is most likely not the case. However, once the initial transient period of the test was surpassed, the reference method 2 gave results which were in good agreement with the slope methods. The relative variation in the reference method 2 *h* values was the lowest out of all the methods for all experimental configurations. This method used data from the non-cooled gauge only, whose measurements had good repeatability in comparison with the air-cooled measurements. It is believed that the repeatable nature of the reference used in this method decreased its overall uncertainty.

The slope method 1 requires a constant gas temperature and a transient gauge surface temperature. Thus, this method is limited in the data which can be used in the analysis. In addition, from Table 3 and Figure 3.20, the variability between tests is slightly larger than that of the slope method 2 due to this method's sensitivity to the fluctuations in the exposure heat flux [8]. The slope method 2 does not require a constant gas temperature, and therefore has fewer limitations on the portions of data which can be used in the analysis. It also decreases the variation along the linear trend through the use of the gas temperature. Further investigation is needed to determine if the interjection of the gas temperature induces a significant amount of measurement uncertainty in the calculated slope in comparison with the uncertainty from the slope method 1.

Both the reference method 2 and slope methods use data during the early and middle portions of the exposure. The slope method uncertainty is lowest during the early times in the test when the exposure heat flux is high. As the exposure heat flux decreases to values below 5 kW/m^2, its uncertainty increases significantly and so does the slope method *h* [8, 33]. Therefore, the reference method 2 and slope methods *h* are best used to separate the heat transfer components when applied to the portion of data which was used to calculate them.

It is suggested that the reference method 1 be investigated further using an adequately cooled heat flux gauge as the reference. Since the uncertainty associated with its *h* values is high in early test times, the reference method 1 *h* is best applied later in the test, when a steady state is reached. The reference method 2 and the slope methods all use data in the early and middle

portions of the exposure. Therefore, they are better used to separate the components during the early and middle times in the exposure. Applying the different methods' h values to the portions of data which was used to calculate them may help to explain some of the disagreements in the convection and irradiation components of heat transfer shown in Figure 3.18. The reference method 2, and slope methods considered in this research assume that h does not change throughout the exposure. This is most likely not true due to changing fluid properties and varying boundary conditions surrounding the ceiling surface. This uncertainty was accepted in this work, however future methods will need to be researched which take this into consideration.

3.5.3. Calculated Standard State Heat Flux

The standard state heat flux, q_o, can be solved for by rearranging Equation (3) and using the calculated h values from the reference and slope methods from Section 3.3, along with the measured heat flux and temperature from the non-cooled gauge. This calculation converts the non-cooled measurements to a standard state heat flux using a known h and assuming a standard temperature condition, T_o, of 298 K. The calculated standard state heat flux gives an indication as to whether the experimentally determined h values provide a representative standard state heat flux. Since a constant reference temperature is used, the calculated standard state heat fluxes determined using the experimentally determined h values should also be constant.

Figure 3.20 shows the results of this calculation for all experimental configurations. The methods used to calculate h using the non-cooled gauge produced similar results; therefore, the h value calculated with the slope method 2 was selected to be shown in Figure 3.20 along with those from the reference method 1. The standard state heat flux using the reference method 1 is lower than the standard state heat flux calculated using the slope method 2 and in some cases, is not constant. The L_f/H=1.5, 90 kW case decreased with time for both methods due to a decrease in the gas temperature. Standard state heat fluxes are designed to maintain a constant temperature, T_o, and a constant heat flux, q_o. The insufficient cooling to the air-cooled gauge used as the reference in the reference method 1 allowed the calculated standard state heat flux to decrease with exposure time. This decrease is more pronounced at lower ceiling heights and with larger *HRRs*, where the cooling had less of an effect on the gauge temperatures. The reference method 1 h values produced results which were not characteristic of a standard state heat flux.

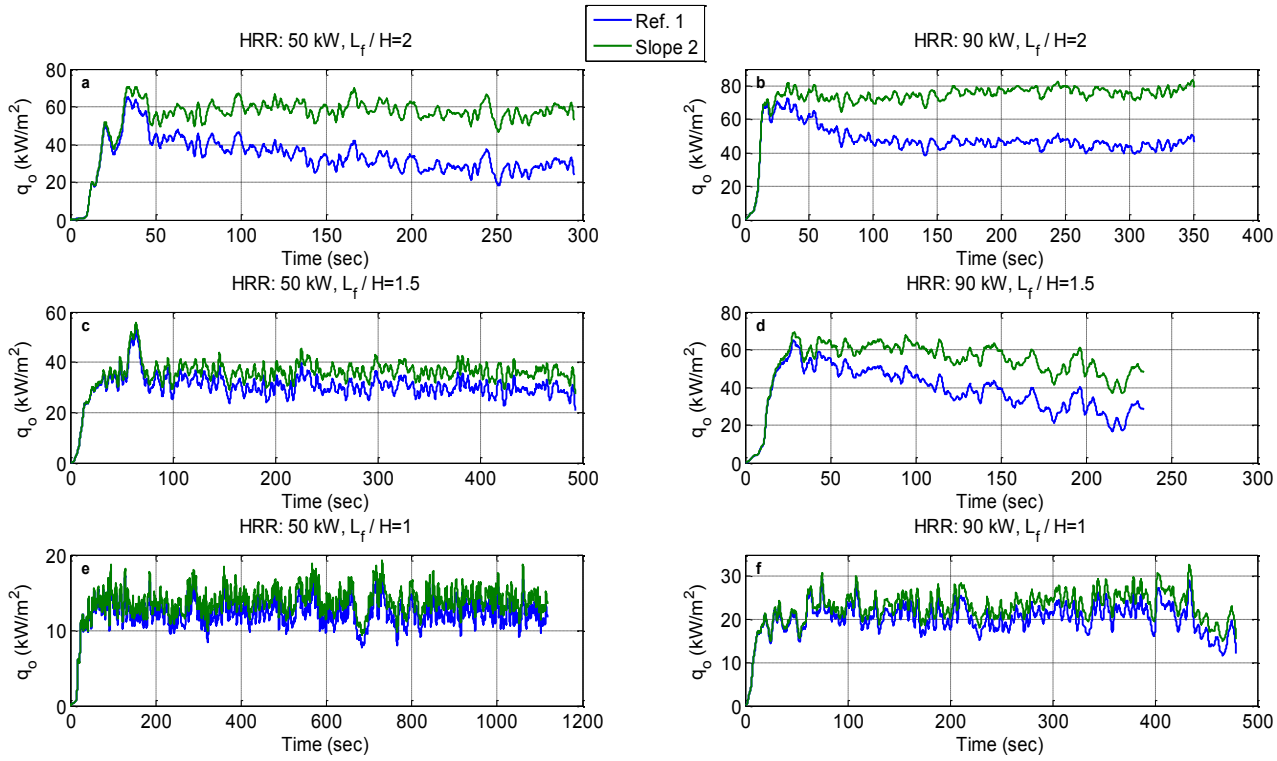

Figure 3.20: Calculated Standard State Heat Fluxes: a) 50 kW, L_f/H=2 b) 90 kW, L_f/H=2 , c) 50 kW, L_f/H=1.5, d) 90 kW, L_f/H=1.5, e) 50 kW, L_f/H=1, f) 90 kW, L_f/H=1

3.5.4. Comparison to Previous Studies

Comparisons were made between the stagnation point heat fluxes in this work to the data found in You and Faeth [19-22] and Kokkala [24]. The data from Refs.[19-22, 24] were measured using water-cooled heat flux gauges and therefore, the average calculated standard state heat fluxes from Section 3.5.3 were chosen for a comparison. Figure 3.21a shows the standard state heat fluxes plotted against L_f/H, along with the data from Kokkala [24] and You and Faeth [19]. The maximum stated heat flux of 60 kW/m^2 from Kokkala's work is also shown on the graph. This maximum occurs for $1.5<L_f/H<3.5$. The maximum heat fluxes for You and Faeth's data occurs for $L_f/H>2$ with values around 25-35 kW/m^2. The data from Ref. [19] is significantly lower in magnitude in comparison with the data from this work. This is attributed to the smaller size burners and *HRR*s used by You and Faeth. The heat fluxes from the larger scale fires are up to four times larger than those measured in the small scale experiments. The corrected standard state heat fluxes from this research match best with the results of Kokkala [24]. The data shown in Figure 3.21a shows considerable variability within the flaming region;

becoming larger as L_f/H increases. This is attributed to the variability in the h values used to calculate the standard state heat fluxes.

Figure 3.21b shows the dimensionless stagnation point heat fluxes scaled according to the correlation given in Ref. [19]. The results from this work are compared with a subset of those found in Ref. [19] and with the data from Ref. [24]. The correlation given in Ref. [19] is only applicable for $L_f/H<1.5$, when radiation losses from the surface are small, and for $10^9<Ra<10^{14}$. The Ra numbers were calculated using Equation (16) with parameters corresponding to this research. This resulted in Ra numbers larger than the bounds given by the correlation. The comparison was still made to look for similar trends among the data sets. Overall, the dimensionless stagnation point heat fluxes show the same trends with L_f/H. Smaller L_f/H result in higher dimensionless heat fluxes. You and Faeth attribute this behavior to the lower temperatures within the core of the flame [19, 22]. It is important to note that within this region, the data points measured in this research are much higher than those of Ref. [19], particularly for the 90 kW HRR. This increase in magnitude was also measured by Kokkala within the region $0.7<L_f/H<2$ [24]. Kokkala attributed this to the possibility of soot formation on the gauges within this region of the flame. This difference could also be caused by the larger scale fires investigated in this research, which produce larger Ra numbers. This supports the idea that small scale fire testing cannot be extrapolated to larger, more realistic size fires.

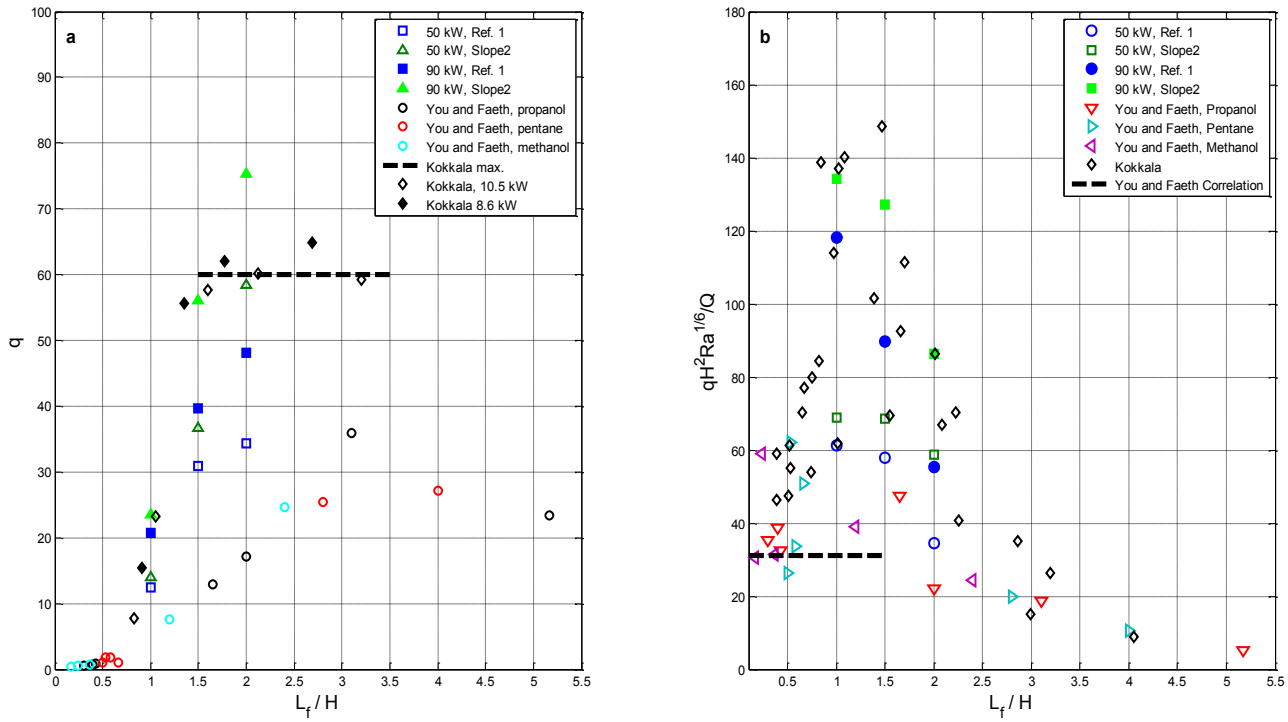

Figure 3.21: Comparison of Experimental Data with Refs. [19, 24], a) q_o vs. L_f/H b) non-dimensional q_o vs L_f/H

Other studies which tried to quantify the convective coefficient of heat transfer were those of Donaldson et al. [23] and Cooper [17]. Donaldson et al. considered the case of a momentum dominated turbulent jet at ambient temperature impinging onto a heated plate. A correlation for laminar flow was used in conjunction with turbulent measurements of the velocity gradient at the wall. Cooper considered a buoyantly driven plume of hot combustion gases impinging onto a ceiling kept at ambient temperature. He developed a correlation based on the formulations and data from You and Faeth [20], Donaldson et al. [23], and Veldmen et al. [35]. Fire Dynamic Simulator uses a combination of natural convection and turbulent boundary layer correlations over a flat plate for determining *h* [3]. Applying the correlations from Refs. [3, 17, 23] to the data collected in this work result in the *h* values shown in Table 3.5. This is considered to be a rough comparison; therefore, values should not be compared for accuracy. It should be noted that the *h* values calculated using the methods in this research are within the range of the correlations given by Cooper and Donaldson et al. This is encouraging since these correlations were developed from theory and data from cases which matched more closely with the experiments in this research. On the other hand, the results from the FDS correlations are

much smaller than those calculated here or in the other papers. This shows that the current methods of estimating the convective heat transfer coefficient in fire models are not sufficient for real fire scenarios. It also shows that there is disagreement between the methods of estimating *h*. Further experimental quantification is required for more accurate estimates.

Table 3.5: Correlations from Ref. [3, 17, 23]

Q (kW)	L_f/H (--)	Cooper (kW/m^{2}K)	Donaldson et al. (kW/m^{2}K)	FDS natural (kW/m^{2}K)	FDS Forced (kW/m^{2}K)
50	2	0.037	0.044	0.0072	0.0083
	1.5	0.048	0.060	0.0068	0.010
	1	0.058	0.075	0.0065	0.012
90	2	0.034	0.038	0.009	0.010
	1.5	0.044	0.052	0.0077	0.0094
	1	0.054	0.066	0.0066	0.013

The work of Weng and Hasemi [25] was the only study which tried to directly solve for *h* for a diffusion flame impinging onto a ceiling. Their model was based on energy balances on the ceiling surface; similar to the work done in this research. Their experimental data was scaled to follow the form of Cooper's correlation [17] based on plume theory and an equation was determined using a curve fit to the scaled experimental data. The results of applying their correlation to the experimental data in this study are shown in Figure 3.22 along with the calculated *h* values from the reference method 1 and slope method 2 discussed above. The comparison indicates that results from the slope method 2 match more closely with the correlation developed by Weng and Hasemi. The trends in the *h* are the same, slightly decreasing with increasing ceiling height. This is encouraging for the non-cooled methods, however the radiation estimated in Ref. [25] was significantly lower than that measured in this research. This could provide a false agreement, where the larger *h* values published in Ref. [25] could be attributed to the lower amount of radiation to the ceiling. Weng and Hasemi also cautioned that their model overestimated the heat fluxes to the ceiling. This could also cause differences between the calculated *h* values in this work and those of Ref. [25].

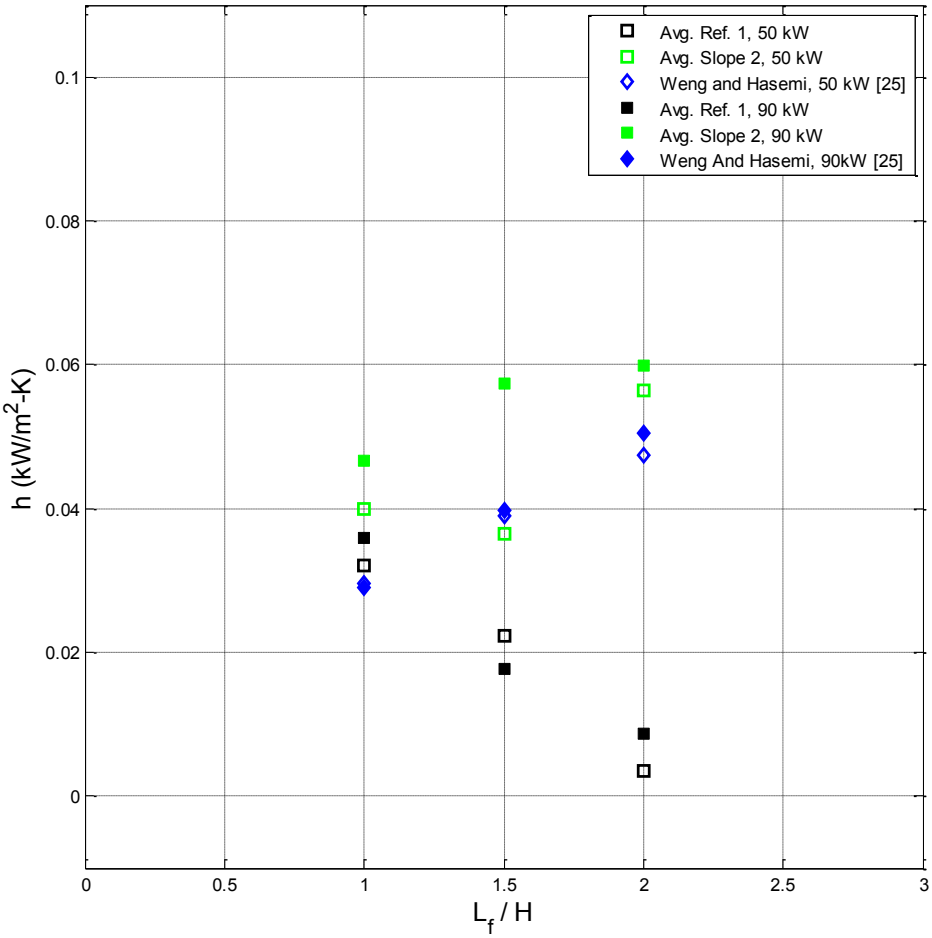

Figure 3.22: Comparison of Calculated *h* Values with Ref. [25]

3.6. Conclusions

The convection and irradiation components of heat transfer from an impinging diffusion flame to a ceiling were calculated using *h* values determined with four different methods: reference method 1, reference method 2, slope method 1, and slope method 2. The reference method 1 required the use of two heat flux gauges; an air-cooled reference and a non-cooled hybrid gauge. The reference method 2, slope method 1, and slope method 2 required the use of only the non-cooled heat flux measurements. The latter three methods resulted in *h* values which were in good agreement with one another. They produced heat transfer components which decreased slightly with ceiling height and increased slightly with *HRR*. The reference method 1 *h* values disagreed largely with the other methods, with values up to 15.8 times lower in magnitude. Its *h* values increased with ceiling height and with *HRR*. The disagreement was largest at the L_f/H=2 and L_f/H=1.5 ceiling heights. The components of heat transfer were

separated using the four calculated h values. Components were greatly influenced by the disagreements between the calculated h values. This was particularly true for the L_f/H=2 ceiling height where the convection calculated with the reference method 1 h values contributed 2-5% of the total exposure, and the convection calculated with the other methods contributed 20-50% of the total. Better agreement between methods was achieved at higher ceiling heights. Corrected standard state heat fluxes revealed uncharacteristic results using the reference method 1 h values. From the analysis, the different methods are best applied at different times during the exposure. The reference method 1 should be applied later in the test, while the reference method 2, and both slope methods are best applied during early and middle times during the exposure. At this point, a clear method cannot be chosen. The large disagreements between methods prompt further investigation into the methods and the assumptions made when using them. It is suggested that a more detailed characterization of the methods be performed in a more controlled environment such as the cone calorimeter and with the reference gauge provided with sufficient cooling. Gas temperatures in these experiments should be close to those measured in this research to simulate fire conditions.

3.7. Acknowledgements

The authors would like to thank Joshua McNeil, Christian Rippe, Akashdeep Singh Virk, and Philip Jones for their help in setting up and running experiments.

References

1. Hinkley, P.L, Wraight, H.G.H., Theobald, C.R., The contribution of flames under ceilings to fire spread in compartments, Fire Safety Journal 7 (1984) 227-242.
2. Hasemi, Y., Firesafety of building exposed to a localized fire-scope and experiments on ceiling/beam system exposed to localized fire, in 1st International Conference ASIAFLAM (1995) 351-361.
3. J. Floyd, G. Forney, S. Hostikka, T. Korhonen, R. McDermott, and K. McGrattan, Fire dynamics simulator user's guide, Gaithersburg, Maryland, USA (2013).
4. Nakos, J.T., Uncertainty analysis of steady state incident heat flux measurements in hydrocarbon fuel fires, United States, Department of Energy, 2005.

5. Gifford, A., Hubble, D.O., Pullins, C.A., Diller, T.E., Huxtable, S.T., Durable heat flux sensor for extreme temperature and heat flux environments, Journal of Thermophysics and Heat Transfer 24 (2010) 69-76.
6. Vega, T., Lattimer, B.Y., and Diller, T.E., Fire thermal boundary condition measurement using a hybrid heat flux gage, Fire Safety Journal **61** (2013) 127-137.
7. Vega, T., Lattimer, B.Y., and Diller, T.E., Temperature predictions using hybrid heat flux measured boundary conditions, submitted to Fire Safety Journal (2012).
8. Vega, T., Wasson, R., Lattimer, B.Y., and Diller, T.E., Partitioning measurements of Convective and Radiative Heat Flux, submitted to International Journal of Heat and Mass Transfer (2014).
9. Diller, T. E., Heat flux measurement, Ch. 18, in Handbook of Measurement in Science and Engineering, Ed. M. Kutz, John Wiley & Sons, NY (2013) 639-643.
10. Lattimer, B.Y., Heat fluxes from fires to surfaces, The SFPE Handbook of Fire Protection Engineering (4th Ed.), P.J. DiNenno (ed.), National Fire Protection Association, Quincy, MA, (2007).
11. Lattimer, B. Y. and Ouellette, J., Properties of composite materials for thermal analysis involving fires, Composites Part A: Applied Science and Manufacturing 37(7) (2006) 1068-1081.
12. Lattimer, B.Y., Vandsburger, U., and Langley, L.W., Detecting fires using a thin-film heat flux microsensor, ASME Winter Annual Meeting, Chicago, Illinois, HTD, Vol. 296, November (1994) 137-142.
13. Lennon, P. and Silcock, G., A Preliminary Investigation into the Partitioning of the Convective and Radiative Incident Heat Flux in Real Fires, Fire Technology 42(2) (2006) 109-129.
14. Blanchat, T., O'Hern, T., Kearney, S., Ricks, A., and Jernigan, D., Validation experiments to determine radiation partitioning of heat flux to an object in a fully turbulent fire, in: Proceedings of the Combustion Institute 32(2) (2009) 2511-2518.
15. Nakos, J. T., Keltner, N.R., The radiative-convective partitioning of heat transfer to structures in large pool fires, American Society of Mechanical Engineers, Heat Transfer Division, HTD 106 (1989).

16. Zhang, J., Delichatsios, M.A., Determination of the convective heat transfer coefficient in three-dimensional inverse heat conduction problems, Fire Safety Journal 44 (2009) 681-690.
17. Cooper, L.Y., Heat transfer from a buoyant plume to an unconfined ceiling, Journal of Heat Transfer ASME 104 (1982) 446-451.
18. Alpert, R.L., Turbulent ceiling-jet induced by large-scale fires, Combustion Science and Technology 11 (1975) 197-213.
19. You, H-Z., Faeth, G.M., An investigation of fire impingement on a horizontal ceiling, Report NBS-GCR-79-188, National Bureau of Standards (1978).
20. You, H.Z., Faeth, G.M., Ceiling heat transfer during fire plume and fire impingement, Fire and Materials 3 (1979) 140-147.
21. You H.Z., An investigation of fire-plume impingement on a horizontal ceiling, Fire and Materials 9 (1985) 46-56.
22. You, H-Z., Faeth, G.M., An investigation of fire impingement on a horizontal ceiling, Report NBS-GCR-80-251, National Bureau of Standards (1979).
23. Donaldson et al., C.D., Snedeker, R.S., Margolis, D.P., A study of free jet impingement. Part 2. Free jet turbulent structure and impingement heat transfer, Journal of Fluid Mechanics 45 (1971) 477-512.
24. Kokkala, M.A., Experimental study of heat transfer to ceiling from an impinging diffusion flame, in: Proceedings of the 3rd International Symposium on Fire Safety Science (1991) 261-270.
25. Weng, W.G., and Hasemi, Y., Heat transfer to an unconfined ceiling from an impinging buoyant diffusion flame, Heat and Mass Transfer 42 (2006) 652-659.
26. Sibulkin, M., Heat transfer near the forward stagnation point of a body of revolution, Journal of Aero Science 19 (1952) 570-571.
27. Rouse, H., Yih, C.S., Humphreys, H.W., Gravitational convection from a boundary source, Tellus 4 (1952) 201.
28. Hubble, D.O., Diller, T.E., A hybrid method for measuring heat flux, ASME Journal of Heat Transfer 132 (2009) 132-138.
29. Pullins, C., In situ high temperature heat flux sensor calibration, International Journal of Heat and Mass Transfer 53 (2010) 3429-3438.

30. Blevins, L.G. , Pitts, W.M., Modeling of bare and aspirated thermocouples in compartment fires, Fire Safety Journal 33 (4) (1999) 239-259.
31. McCaffrey, B.J., Heskestad, G., A robust bidirectional low-velocity probe fore flame and fire application, Combustion and Flame 26 (1976) 125-127.
32. Drysdale, D., An introduction to fire dynamics, Third Ed,. Scotland, UK (2011).
33. Bryant, R., Womeldorf, C., Johnsson, E., Ohlemiller, T., Radiative heat flux measurement uncertainty, Fire and Materials 27 (2003) 209-222.
34. Cengel, Y.A., Ghajar, A.J., Heat and Mass Transfer Fundamentals and Applications, Fourth Ed., New York (2010).
35. Veldmen, C.C., Kubota, T., and Zukoski, E.E., An experimental investigation of the heat transfer from a buoyant gas plume to a horizontal ceiling-part 1: unobstructed ceiling, Report NBS-GCR-77-97 (1975).
36. Pullins, C.A., High temperature heat flux measurement: sensor design, calibration, and applications, Virginia Tech Dissertation (2011) 120.

4. Conclusions and Recommendations

4.1. Conclusions

Measurements of time averaged gas temperature and velocity along the centerline of a fire plume impinging onto a ceiling showed that the gas temperature close to the burner surface remained relatively constant, with little dependence on *HRR* and ceiling height. The velocities near the burner increased with z, and were independent of ceiling height, yet had a slight dependence on *HRR*. As elevation above the burner increased, gas temperature decreased and the fire plume velocity increased to a maximum. Within the intermittent region of the flame, gas temperature and velocity increased significantly with *HRR*. Velocity increased with ceiling height, while gas temperature decreased slightly with an increase in ceiling. At 70% of the ceiling height, both parameters decreased significantly as the flame reached the impingement point. The experimental results of this work match the correlations developed by McCaffrey the best, with slightly lower temperatures and velocities. The presence of the ceiling had a substantial effect on the velocities within the flame, which was not discussed in previous work. The fire plume correlations can be used as a good approximation for the gas temperature; however, the velocity correlations should only be used up to elevations which are below 60% of the ceiling height. Anything above this region is where the unbounded fire plume correlations break down due to the presence of the ceiling. The comparison between the experimental results and the FDS simulation were favorable, with maximum temperatures within 5.74 % and maximum velocities within 11.6%.

The convection and irradiation components of heat transfer from an impinging diffusion flame to a ceiling were separated using h values determined from four methods: reference method 1, reference method 2, slope method 1, and slope method 2. The latter three methods resulted in h values which were in good agreement with one another. They produced heat transfer components which decreased slightly with ceiling height and increased slightly with *HRR*. The reference method 1 h values disagreed largely with the other methods, with values up to 15.8 times lower in magnitude. Its h values increased with ceiling height and with *HRR*. The disagreement was largest at the L_f/H=2 and L_f/H=1.5 ceiling heights, where the compressed air could not sufficiently cool the gauge; allowing the gauge temperature to change throughout the exposure, increasing the variation between tests. The components of heat transfer were

separated using the four calculated *h* values. Components were greatly influenced by the disagreements between the calculated *h* values, particularly at the L_f/H=2 ceiling heights where the convection calculated with the reference method 1 *h* values contributed 2-5% of the total exposure, and the convection calculated with the other methods contributed 20-50% of the total. Corrected standard state heat fluxes revealed uncharacteristic results when using the reference method 1 *h* values. Such large disagreements prompt further investigation into the methods and the assumptions made when using them.

4.2. Recommendations for Future Work

Although, it has been shown that the methods can work in the fire scenario, a step back needs to be taken to characterize each method's limitations in a more controlled environment. Therefore, it is suggested that experiments be conducted in the cone calorimeter. Conditions should be kept as close as possible to those measured in this work to simulate a real fire scenario. It is especially important to replicate the high gas temperatures present in a real fire. The reference method 1 should be implemented using a true standard state heat flux measured by a hybrid gauge with active cooling. The cooling should be adequate to ensure that the back surface temperature of the gauge is kept at a constant value close to 298 K. A non-cooled hybrid gauge can then be used to measure the elevated temperature heat flux. This will provide a constant boundary condition on the back surface of the gauge and a true measurement of the standard state heat flux and temperature, helping to reduce variation in the calculated *h* values. Varying reference temperature should also be investigated to determine if there are any temperature limitations on the reference method 1. This method assumes that *h* is independent of either surface temperature; however, it seems likely that the method is dependent on the temperature difference between surfaces. It has already been determined that small temperature differences result in high uncertainties for this method. From the data in this research, it is possible that high temperature differences result in high uncertainties as well. Using the cone calorimeter to test the method at different levels of reference temperature will help to reveal any temperature dependencies/limitations this method may have. The other four methods should be implemented using the data from these experiments and compared to the reference method 1.

The measurement uncertainty in the gas temperature should be characterized. This will allow the uncertainty of the slope method 2 to be calculated. This information would be useful in trying to evaluate the method further. Comparisons of uncertainties should be made between

the slope method 1 and slope method 2 so that efforts can be focused on the best method of calculating h.

If experiments are to be run using the diffusion flame, it is suggested that the gauges be kept at a constant temperature during the initial ramp up time of the fire. This can be done using an actively cooled ceiling. The gauges and ceiling should be kept at a constant temperature with the coolant, until gas temperature is constant, measure at this constant temperature for two minutes, then shut off cooling and allow both gauge and ceiling temperature to rise. The methods can then be applied. This ensures that the gas temperature is constant throughout the exposure and thus, h should be constant also. This way, the exposure fluxes are not limited in the slope method 1 and the methods apply at all times.

A better quantification of the emissivity of the gauges during the experiment needs to be developed. Soot collection on the gauge could cause a violation of the reference methods of calculating h. This could be accomplished through spectral analysis, or through a more rigorous calibration procedure. A model for variable emissivity could also be developed to better characterize the changing emissivity throughout the exposure from the flame to the ceiling. This model should include a dependency on temperature as soot collection on surfaces could be a function of the temperature difference between the surface and the surrounding gas.

Cross correlation techniques should be carried out on measurements of the air-cooled and non-cooled gauge heat fluxes to determine if the assumptions of the same irradiation and same fluid properties were valid throughout the experiment. If the two measurements have a large lag between them, then it can be concluded that the two gauges were not subjected to the same conditions.

The methods used to calculate h in this thesis, assume that h is constant throughout the exposure. As mentioned earlier, this is likely not true due to varying fluid properties and flow conditions. Once the methods and their limitations are better characterized, methods should be developed to account for varying fluid conditions and irradiation.

It may be interesting to look into characterizing the radiation from the flames using thermal imaging techniques such as an infrared camera. The flame temperatures could be quantified pretty accurately with a FLIR infrared camera. This would require the flow to be seeded with ceramic particles and the ceramic particle temperature to be measured. This would help to better understand the temperatures present within the flaming region.

APPENDIX A- UNCERTAINTY CALCULATIONS IN REFERENCE METHOD 1 AND SLOPE METHOD 1

An uncertainty analysis was performed on both the reference and slope methods for calculating the convective heat transfer coefficient for the data in Ref. [8]. The reference method uncertainty was determined using the law of propagation of uncertainty as outlined in the Guide to the Expression of Uncertainty in Measurement (GUM) [A.1] whereas the slope method uncertainty was found using a regression uncertainty technique similar to that outlined in Coleman and Steele [A.2].

Relative Uncertainty in Non-cooled heat flux

In order to calculate the uncertainty in either method, the uncertainty in the measured non-cooled heat flux had to be quantified. The uncertainty in the non-cooled heat flux was determined using the methodology outlined in Ref. [A.1]. The calculated sensitivity coefficients are shown in Equations (A.1-A.4). This uncertainty was required to evaluate the uncertainty in the reference method 1.

$$c_1 = \frac{\partial q_{net}}{\partial voltage} = \frac{1}{S} \tag{A.1}$$

$$c_2 = \frac{\partial q_{net}}{\partial S} = \frac{-voltage}{S^2} \tag{A.2}$$

$$c_3 = \frac{\partial q_{net}}{\partial \rho c_p \delta} = \frac{1}{2}\frac{dT}{dt} \tag{A.3}$$

$$\mathbf{c_4} = \frac{\partial q_{net}}{\partial \dfrac{dT}{dt}} = \frac{1}{2}\rho c_p \delta \tag{A.4}$$

Table A.1 provides the individual uncertainty components for the non-cooled heat flux.

Table A.1: Non-cooled heat flux Uncertainty Components

x_i	Uncertainty type	$u(x_i)$	Comments
Gauge voltage	A	6.13 (μV)	Unbiased sample standard deviation of raw measured voltage
S	B	14.8 (μV/(W/cm^2))	Stated from previous analysis [29]
$\rho c_p \delta$	B	0.03(Ws/cm^2-C)	Estimated from previous calibration
$\frac{dT}{dt}$	A	0.01 $\frac{C}{s}$	Unbiased sample standard deviation of measured data

The relative uncertainty in the non-cooled heat flux for the convection only case is shown in Figure A.1a. The uncertainty in the non-cooled heat flux ranges in time from ~4.5% to ~6%,

with low heat fluxes resulting in higher relative uncertainties. This trend agrees with those found in the literature [A.3]. The relative uncertainty in the non-cooled heat flux for the mixed mode environment is shown in Figure A.1b. The uncertainty in the non-cooled heat flux ranges from 5% to 12% until about 500 seconds where it becomes increasingly large. This occurs roughly when the heat flux became small and passed through zero. These heat flux values were neglected in the uncertainty analysis and the uncertainties associated with them are not shown in Figure A.1b.

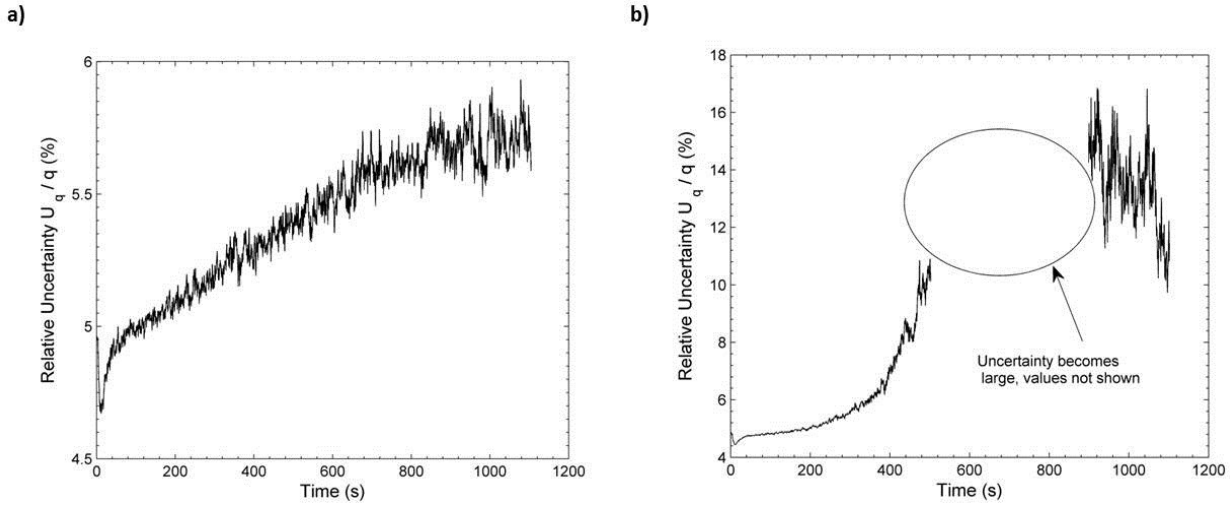

Figure A.1. Relative Uncertainty in Non-cooled heat flux in a) convection only and b) mixed-mode environments

Reference Method Uncertainty

The reference method uncertainty is expressed as a root-sum-square of the individual measured input uncertainties,

$$u_c^2(h) = \sum_{i=1}^{N}\left(\frac{\partial h}{\partial x_i}\right)^2 u^2(x_i) + 2\sum_{i=1}^{N-1}\sum_{j=i+1}^{N}\frac{\partial h}{\partial x_i}\frac{\partial h}{\partial x_j}u(x_i,x_j) = \sum_{i=1}^{N}c_i^2 u^2(x_i) + 2\sum_{i=1}^{N-1}\sum_{j+i+1}^{N}c_i c_j u(x_i)u(x_j)r(x_i,x_j) + u_{rep}^2 \quad \text{(A.5)}$$

where h is the heat transfer coefficient from Equation (8), the $x_i x_i, x_j$ terms are the measured input variables of Equation (8),thec_i c_i, c_j terms are the sensitivity coefficients, and u_{rep} is the uncertainty attributed to repeatability of the experiment. The second terms on the right hand side of each equals sign represents any correlated uncertainties in the input variables where $r(x_i, x_j)$ is the degree of correlation between the variables. For this work, the measured non-cooled heat flux and gauge surface temperature in Equation (8) were considered to be correlated with a

degree of correlation of -1. This correlation must be considered because $q_{meas,non-cooled}$ will change along with a change in T_s. The complete expression for the combined uncertainty in the value of *h* evaluated using the reference method 1 becomes:

$$u_c^2(h) = \left\{ \begin{array}{l} c_1^2 u_{q_{meas,air-coooled}}^2 + c_2^2 u_{q_{meas,non-cooled}}^2 + c_3^2 u_{\varepsilon_s}^2 + c_4^2 u_{T_s}^2 + c_5^2 u_{T_{ref}}^2 \\ + 2\left[c_{qmeas,\,non-cooled}\; {}^{c}{}_{T_S}\, u_{q_{meas,cnon-cooled}}\, {}^{u}{}_{T_S} (-1) \right] + u_{rep}^2 \end{array} \right\} \tag{A.6}$$

A relative uncertainty is determined by dividing through by the heat transfer coefficient. The calculated sensitivity coefficients are defined in Equations (A.7-A.11) and shown in Figure A.2.

$$c_1 = \frac{\partial h}{\partial q_{meas,air-cooled}} = \frac{1}{T_s - T_{ref}} \tag{A.7}$$

$$c_2 = \frac{\partial h}{\partial q_{meas,non-cooled}} = \frac{-1}{T_s - T_{ref}} \tag{A.8}$$

$$c_3 = \frac{\partial h}{\partial \varepsilon_s} = \frac{-\sigma\left(T_s^4 - T_{ref}^4\right)}{T_s - T_{ref}} \tag{A.9}$$

$$c_4 = \frac{\partial h}{\partial T_s} = \frac{\left(-\left(q_{meas,air-cooled} - q_{mwas,non-cooled}\right) - \varepsilon_s \sigma\left(3T_s^4 - 4T_s^3 T_{ref} + T_{ref}^4\right)\right)}{\left(T_s - T_{ref}\right)^2} \tag{A.10}$$

$$c_5 = \frac{\partial h}{\partial T_{ref}} = \frac{\left(\left(q_{meas,air-cooled} - q_{mwas,non-cooled}\right) - \varepsilon_s \sigma\left(T_s^4 - 4T_{ref}^3 T_s + 3T_{ref}^4\right)\right)}{\left(T_s - T_{ref}\right)^2} \tag{A.11}$$

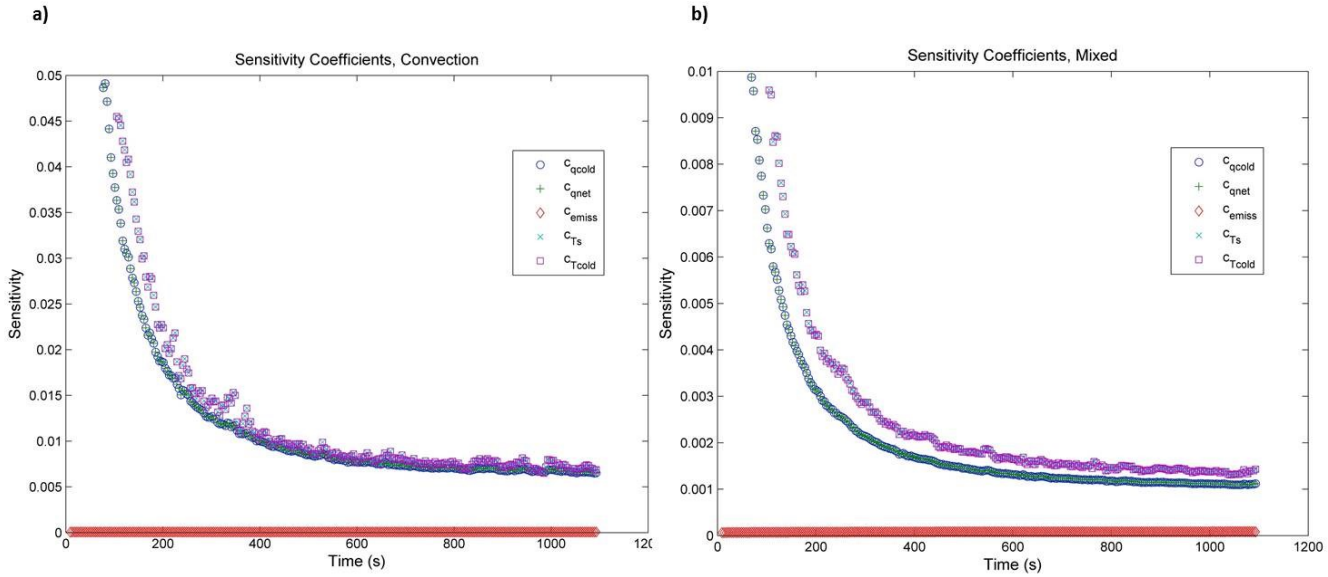

Figure A.2. Reference Method Squared Sensitivity Coefficients: a) convection only, and b) mixed mode

Table A.2 summarizes the individual uncertainty quantities used to determine the combined uncertainty in the value of *h* evaluated using the reference method.

Table A.2: Uncertainty Budget for Reference Method Coefficient of Heat Transfer

x_i	Uncertainty type	$u(x_i)$		Comments
$q_{meas,air-cooled}$	A,B-random and bias	Convection	Mixed	Law of propagation of uncertainty of hybrid heat flux method (Equations 4- 6)
		5.04 %	4.95%	
$q_{meas,non-cooled}$	A,B-random and bias	Convection	Mixed	Law of propagation of uncertainty of hybrid heat flux method (Equations 4- 6)
		4.5-6% (Fig. A.2a)	4.95-12% (Fig. A.2b)	
ε_s	B-bias	3%		Must be estimated since no data is available for this quantity (k=2)
σ	B-bias	0		Assumed no uncertainty, therefore not included in analysis
T_s	A-random	Convection	Mixed	Root mean square error from a fitted line
		0.178-0.186%	0.185-0.202%	
T_s	B-bias	1.1˚C		As stated from manufacturer
T_{ref}	A,B-random and bias	Convection	Mixed	Root sum square of variance of T_{ref} measurements and type B uncertainty of T_s
		0.18%	0.17%	
u_{rep}	B-bias	4%		Repeatability uncertainty calculated from the averages from

			the three experimental runs

The uncertainty in the measured non-cooled heat flux was determined by applying the law of propagation of uncertainty (Equation A.5) to the hybrid heat flux method obtained by substituting Equations (4-5) into Equation (6). It was found that lower measured heat fluxes resulted in higher relative uncertainties which describe the ranges found in Table 1. This trend agrees with those found in the literature [A.3]. It should be noted that the mixed-mode relative non-cooled heat flux uncertainty became increasingly large at about 500 seconds into the test. This occurs roughly when the non-cooled heat flux became small and passed through zero. These heat flux uncertainty values are also consistent with Ref. [A.3] and were neglected in the analysis.

Figure A.3 shows the relative heat transfer coefficient uncertainties for the convection only and the mixed-mode environments after 80 seconds, when the initial instability due to small differences between T_s and T_{cold} has settled out. An average uncertainty value is also shown, with the average being taken on data after 300 seconds.

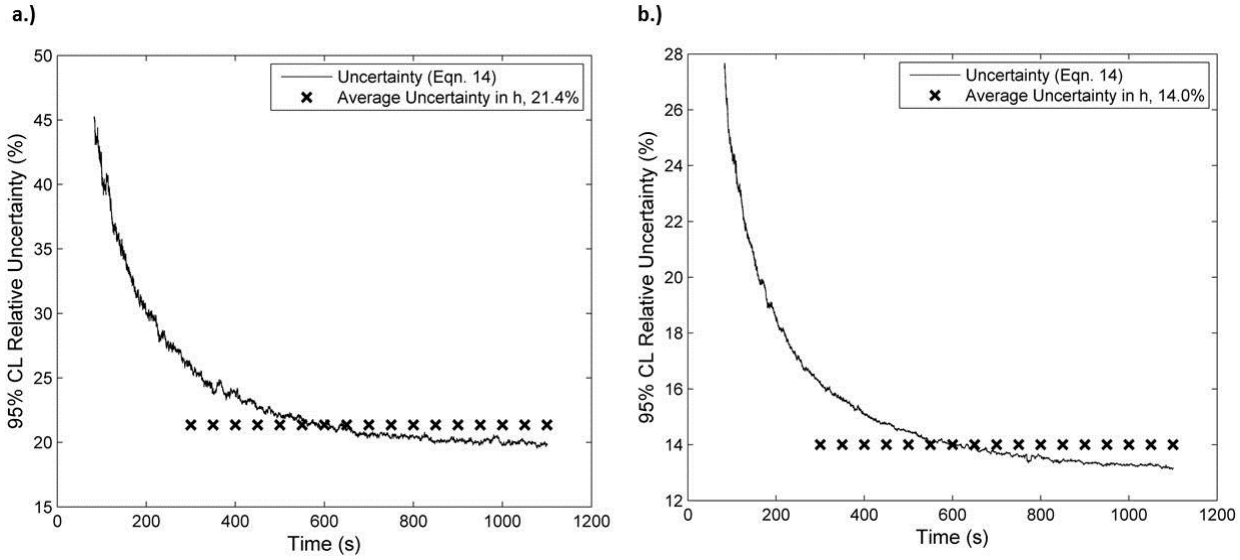

Figure A.3. 95% CL Relative Uncertainty in Reference Method Heat Transfer Coefficient in a) convection only and b) mixed-mode environments.

The 95% level of confidence (k= 2) test average relative uncertainty in *h* for the convection only case, shown in Figure A.3a, is ±21.4% (±0.22 kW/m^2-˚C) of the calculated test average *h* value of 1.03 kW/m^2-˚C. The 95% level of confidence (k= 2) test average relative uncertainty in *h* for

the mixed mode case, shown in Figure A.3b, is ±14.0% (±0.16 kW/m^2-˚C) of the calculated test average h value of 1.11 kW/m^2-˚C.

The greatest contributors to the reference method uncertainty were q''_{cold}, T_s and T_{cold}. The sensitivities of T_s and $q_{meas,non-cooled}$ were very similar; both negative with T_s being slightly more negative than $q_{meas,non-cooled}$. However, since the sensitivity coefficients are squared, c_{T_s} becomes slightly larger. In addition, the uncertainty contribution from $q_{meas,non-cooled}$ is initially larger than T_s, however as q''_{net} decreases, so does its uncertainty and therefore the uncertainty from T_s becomes larger than the uncertainty of $q_{meas,non-cooled}$.

The heat transfer coefficient uncertainty in the convection only environment is larger than that of the mixed mode. This is attributed to the change in the gauge surface temperature with time from its initial water cooled temperature to its transient, elevated temperature. This change in gauge surface temperature appears in the denominator of each sensitivity coefficient, therefore, as the gauge surface temperature increased with time, the sensitivity coefficients decreased with time to values smaller than one. These values were then squared in the uncertainty equation making them even smaller. Since the convection only environment had a smaller gauge surface temperature change than the mixed-mode case, as shown in Figure 4, its sensitivity coefficients were larger and therefore its overall uncertainty was larger. This is solely an artifact of the experiment and does not necessarily mean that the mixed-mode environment produces a heat transfer coefficient which is more accurate than that of a convection only environment. It simply reveals that if the reference method is to be used as a way to calculate the heat transfer coefficient in this type of experiment, then the experiment should be set up so as to increase the temperature difference between the gauge surface and the initial water-cooled surface in order to decrease the uncertainty of the heat transfer coefficient. This behavior indicates that the reference method uncertainty is highly dependent on the type of environment in which the measurements are made.

Figure A.3 shows that the uncertainty during the transient period of both experiments is much larger than the steady period. This behavior can also be attributed to the difference in the gauge surface temperature and the initial water-cooled surface temperature. As this difference

increases, the sensitivity coefficients decrease and therefore the uncertainty decreases. Therefore, if smaller measurement uncertainties in h are desired, the reference method should be used in situations in which there is a large change in the surface temperature.

Slope Method Uncertainty

Quantifying the uncertainty in the slope method requires calculating the uncertainty in a linear regression. The method used to do this is similar to that outlined by Coleman and Steele [A.2]. This method provides a more general uncertainty than the random standard curve fit uncertainty because it includes both random and bias uncertainties as well as any correlated bias uncertainties in the regression variables. The 95% level of confidence uncertainty equation for the slope in a linear regression equation is given by,

$$U_m^2 = 2^2 \left[\begin{array}{l} \left(\frac{\partial m}{\partial Y}\right)^2 u^2(Y)_{bias} + \left(\frac{\partial m}{\partial Y}\right)^2 u^2(Y)_{random} + \left(\frac{\partial m}{\partial X}\right)^2 u^2(X)_{bias} + \left(\frac{\partial m}{\partial X}\right)^2 u^2(X)_{random} \\ + 2\left(\frac{\partial m}{\partial Y}\right)\left(\frac{\partial m}{\partial X}\right) u(X,Y)_{bias} \end{array} \right] \tag{A.12}$$

where in this case, Y is the exposure heat flux to the gauge defined by Equation (12), X is the measured gauge surface temperature, m is the heat transfer coefficient, and the partial derivatives are the sensitivity coefficients of *h*. The first four terms take into account the random and bias uncertainty in the exposure heat flux as well as the gauge surface temperature. The last term accounts for the correlated bias uncertainties in the exposure heat flux and the gauge surface temperature. These terms must be accounted for since $q''_{\exp}$ is calculated using T_s.

The uncertainty for the exposure heat flux was calculated using the same methodology as for the non-cooled heat flux described above. This uncertainty was determined to be dominated by the non-cooled heat flux uncertainty, with little contribution from the reradiation term. The random and bias uncertainties in the surface temperature were the same values specified in Table A.2. A perturbation technique was employed to determine the sensitivity coefficients. To determine the sensitivities, numbers were added in 1% increments from 1-10% of each data point for the input variables. Table A.3 summarizes the sensitivity coefficients for the convection only and the mixed mode environments.

Table A.3 Sensitivity Coefficients of Slope Method

	$\frac{\partial m}{\partial Y}\left(\frac{Y}{m}\right)$	$\frac{\partial m}{\partial X}\left(\frac{X}{m}\right)$
Convection Only	1.00	-0.95

Mixed Mode	1.00	-0.95

The sensitivity coefficients show that, in general, the uncertainty in the heat transfer coefficient is more sensitive to a change in the exposure heat flux rather than in the temperature. The uncertainty in the heat transfer coefficient is insensitive to the thermal environment. .

The relative uncertainty of h for the convection only case was ±10.2% (±0.10 kW/m^2-˚C) of the calculated h value of 0.94 kW/m^2-˚C. The relative uncertainty of h for the mixed-mode case was ±11.3% (±0.11 kW/m^2-˚C) of the calculated h value of 1.00 kW/m^2-˚C. The mixed-mode uncertainty was averaged before the point where the non-cooled heat flux uncertainty increased rapidly as discussed earlier. The results of both the convection and mixed-mode cases revealed that the slope method uncertainty is driven by the uncertainty in the exposure heat flux, with a small contribution from the gauge surface temperature and a small negative contribution from the correlated terms. This could be a drawback when using the slope method in a mixed-mode environment with small exposure heat flux values. Therefore the reference method may be better in this scenario, whereas the slope method is better early on in the test. The results also indicate that the slope method uncertainty is relatively insensitive to the type of environment in comparison to the reference method. This can be attributed to the elimination of the dependence on the difference between the elevated gauge surface temperature and the cold surface reference temperature. Thus, if it is desired to bypass the effect of gauge surface temperature change, the slope method would be the more robust method to calculate the heat transfer coefficient.

When interpreting these results, keep in mind that the uncertainty values stated are the uncertainties in the measurements and methods used to determine the heat transfer coefficient, not the absolute error from the true value. It provides insight into the dispersion of values of the heat transfer coefficient to the resultant value as well as how to improve the estimate of the heat transfer coefficient with the current knowledge of the measurand [A.1].

[A.1] JCGM 100:2008, Evaluation of measurement data-Guide to the expression of uncertainty in measurement (GUM), first ed., JCGM, 2008.

[A.2] Coleman, H.W. and Steele, W.G., “Experimentation, Validation, and Uncertainty Analysis for Engineers”, Third Edition, John Wiley & Sons, Inc., Hoboken, NJ, 2009.

[A.3] Bryant, R., Womeldorf, C., Johnsson, E., Ohlemiller, T., “Radiative Heat Flux Measurement Uncertainty”, *Fire and Materials*, **27**, pp. 209-222, 2003.

APPENDIX B- CALIBRATION PROCEDURES AND CALCULATED GAUGE SENSITIVITIES

Radiation Calibration using Lamp

Introduction:

This document serves as a guideline for all heat flux gauge lamp calibrations in 100V. It is best to try and follow these procedures to ensure consistent calibration methods are being used.

Equipment:

Halogen Lamp:

- USHIO J120V-250W/79 halogen bulbs
- Life of 2000 hours
- Lamp has focal point of 1.25" away from its face

Model SC-10T Variac:

- 0-130 VAC
- Max 1000W
- 117VAC, 60 Hz input

HP 3468A True RMS Multimeter:

- We want to measure AC

HTHFS and SB gauge with holders:

- Each has their own plate holder. We want to figure this out.
- SB gauge has sensitivity of 625.19 uV/(W/cm^2). It is used to calibrate the lamp.

Gauge Holster:

- Same gauge holster used for both SB and HTHFS

NI cDAQ 9172:

- 24 bit Sigma delta A/D
- 9213 thermocouple module
- 9219 voltage module
- HTHFS TC1 and TC2 leads, water temp lead

Dell laptop

- Has the necessary LabVIEW files on it

Ice in a bucket

Experimental Setup:

1. Gather all needed equipment.

2. Configure the lamp and the gauge holster facing towards each other.

3. Connect water hoses to lamp.

a. This requires that two hoses are connected to the water pumps and then to one side of the lamp (provide cooling water). Another two hoses are connected to the other side of the lamp and are allowed to empty into the water bin (take cooling water away).

4. Connect water hoses to gauge.

    a. For the SB gauge, there are 4 hoses total. Two hoses should be hooked up to one pump to provide cooling water to both the gauge and the plate. The other two hoses are free to the bin to take the cooling water away from both the gauge and the plate.

    b. For the HTHFS, there are 5 hoses. One hose provides cooling water to the gauge and is thus connected to a pump while all other hoses are free to the water bin.

5. Mount gauge into plate holder. Use thermal grease to reduce contact resistance. Screw gauge into holder.

6. Mount gauge and holder into gauge holster. Use machinist ruler to ensure gauge face is 1.25" away from lamp face. Tighten bolts on holster so that it becomes fixed to lamp base (does not move/wiggle).

7. Plug in lamp and multimeter to variac (brown to red and blue to black). Make sure multimeter and variac are also plugged in.

8. Connect all lead wires to daq (See Figure 1).

    a. SB gauge lead wires are white (+) and black (-). These leads go connected to the 9219 module. Connect the leads to any desired channel but ensure that the white wire (+) is connected to terminal 4 (high signal) and the black wire (-) is connected to terminal 5 (low signal).

    b. For the HTHFS, the yellow wire (Chromel) is the positive lead and the red wire (Alumel) is the negative lead. When connecting connectors together, positive side goes to positive and negative goes to negative. These go connected to the 9213 module for temperature readings and then connected to the 9219 for heat flux readings.

    c. Make sure to connect a TC for the water temp.

9. Configure Labview file to read channels as they are hooked up and for a sampling rate of 1Hz.
10. To do this, open the labview file titled "HTHFS Radiation Calibration" or "SB Radiation Calibration" depending on which you are performing. Open the DAQ Assistant block and ensure that the physical channels correspond to the actual channel.

11. You are now ready to calibrate.

12.

Calibration Procedure:

1. Turn on daq and allow warm up of 15 min.

2. Check to make sure all hoses are connected properly.

3. Check that all lead wires are connected properly.

4. Check to make sure VI channels correspond to actual channels.

5. When the system is at thermal equilibrium with the surroundings (Before water pumps or heater are turned on) run the VI to make sure text file of raw data is being written.

6. Collect data at thermal equilibrium for at least 2 min prior to ramping up the voltage. This is the voltage offset in the system and will be subtracted off of the data (Subtracting bias).

7. Ramp up the voltage on the variac to desired setting and allow for entire system to reach steady state (no change in temperature >0.2 C for 5 min). Repeat for desired voltage levels.

    a. Note: The voltage level is entirely up to the calibrator, however 5 measurements in the range of 40-120V should be fine. We expect the response to be approximately linear to the input voltage.

8. Record all voltage levels. These will be used later in the code.

9. Be sure to monitor the water temperature. If it rises above room temp (22-26 C), add ice to the water bin. It is important to keep the gauge close to room temperature to ensure that convection is kept to a minimum level.

Post Processing:

This can be done in Excel or Matlab.

For SB:

If you are using the SB gauge to calibrate the lamp, you will

1. Average the baseline measurements (first 2 min) and subtract this average from all of the voltage output data. This gets rid of offset voltage.

2. Go through data and identify the end time of the steady state events.

3. Average the steady state data (example: the end of the steady state event was at 500 seconds so I am going to average the last 60 measurements from 440 to 500).

4. Multiply this by 10^6 to put data into micro-Volts (uV).

5. Take this and divide by the sensitivity (625.19 uV/(W/cm^2)) to get *absorbed* heat flux (heat flux absorbed by sensor).

6. We can now calculate the *incident* heat flux to the sensor by dividing by the emissivity which is 0.94 for the black paint in the lab. (Recall our assumption of negligible convection.)

7. Plot the input voltage versus the incident heat flux. Use a 4^{th} degree polynomial fit to find the coefficients we will use to relate input voltage to incident heat flux for future calibrations.

<u>For HTHFS:</u>

If you are calibrating a HTHFS, you will

1. Average the baseline measurements (first 2 min) and subtract this average from all of the voltage output data. This gets rid of bias voltage.

2. Go through data and identify the end time of the steady state events.

3. Average the steady state data (example: the end of the steady state event was at 500 seconds so I am going to average the last 60 measurements from 440 to 500).

4. Multiply this by 10^6 to put data into micro-Volts (uV).

5. Use the coefficients from the SB calibration and evaluate the polynomial equation at the voltage levels used during the calibration. This gives the *incident* heat flux of the lamp.

6. We can now calculate the *absorbed* heat flux to the sensor by multiplying by the emissivity which is 0.94 for the black paint in the lab. (Recall our assumption of negligible convection.)

7. Divide the mean SS voltage output from the gauge by the absorbed heat flux to get sensitivities in uV/(W/cm^2).

Thermal Storage Calibration using Lamp

Introduction:

This document serves as a guideline for all HTHFS thermal storage lamp calibrations. It is best to try and follow these procedures to ensure consistent calibration methods are being used.

Equipment:

Halogen Lamp:

- USHIO J120V-250W/79 halogen bulbs
- Life of 2000 hours
- Lamp has focal point of 1.25" away from its face

Model SC-10T Variac:

- 0-130 VAC
- Max 1000W
- 117VAC, 60 Hz input

HP 3468A True RMS Multimeter:

- We want to measure AC

HTHFS with alumina surrounding:

- The gauge is mounted in a piece of alumina to provide for insulation.

Gauge Holster:

- Same as for differential calibration

NI cDAQ 9172:

- 24 bit Sigma delta A/D
- 9213 thermocouple module
- 9219 voltage module
- HTHFS TC1 and TC2 leads, reflector temp lead

Pneumatic Cylinder:

- Clippard SDD-17-9
- Max 250 psi
- 1 1/16" bore
- 9" stroke

2 Solenoid Valves

- MAC 224B-531BAA
- 0.5 C_v
- Vacuum to 150psi
- 3 port, 2 directions—(Port 1 inlet, port 2 outlet, port 3 exhaust)
- 24 VDC (either on or off)

2 DC Power supplies (For valves)

- 24 VDC

Dell laptop

- Has the necessary LabVIEW files on it---Slug_calibration VI

Experimental Setup:

13. Gather all needed equipment.

14. Configure the lamp and the gauge holster facing towards each other.

15. Connect water hoses to lamp.

    a. This requires that two hoses are connected to the water pumps and then to one side of the lamp (inlets to provide cooling water). Another two hoses are connected to the other side of the lamp and are allowed to empty into the water bin (outlets to remove cooling water).

16. Mount gauge into insulation slot. Use #1 bolts ~1 ¼" long with small metal plate on back.

17. Mount gauge and insulation into gauge holster. Use machinist ruler to ensure gauge face is 1.25" away from lamp face. Tighten bolts on holster so that it becomes fixed to lamp base (does not move/wiggle).

18. Mount pneumatic cylinder (with brackets) onto base plate with screws 10-32-1/2". Also mount solenoid valves onto base plate with 10-32-2" screws. Clamp base plate to table; ensure sheet metal is covering the lamp and gauge.

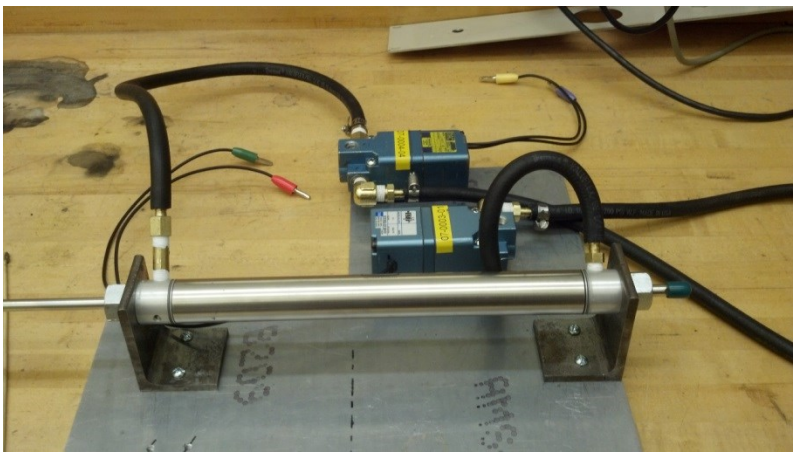

Figure B.1: Pneumatic Cylinder with valves

19. Connect all lead wires to daq.

a. For the HTHFS, the yellow wire (Chromel) is the positive lead and the red wire (Alumel) is the negative lead. When connecting connectors together, positive side goes to positive and negative goes to negative. These go connected to the 9213 module for temperature readings and then connected to the 9219 for heat flux readings.

b. Make sure to connect a TC for the water temp.

20. Hook hose up to airline. Plug valve leads into DC supplies.

21. Plug in lamp and multimeter to variac (brown to red and blue to black). Make sure multimeter and variac are also plugged in.

22. Configure Labview file to read channels as they are hooked up and for a sampling rate of 2 Hz.

    a. To do this, open the labview file titled "HTHFS Slug Calibration". Open the DAQ Assistant block and ensure that the physical channels correspond to the actual channel.

23. You are now ready to calibrate.

Calibration Procedure:

10. Turn on daq and allow it to warm up for 15 min.

11. Check to make sure all hoses are connected properly.

12. Check that all lead wires are connected properly.

13. Check to make sure VI channels correspond to physical channels.

14. When the system is at thermal equilibrium with the surroundings (Before water pumps or heater are turned on) run the VI to make sure a text file of raw data is being written.

15. Collect SS data at thermal equilibrium for at least 2 min prior to ramping up the voltage. This is the voltage offset of the system and will be subtracted off of the raw data.

16. Actuate the rear solenoid by supplying power to it so that piston rod is fully extended, thus covering the gauge from the lamp. Remove power from the valve.

17. Ramp up the voltage on the variac to desired setting and allow it to reach SS (1-2 seconds). When ready, apply power to the front valve to actuate the piston backwards,

uncovering the gauge. Allow gauge to be exposed for 30 seconds before covering up again and shutting variac off. Allow gauge to reach equilibrium before next test. Repeat for desired voltage levels.

a. Note: The voltage level is entirely up to the calibrator, however 5 measurements in the range of 40-120V should be fine. I used [40V, 60V, 80V, 100V, 120V].

18. Record all voltage levels. These will be used later in the code.

Post Processing:

8. Average the baseline measurements (~first 2 min) and subtract this average from all of the voltage output data. This gets rid of offset voltage.

9. Multiply this by 10^6 to put data into micro-Volts (uV).

10. Enter all voltage levels used during testing as well as sensor differential sensitivities and sample rate used in Hz.

11. Use the lamp coefficients from the SB calibration and evaluate the polynomial equation at the voltage levels used during the calibration. This gives the *incident* heat flux.

12. We can now calculate the *absorbed* heat flux to the sensor surface by multiplying by the emissivity which is 0.94 for the black paint in the lab. (Recall our assumption of negligible convection.)

13. Go through data and identify the start and end time (or duration) of each event.

14. Pick out heat flux data and temperature data which only correspond to the individual thermal events.

15. Subtract the initial temperature for each event from both TC measurements.

16. Average the two sensor thermocouple measurements to get Tavg.

17. Divide the average temperature by the non-cooled heat flux and plot for all voltage levels to get the inverse of the gauge thermal storage.

a. Use methodology found in slug cal write-up.

18. Fit the plotted line using a linear fit. The inverse of the slope of this line is the thermal storage of the gauge.

Slug Calibration Calculations

Method 2:

- Accounts for energy losses due to re-radiation from gauge surface and heat lost to insulation

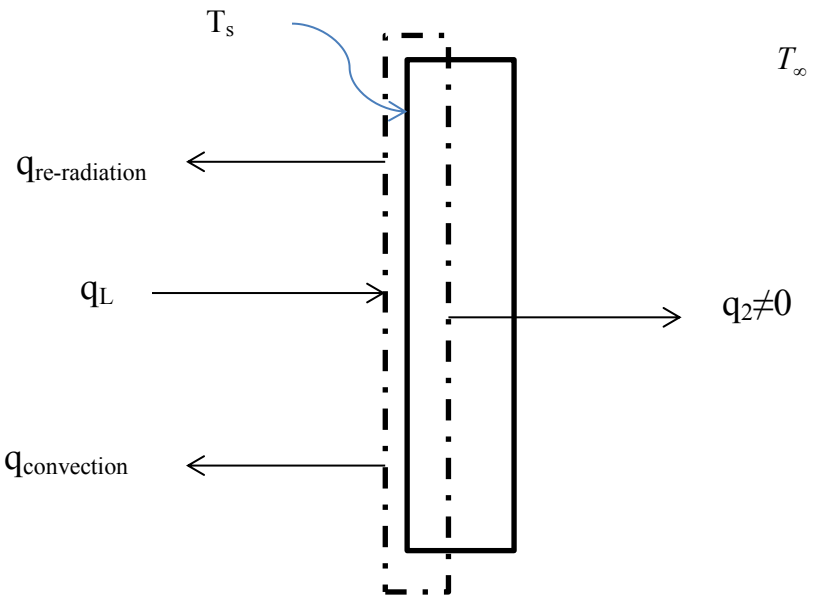

q_L=heat absorbed by surface from lamp

$q_{re\text{-}radiation}$=re-radiation heat flux from gauge= $\varepsilon_s \sigma T_s^4$

$q_{convection}$=convection heat transfer= $h(T_s - T_\infty)$

q_2=heat lost to insulation (calculated using HHF method)

In HHF method:

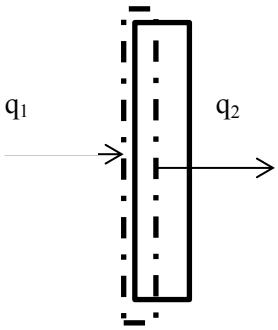

$$q_{diff} = \frac{q_1 + q_2}{2} = \text{Output from HTHFS}$$

$$q_{slug} = \rho c_p \delta \frac{dT}{dt} = q_1 - q_2$$

Rearranging and adding to solve for q_2:

$$q_1 + q_2 = 2q_{diff}$$

$$-q_1 + q_2 = -\rho c_p \delta \frac{dT}{dt}$$

$$q_2 = q_{diff} - \frac{1}{2}\rho c_p \delta \frac{dT}{dt}$$

Plugging all components into an energy balance on the surface:

$$\rho c_p \delta \frac{dT}{dt} = q_L - q_{re-radiation} - q_{convection} - q_{diff} + \frac{1}{2}\rho c_p \delta \frac{dT}{dt}$$

$$\frac{1}{2}\rho c_p \delta \frac{dT}{dt} = q_L - q_{re-radiation} - q_{convection} - q_{diff}$$

Rearranging

$$\frac{d}{dt}\left(\frac{T - T_i}{2\left(q_L - q_{re-radiation} - q_{convection} - q_{diff}\right)}\right) = \frac{1}{\rho c_p \delta}$$

$$\frac{d}{dt}\left(\frac{T - T_i}{2q_{net}}\right) = \frac{1}{\rho c_p \delta}$$

For this calibration, in order to include convection, an estimate of h as well as an estimate of the ambient air is required.

Air-cooled Gauge Calibrations

Vin =

40.9690 60.7203 83.2323 99.8380 121.8650

S1 =

223.8943 234.9282 236.8459 233.8420 229.0795

S2 =

129.8114 134.7993 134.6924 133.2598 129.1815

S1a= 231.7180
S2a= 132.3489

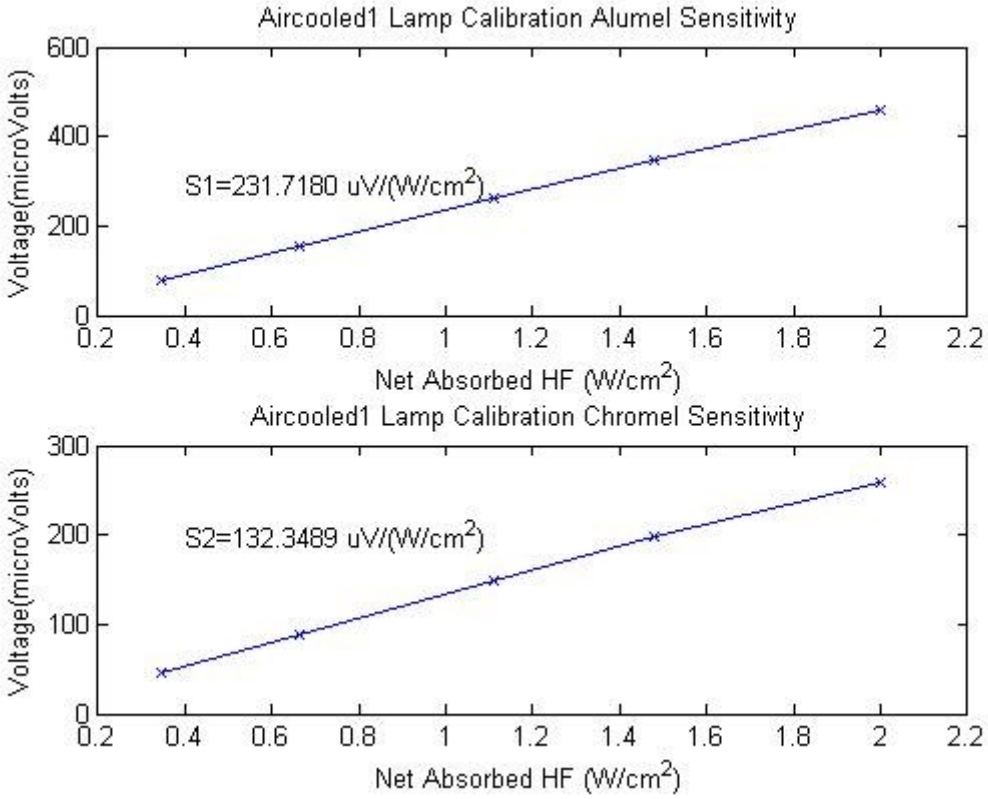

Figure B.2: Air-cooled Gauge Voltage vs. Absorbed Heat Flux

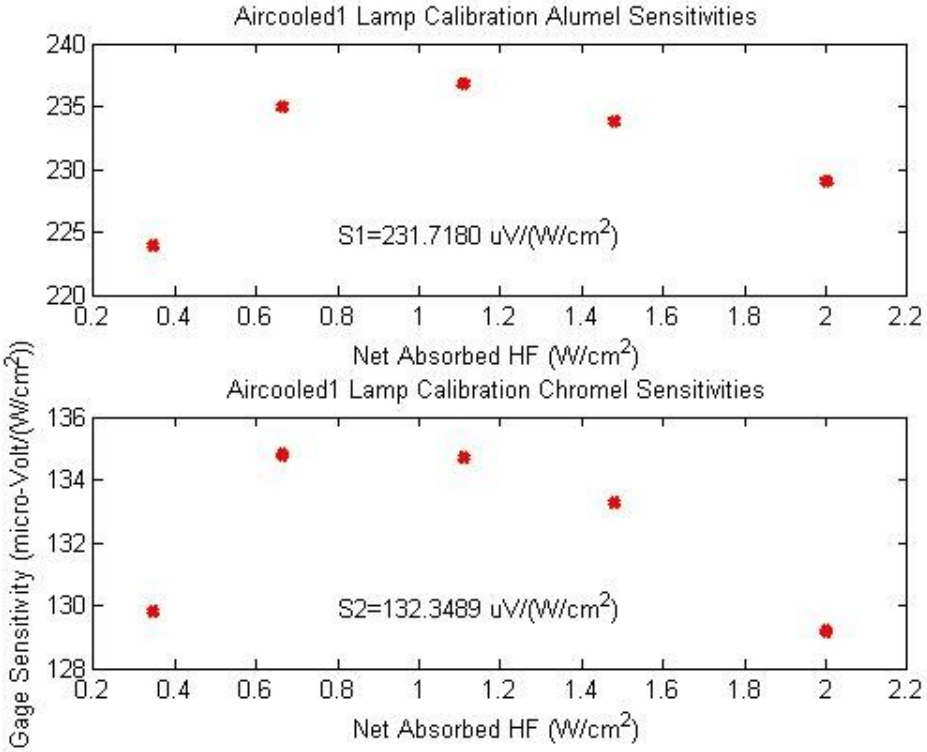

Figure B.3: Air-cooled Gauge Differential Sensitivities

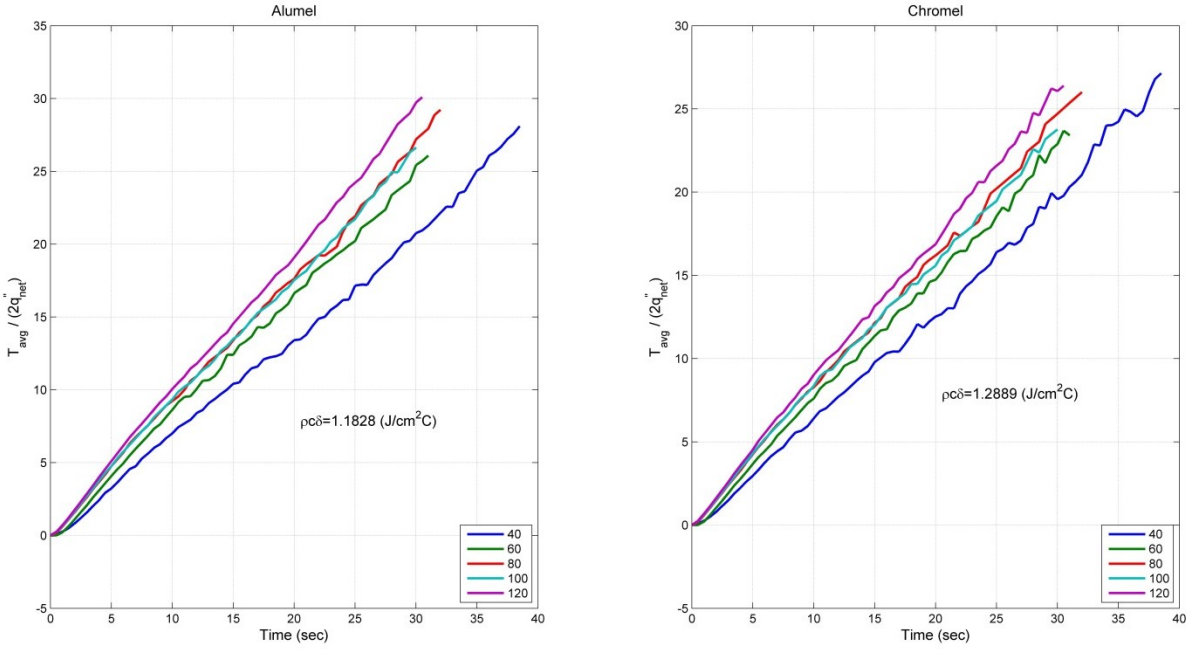

Figure B.4: Air-cooled Gauge Slug Sensitivities

Non-cooled Hybrid Gauge Calibrations

Vin =
  40.1980 60.2267 80.7960 100.3110 120.7593

S1 =
  494.4100 500.3134 505.9333 508.1097 521.8743

S2 =
  364.8202 371.1437 376.2748 377.1528 387.0087

S1a = 506.1281
S2a = 375.2800

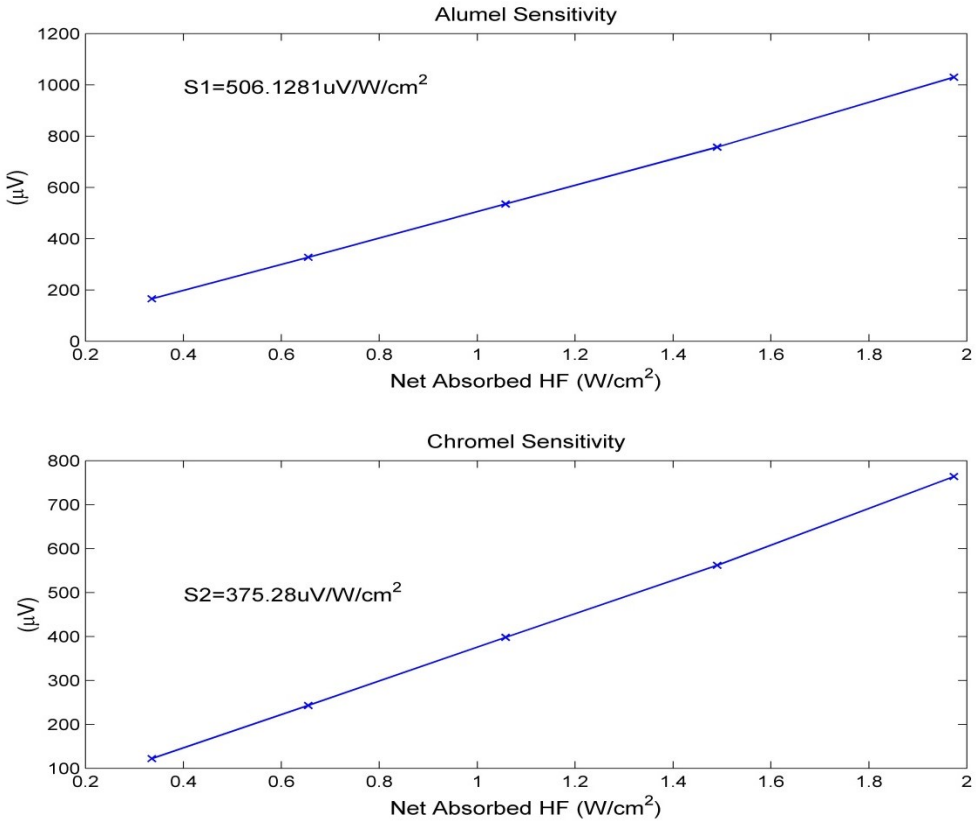

Figure B.5: Non-cooled Gauge Voltage vs. Absorbed Heat Flux

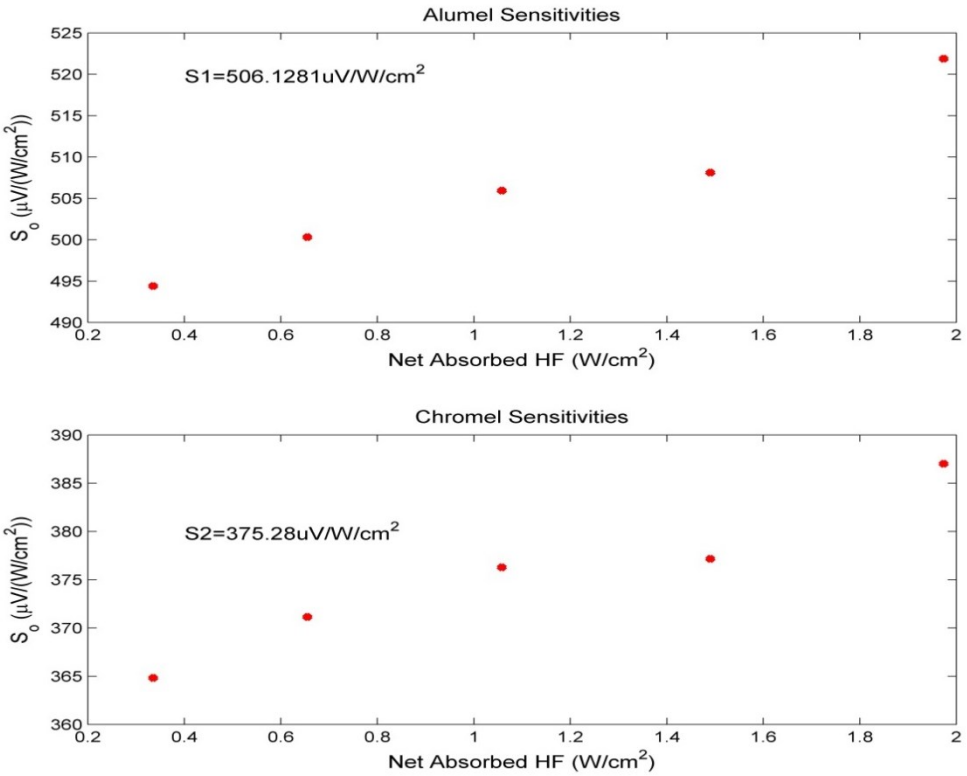

Figure B.6: Non-cooled Gauge Differential Sensitivities

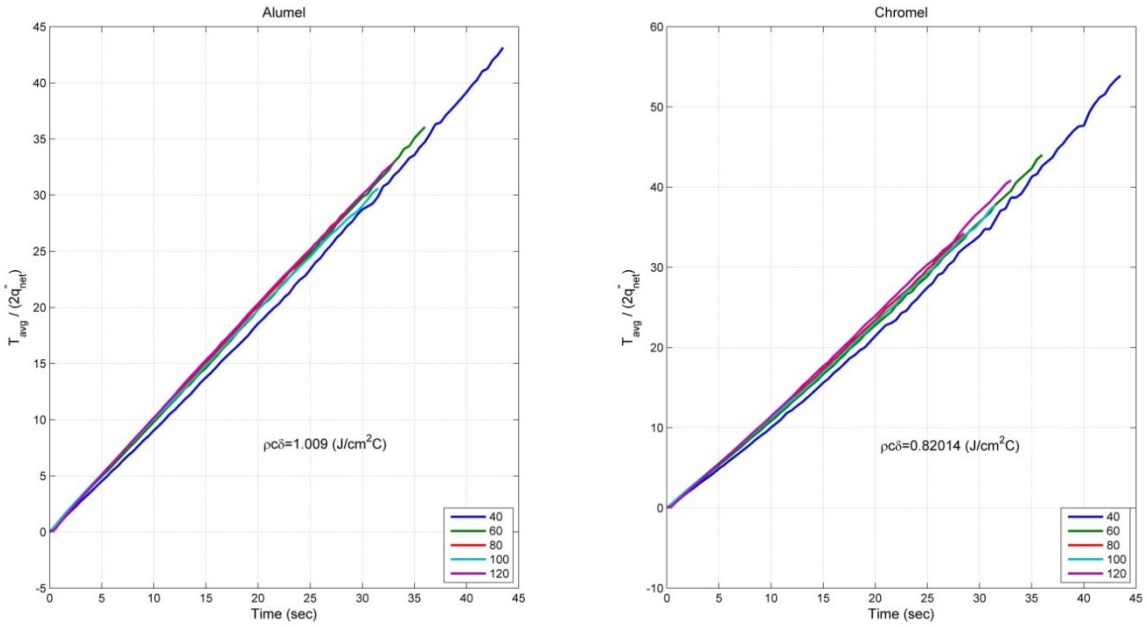

Figure B.7: Non-cooled Gauge Slug Sensitivities

APPENDIX C- SOOT CALIBRATIONS

Due to the incomplete combustion of the diffusion flame, soot formed onto the gauge surfaces during the tests. To minimize the change in emissivity during the tests, the gauges were covered in soot prior to running a test. The gauges were calibrated for the emissivity using the calibration sensitivities calculated in Appendix B. The results of the calibrations are shown in this appendix.

Table C.1: Gauge Emissivities

Air-Cooled Emissivities							
e1	**40**	**60**	**80**	**100**	**120**	**Avg**	
1	0.8218	0.8446	0.846	0.8267	0.814	0.83062	
2	0.805	0.8379	0.8431	0.8028	0.7525	0.80826	
e2	**40**	**60**	**80**	**100**	**120**	**Avg**	**Overall Avg.**
1	0.8508	0.828	0.7734	0.7382	0.6907	0.77622	0.77
2	0.7112	0.6786	0.653	0.6251	0.5931	0.6522	
Non-Cooled Emissivities							
e1	**40**	**60**	**80**	**100**	**120**	**Avg**	
1	0.9373	0.962	0.9626	0.9703	0.9809	0.96262	
3	0.7756	0.7385	0.8406	0.8501	0.8411	0.80918	
							Overall Avg.
e2	**40**	**60**	**80**	**100**	**120**		0.84
1	0.7826	0.7855	0.7772	0.78	0.7861	0.78228	
2	0.8003	0.8071	0.8133	0.8146	0.8211	0.81128	

APPENDIX D -VELOCITY AND GAS TEMPERATURE PROCEDURE

Purpose:
This outlines the materials, instrumentation, and experimental procedure for the velocity and gas temperature measurements. The goal of these experiments is to collect velocity and gas temperature data at various elevations above the burner with a ceiling present. Various ceiling heights and fire sizes were examined as outlined in Table 1 below.

Table D.1: Test Matrix for Velocity Measurements

	50 kW	**90 kW**
$L_f/2$	19.25” Burner: 23” above ground Ceiling: 42.25” above ground	25” Burner: 17.125” above ground Ceiling: 42.25” above ground
$L_f/1.5$	25” Burner: 17.125” above ground Ceiling: 42.25” above ground	33.625” Burner: 8.625” above ground Ceiling: 42.25” above ground
$L_f/1$	38” Burner: 8.625” above ground Ceiling: 46.75” above ground	50” Burner: 7.75” above ground Ceiling: 58” above ground

Instrumentation:

- Setra Model 264 ±0.25 in WC differential pressure gauge

Figure D.1: Setra Gauge

- Aspirated thermocouple probe
- Pump
- Type K thermocouple
- Bi-directional probe

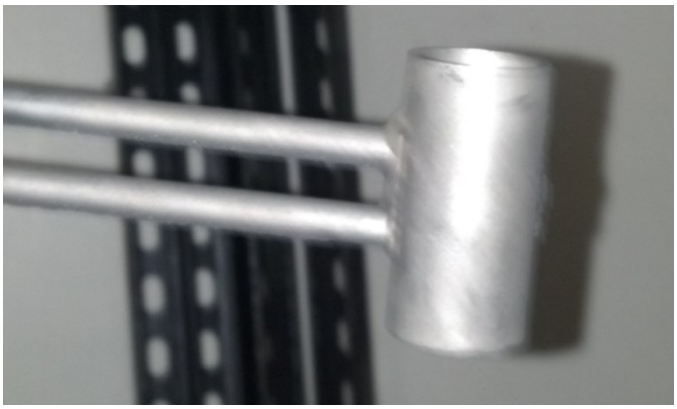

Figure D.2 Bi-directional Probe

- NI 9205 DAQ module

Materials:

- Ceiling Apparatus

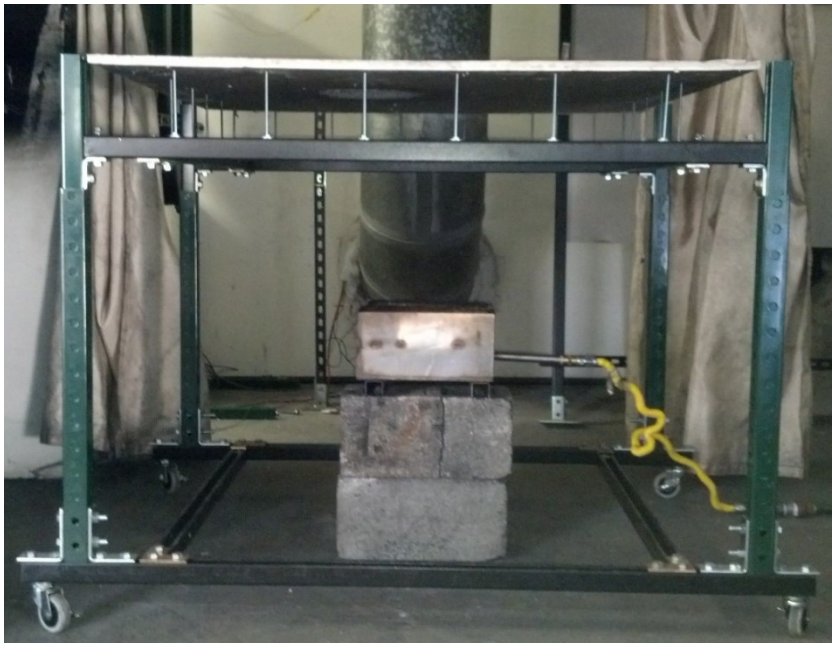

Figure D.3: Ceiling Apparatus

- 4 ft x 4 ft Type X fire rated gypsum (5/8" thick) drywall

Setup Procedure:

1. Place ceiling apparatus underneath hood. Make sure it is centered. It is easiest if the sand burner gas line is run over the base of the apparatus.
2. Adjust the ceiling apparatus to the desired height (account for burner height).
3. Place drywall ceiling on top of apparatus. Center it as much as possible.
4. Center the burner underneath the ceiling.

5. Place the wire mesh around the ceiling apparatus and the curtains around the two sides of the apparatus.
6. Insert thermocouple into aspirated probe assembly if not already present. It should be ~ 0.5" from the tip of the tube.
7. Adjust the height of the bi-directional probe and aspirated thermocouple to the desired elevation above the burner (do not go lower than 9" above the burner as probe joints will melt).
8. Center the bi-directional probe over the burner.
9. Place the aspirated thermocouple probe on the right hand side of the bi-directional probe, centered vertically on the probe (see picture below).

Figure D.4: Bi-directional and Aspirated Thermocouple Probe Placement

10. Attach Setra gauge to strut pole at approximately the same height as the bi-directional probe.
11. Connect the lines from the Setra gauge to the bi-directional probe and plug in the power supply to the Setra gauge.
12. Connect the thermocouple lead wires to the daq connector.
13. Once the lab computer is on, locate the folder on the Desktop titled "Rachel". The LabVIEW program to collect this data is titled "Pressure".
14. Go into the block diagram of the LabVIEW VI and click on the DAQ Assistant. Make sure that the physical channel selected matches the channel on which each sensor is connected. The pressure probe should be connected to the NI 9205 module and the thermocouple should be connected to the NI 9213 module. Select Type K for thermocouple.
15. Make sure the sampling rate is set to 200 Hz (so that a filter can later be applied to get rid of 60 Hz from fume hood motor controller).
16. Check to see that the ranges for the pressure sensor (0-5 V) and the thermocouple (0-1300 C) are correct.
17. If any changes to the program are made, save it.

18. Make sure to give the data file saved by LabVIEW a new name.

Experimental Procedure:

1. Run the LabVIEW program and collect 2 min of baseline data without the fume hood on.
2. Follow the startup procedure for the sand burner located in the lab (near computer).
3. Once the sand burner is ready to go, collect another 2 min of baseline data with the fume hood on.
4. You are now ready to run a test.
5. Starting at the desired height, set the burner setup to the desired fire size.
6. Allow temp and bi-directional probe to reach a steady-state.
7. Record data for 1 ½ minutes.
8. Take notes about the flame shape i.e. times in which the flame leans or is not straight, if the flame is wide, etc.
9. Shut the fire off and stop recording.
10. Repeat steps 5-9 for each height above the burner. In these experiments, elevations above the burner began at 9" and increased in increments of 3" until reaching the ceiling.

APPENDIX E -HEAT FLUX MEASUREMENTS PROCEDURE

Purpose:
This outlines the materials, instrumentation, and experimental procedure for the heat flux measurements. The goal of these experiments is to collect heat flux and gas temperature data at the ceiling with a flame impinging on it. These will aid in calculating the convection heat transfer coefficient and allow for the separation of convection and radiation. Various ceiling heights and fire sizes were examined as outlined in Table 1 below.

Table E.1: Test Matrix for Heat Flux Measurements

	50 kW	**90 kW**
$L_f/2$	19.25” Burner: 23” above ground Ceiling: 42.25” above ground	25” Burner: 17.125” above ground Ceiling: 42.25” above ground
$L_f/1.5$	25” Burner: 17.125” above ground Ceiling: 42.25” above ground	33.625” Burner: 8.625” above ground Ceiling: 42.25” above ground
$L_f/1$	38” Burner: 8.625” above ground Ceiling: 46.75” above ground	50” Burner: 7.75” above ground Ceiling: 58” above ground

Instrumentation:

- Non-cooled High Temperature Heat Flux Sensor (HTHFS)
- Air-cooled High Temperature Heat Flux Sensor (HTHFS)
- 2 Aspirated thermocouple probes
- 2 Type K thermocouples
- 2 Pumps
- Setra Model 264 ±0.25 in WC differential pressure gauge

Figure E.1: Setra Gauge

- Bi-directional probe

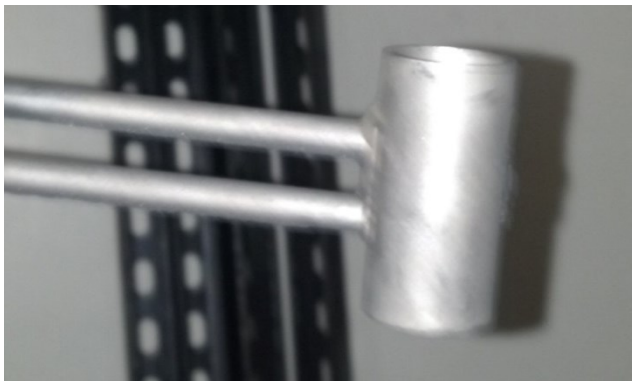

Figure E.2: Bi-directional Probe

- NI 9205 DAQ module
- NI 9213 DAQ module
- NI9219 DAQ module

Materials:

- Ceiling Apparatus

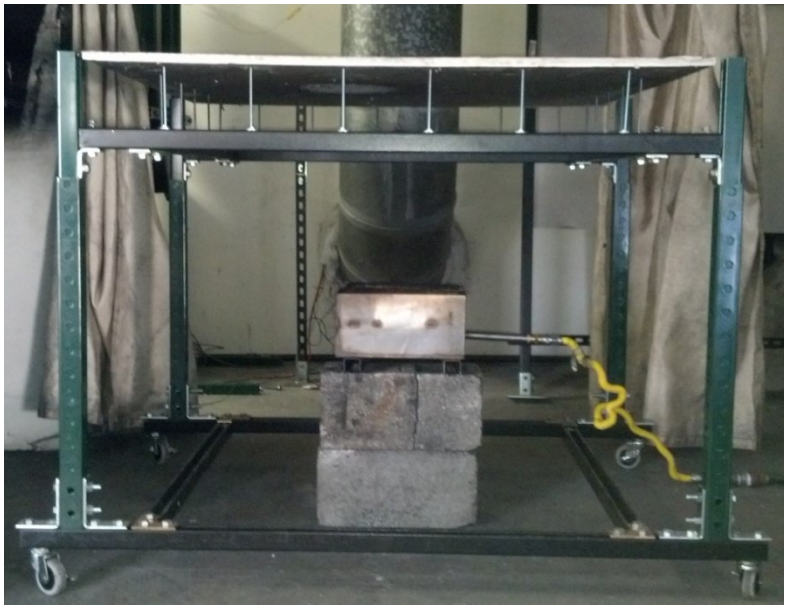

Figure E.3: Ceiling Apparatus

- 4 ft x 4 ft Type X fire rated gypsum (5/8” thick) drywall

Ceiling Preparation Procedure

1. Cut a 4 ft. x 4 ft. piece of Type X drywall
2. Measure and mark the center of the 4 ft. x 4 ft. drywall piece.
3. Cut the appropriate holes for the heat flux gauges as shown below.

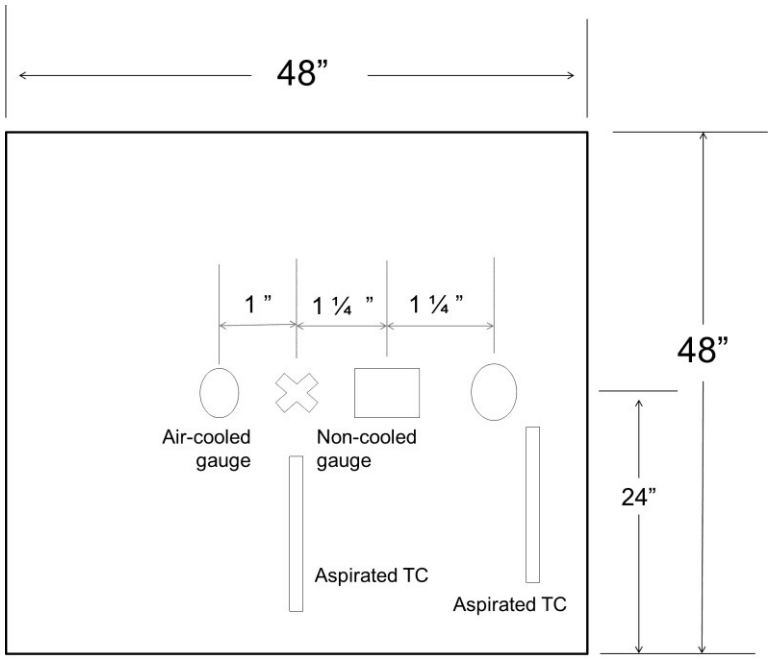

Figure E.4: Gauge Placement

The air-cooled gauge is ½” in diameter (requires a ½” hole). The non-cooled gauge is 1” long and ½” wide (requires four 1/16” holes). Place both gauges such that their edges are ¾” from the center.

4. Three 1/8” holes are also made to towards the edge of the drywall to secure the lead wires to the ceiling.
5. Attach the non-cooled gauge to the ceiling with the appropriate bolts. Make sure it is tight against the drywall.

Setup Procedure:

19. Place ceiling apparatus underneath hood. Make sure it is centered. It is easiest if the sand burner gas line is run over the base of the apparatus.
20. Situate the cart with the daq near the ceiling setup so that the heat flux gauges and aspirated thermocouple data can be measured. These are measured using the NI 9219 (heat flux) and NI 9213 (temperature) modules. The NI cdaq is the chassis.
21. Adjust the ceiling apparatus to the desired test height (account for burner height).
22. Place drywall ceiling on top of apparatus. Center the air-cooled hole as much as possible under the air-cooled gauge holder (metal bracket that runs across the ceiling apparatus).
23. Place the wire mesh around the ceiling apparatus and the curtains around the two sides of the apparatus.
24. Situate the cart with the daq near the ceiling setup so that the heat flux gauges and aspirated thermocouple data can be measured. These are measured using the NI 9219 (heat flux) and NI 9213 (temperature) modules. The NI cdaq is the chassis.

25. Attach the copper cooling tube to the air-cooled heat flux gauge inlet and to the compressed air line (back wall of lab). The blue filter on the copper line filters out any condensed air in the line.
26. Mount the air-cooled gauge through the 0.5" hole in the drywall and secure it with the 7/16" bolts. The gauge will be vertical in the air. Make sure the air-cooled gauge is protruding from the drywall at about the same distance as the non-cooled gauge, and that it is as perpendicular to the ceiling as possible.

IF SOOT IS NEEDED

27. Adjust burner height such that the ceiling is ~34" above burner.
28. Center the burner underneath the ceiling.
29. Follow soot procedure below.

IF SOOT IS NOT NEEDED (If the same piece of drywall is used from a previous test, and gauges already have soot on them, no soot procedure is needed.)

7. Adjust burner height such that the ceiling is the desired height above burner.
8. Center the burner underneath the ceiling.
9. Insert the two thermocouples into the aspirated probe assemblies if not already present. They should be ~0.5 " from the tip of the tube.
10. Adjust the height of the bi-directional probe and velocity aspirated thermocouple to the height above the burner in which the maximum velocity occurred in the previous set of experiments (see Table 2).

Table E.2: Max Velocity Heights for Each Test Condition

	50 kW	**90 kW**
$L_f/2$	12" above burner	15" above burner
$L_f/1.5$	15" above burner	18" above burner
$L_f/1$	21" above burner	27" above burner

11. Place the bi-directional probe 0.5" away from the edge of the non-cooled gauge. It is fed through the wire mesh through one of the openings. The wire mesh should be on the inside of the two legs.
12. Plug in the power supply to the Setra gauge.
13. Attach Setra gauge to strut pole at approximately the same height as the bi-directional probe.
14. Connect the lines from the Setra gauge to the bi-directional probe.
15. Place the aspirated thermocouple probe on the right hand side (looking towards the exhaust duct from the hood) of the bi-directional probe, centered vertically on the probe.

Figure E.5: Bi-directional and Aspirated Thermocouple Probe Placement

16. Hook the velocity aspirated thermocouple up to one of the pumps. Make sure pump has filter attached before hooking up the aspirated probe.
17. Adjust the height of the heat flux aspirated probe (near heat flux gauges) such that it is slightly lower than the ceiling height.
18. Place the heat flux aspirated probe in the center of the two heat flux gauges. It should be ~1" away from the ceiling. See pictures below for examples.

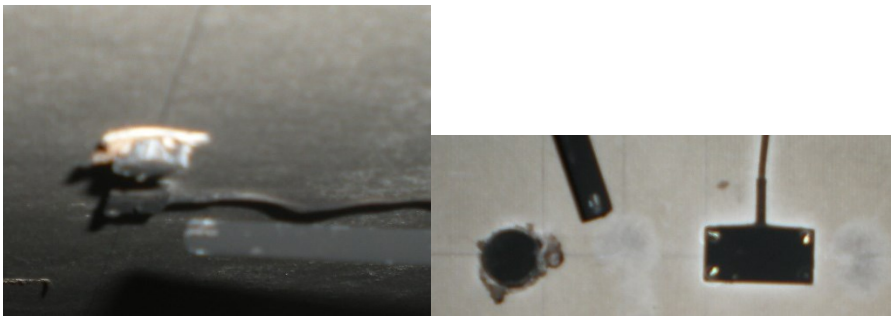

Figure E.6: Aspirated Thermocouple Placement

19. Hook the heat flux aspirated probe to the other pump. Make sure pump has filter in it before hooking up the aspirated probe.
20. Set up the video camera to record the test.
21. Connect the thermocouple lead wires and the heat flux lead wires to the daq connectors. For proper daq connector setup see the example figure below.

Soot Procedure:

1. Set the burner at a height such that the ceiling is ~34" above the burner.
2. Follow the startup procedure for the sand burner (procedure is located in the lab near computer).

3. Run a 50 kW fire for ~ 15 min or until a layer of soot is evenly distributed on both heat flux gauges. You want to make sure that no parts of the gauges are visible and both have about the same amount of soot (see pic below for example).

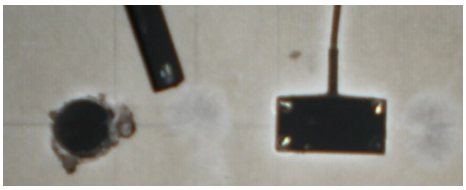

Figure E.7: Gauges with Soot

4. Allow gauges to cool back to ambient.
5. Reposition sand burner such that the ceiling height is the desired height above the burner and it is centered under the center of the drywall.

Daq Setup:

22. Once the fire lab computer is on, locate the folder on the Desktop titled "Rachel". The LabVIEW program to collect this data is titled "Pressure".
23. Go into the block diagram of the LabVIEW VI and click on the DAQ Assistant. Make sure that the physical channel selected matches the channel on which each sensor is connected. The pressure probe should be connected to the NI 9205.
24. Make sure the sampling rate is set to 200 Hz (so that a filter can later be applied to get rid of 60 Hz from fume hood motor controller).
25. Check to see that the ranges for the pressure sensor (0-5V) are correct.
26. If any changes to the program are made, save it.
27. Make sure to give the data file saved by LabVIEW a new name.
28. Turn on the laptop used to collect the heat flux data.
29. Power on the chassis and let it warm up for 15 min.
30. Locate the Desktop folder titled, 'Wasson" and open the LabVIEW program titled "Fire".
31. Go into the block diagram of the program and open DAQ Assistant. Make sure that the physical channels selected match the channels on which each sensor is connected. The heat flux gauges should be connected to the NI 9219 module and the thermocouples to the NI 9213 module.
32. Set the ADC timing mode to "Best 60 Hz Rejection" for the 9219 module and to "Let DAQmx decide" for the 9213.
33. Set both heat flux and thermocouple modules to sample at 9 Hz.
34. Make sure that the thermocouple range is set to 0-1.3k C.
35. If any changes to the program are made, save it.
36. Make sure to give the data file saved by LabVIEW a new name.
37. Run both the pressure program and the heat flux program to ensure the sensors are working correctly. If not, stop the programs and investigate the lead wires to all sensors. Also check sensors.

Experimental Procedure (performed once soot procedure and setup is complete):

11. Follow the startup procedure for the sand burner (procedure is located in the lab near computer).
12. Prior to starting a fire, start the aspirated pumps and the compressed air cooling to the air-cooled gauge.
13. Once the sand burner is ready to go, and all sensors are stabilized near ambient temperature, record 2 min of baseline data (try to push the record buttons on the pressure and heat flux programs as close in time as possible; leave the recording on).
14. Turn on the camera and start recording video.
15. Open the propane valves and set the fire size to 10 kW and light the burner. Close the wire mesh around the setup.
16. Set the fire size to the appropriate fire size as quickly as possible. For the 50 kW fire I usually ramp up to 30 kW and then 50 kW. For the 90 kW fire, I ramp to 50 KW and then 90 kW.
17. Allow fire to continue until a visual steady state is reached by all temperature probes (aspirated and heat flux gauge).
18. Take notes about the flame shape i.e. times in which the flame leans or is not straight, if the flame is wide, etc. while running the test.
19. Once a steady-state is reached by both the heat flux gauge temperatures and the aspirated probe temperatures, shut the fire off and stop recording.
20. Allow gauges to cool down to ambient.
21. Repeat steps 2-9 for each fire size and ceiling height above the burner.

APPENDIX F – COMPARISON OF METHODS FOR CALCULATING H USING PREVIOUS EXPERIMENTS

The four methods of calculating *h* were compared to previous data collected in the cone calorimeter by Vega et al. The *h* calculated using the original reference method was chosen for comparison with the new methods. The original reference method consisted of using the initial five seconds of data from the non-cooled hybrid gauge exposure as the reference heat flux and temperature. Data was taken from the experiments in Ref. [Vega paper 1].

Comparisons were made for data taken with the hybrid gauge mounted onto a piece of ceramic board at standard state heat flux levels of 20 and 40 kW/m^2. In these experiments, gas temperatures were measured separately from the experiments with the hybrid gauge. Therefore, the slope method 2 could not be evaluated appropriately. Standard state heat fluxes were measured with a Schmidt-Boelter gauge. These were also made in separate experiments, and are therefore not a direct comparison, but are sufficient for the purpose of evaluating the methods of calculating *h*. No Schmidt-Boelter temperature data was recorded, and therefore the temperature of the water used to cool it was used as the standard temperature. This measurement was taken at the outlet of the gauge holder.

Figure F.1 below shows the comparison between the *h* obtained using the reference method in Ref. [Vega 1] versus using the reference method 1 used in this research for the Ceramic 40 kW/m^2 experiment. The average values taken for both methods resulted in *h* values of 0.0125 and 0.0106 kW/m^2-K for the original reference method and reference method 1, respectively. For the 20 kW/m^2 case, the original reference method had an average *h* of 0.0134 kW/m^2-K, while the reference method 1 had an average *h* of 0.0120 kW/m^2-K.

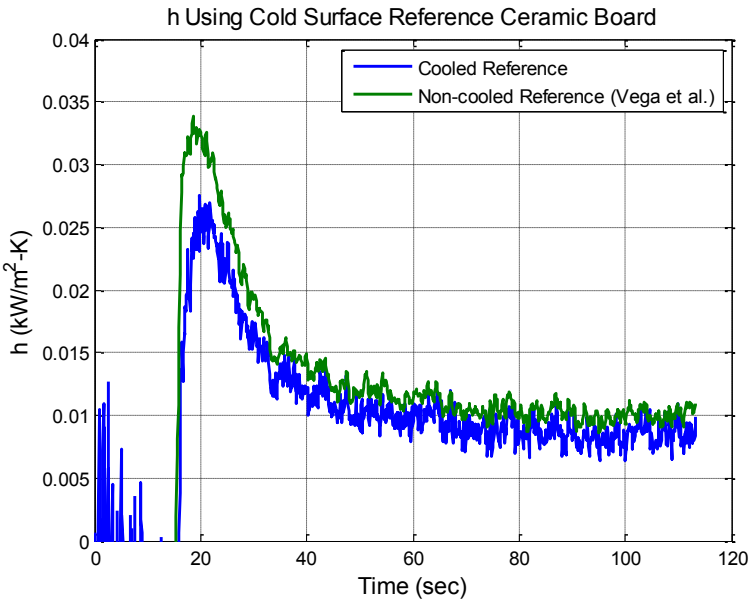

Figure F.1: Original Reference Method vs. Reference Method 1- 40 kW/m^2-K case

The results from the reference method 2 used in this research are shown below. The threshold temperature difference used to average the *h* values for each reference point was 335K. This corresponded to the temperature difference where the average was taken for the original reference method. This method resulted in an *h* value of 0.0081 kW/m^2-K for the 40 kW/m^2-K case. The *h* obtained for the 20 kW/m^2-K case was 0.0115 kW/m^2-K.

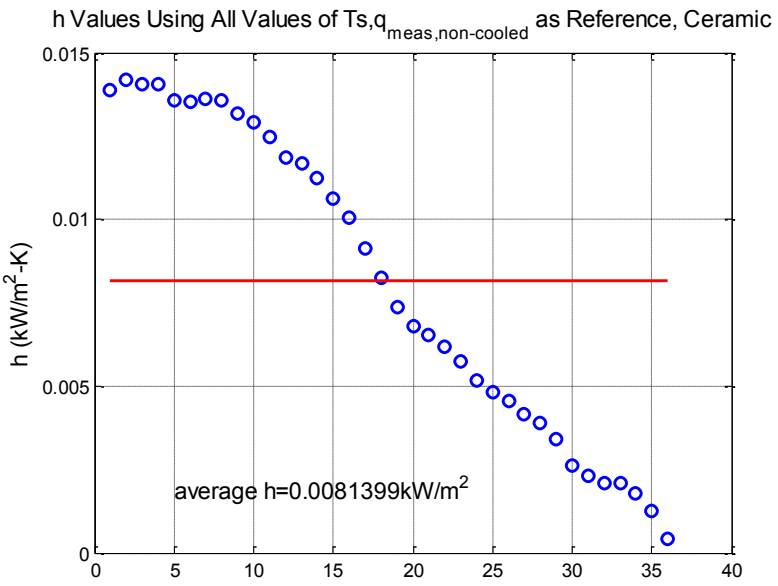

Figure F.2: Reference Method 2- 40 kW/m^2-K case

The slope methods were evaluated using the measured heat flux and surface temperatures. The gas temperature was not measured in the same experiment, therefore it was difficult to ascertain which portion of the data to include in the analysis. The slope method 1 results are shown in Figure F.3 below. Results from the slope method 2 were identical. This *h* was the lowest of the four methods with a value of 0.0074 kW/m^2-K. The curl upwards towards the right hand side of the figure represents a behavior found in the exposure heat flux. The *h* obtained using the slope methods for the 20 kW/m^2-K case was 0.0081 kW/m^2-K.

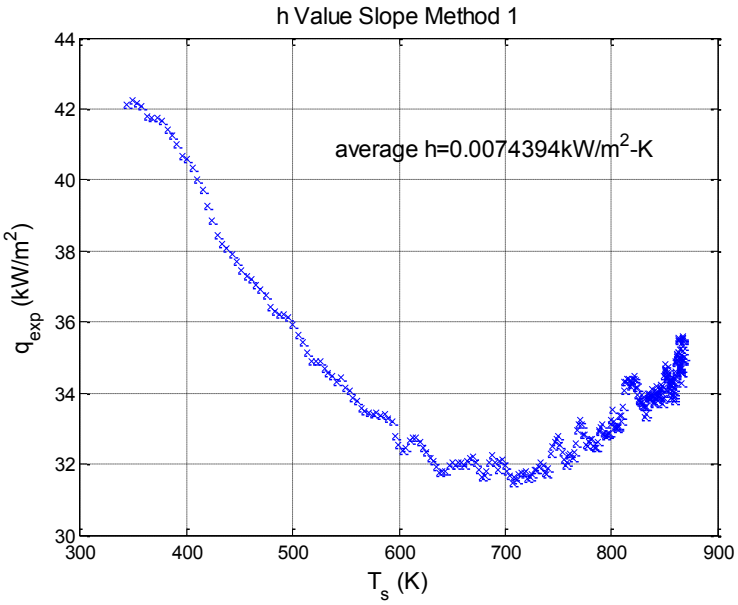

Figure F.3: Slope Method 1-40kW/m^2 case

Comparisons were also made using data from Ref. [Vega paper 2]. In these experiments, a standard state heat flux was not measured, however the reference 2 and slope methods used in this research are compared to the original reference method from the previous experiments []. Comparisons were performed for experiments in which the hybrid gauge was mounted onto marinate and ceramic boards at standard state heat flux levels of 35 kW/m^2. The plots of each are not shown as above, however all results are listed in Table F.1.

Table F.1: Summary of Comparisons for *h* Methods

	Ceramic		Marinite	Ceramic
Heat Flux (kW/m2)	**40**	**20**	**35**	**35**
Original	0.0125	0.0134	0.024	0.0138
Ref 1	0.0106	0.012	--	--
Ref 2	0.0081	0.0115	0.0263	0.0093
Slope 1	0.0074	0.0081	0.0173	0.0075
Slope 2			0.0176	0.0076

Based on these comparisons, the reference method 1 produces slightly lower results than the original reference method.

APPENDIX G- FFT OF PRESSURE DATA

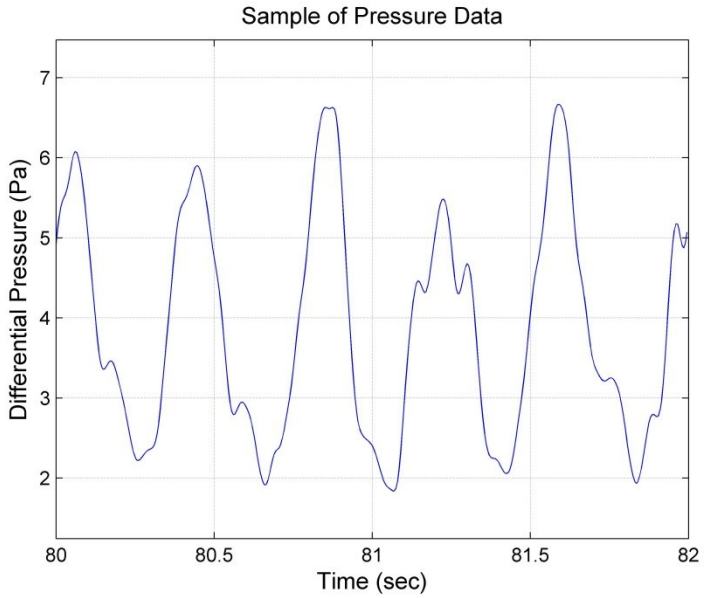

Figure G.1: Sample of Pressure Data

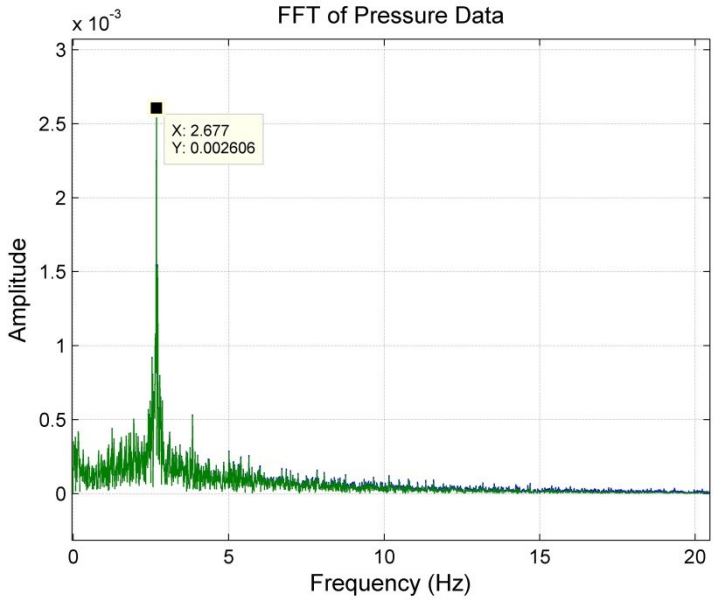

Figure G.2: Sample of FFT of Pressure Data

Figure G.1 shows a sample of the pressure data taken from Chapter 2 of this thesis. It is a sinusoidal type signal as expected. Figure G.2 shows the FFT of the time signal shown in Figure F.2. It can be seen that the dominant frequency occurs around 2.7 Hz. This was consistent throughout all measurements at each of the experimental configurations, particularly as z increased. Some dominant frequencies occurred at values slightly closer to 3 Hz, with values of 2.8-2.9 Hz. This behavior agrees with that found in the literature [McCaffrey].

APPENDIX H- EXPOSURE HEAT FLUXES

The exposure heat fluxes for each gauge are determined from Equation (12) using their respective measured heat fluxes. Figure H.1 shows a comparison of the exposure heat fluxes for the air-cooled and the non-cooled gauge and the difference between the measured gas and gauge surface temperatures for the 50 kW experiments. The results from the 90 kW *HRR* were similar. These plots may help to explain the behavior of the two gauges used to calculate the reference method 1 *h* value. Taking a look at the top two plots, shows that although the difference between the measured gas temperature and air-cooled gauge temperature is larger than the non-cooled gauge, its exposure flux is almost the same. According to Equation (10) and the assumptions that the absorbed irradiation and gas temperatures are constant, the air-cooled exposure flux should be larger than the non-cooled exposure flux, particularly for later test times as the temperature difference between the non-cooled gauge decreases. On the contrary, the exposure heat fluxes are roughly the same. This could be an indication of two things: that the *h* is indeed close to zero at small ceiling heights or that that their *h* values are not the same. If convection is really small, then the exposure flux would mostly be a measure of the absorbed irradiation heat flux component. If the *h* is not near zero, then this is an indication that the two gauges do not have the same irradiation between the two or the same *h*. Notice that as ceiling height increases, the exposure fluxes behave as expected. Perhaps at the lower ceiling heights, the local boundary conditions around each gauge are different.

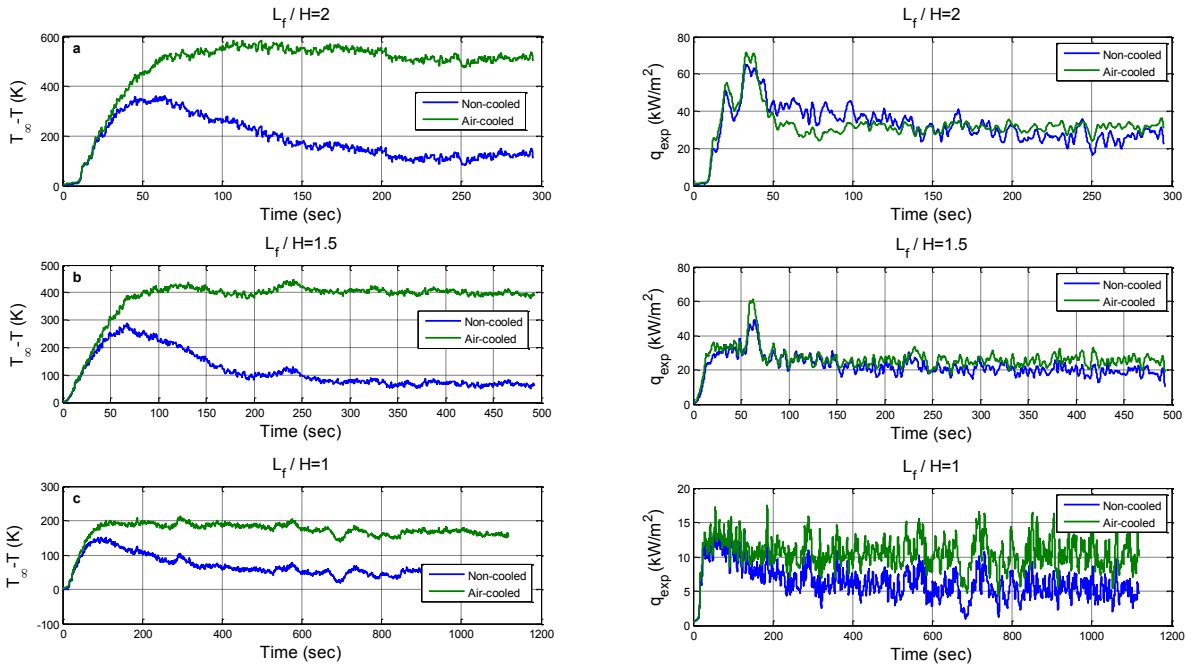

Figure H.1: T_∞-T and q_{exp} for 50 kW HRR: a) L_f/H=2, b) L_f/H=1.5, c)L_f/H=1